



Development of Bioelectronics for Inertial Sensing
Applications

Thesis submitted to the Faculty of Science, Agriculture
and Engineering as a part of the requirement for the
degree of Doctor of Philosophy

Submitted by: Carl Dale

School of Mechanical and Systems Engineering

Date: 28th October 2011

Development of Bioelectronics for Inertial Sensing Applications

C. Dale¹, N. Keegan, C. J. McNeil, J. Hedley
School of Mechanical and Systems Engineering
University of Newcastle upon Tyne, NE1 7RU

ABSTRACT: Inertial navigation systems (INS) are employed for the accurate navigation of military and civil vehicles. Modern non-conventional INS technologies incorporate the use of microelectromechanical systems (MEMS) such as microgyrometers and microaccelerometers to act as the sensing component. The development of bioelectronics has been integrated with microaccelerometer technology to develop a novel sensitive sensing system. The bioelectronic element consisting of a metallised DNA nanowire anchored between a sensing gap to allow the measurement of acceleration. The approach of bottom up fabrication (i.e. building up from constituent parts) has been undertaken for the development of bioelectronics allowing the assembly of novel MEMS microaccelerometers. The use of surface gold thiol (-SH) chemistry has been performed to allow highly specific deposition of deoxyribonucleic acid (DNA) molecules on sensing surfaces. The placement of λ -DNA immobilisation and hybridisation has been analysed in real time by utilising techniques such as surface plasmon resonance (SPR) allowing the suitability of the protocols to be scrutinised for DNA nanowire formation.

The design and fabrication of MEMS microaccelerometers was undertaken with exact specifications to allow the immobilisation and subsequent DNA nanowire assembly for the bioelectronic sensing component to be realised. The microaccelerometers were characterised by scanning electron microscopy (SEM) and optical profilometry to determine the suitability for the application. The use of self assembled monolayers (SAMs) was exploited to immobilise DNA specifically on gold sensing electrodes. Sequence specific complementary DNA hybridisation was employed giving the ability to further position the nanowires between gold sensing electrodes. The positioning being achieved using dielectrophoretic (DEP) methods to stretch and align immobilised DNA in the required direction and orientation. Further the DNA was subjected to metallisation to give electrical functionality that allows it to be used as the sensing element. The intercalation of metals such as zinc onto DNA templates was performed and monitored using spectrophotometric methods to allow a future assessment of the electrical properties. The research aim being to develop robust hybridisation protocols for the controlled selective placement and subsequent metallisation of DNA to allow the integration of bioelectronics into novel nanoscale microaccelerometer systems.

KEYWORDS - DNA Nanowire, DNA Immobilisation, Self Assembled Monolayers, SAMs, Molecular Electronics, Bio-MEMS, DNA Metallisation, MEMS, Microaccelerometer.

¹ Author to whom correspondence should be addressed. E-mail: carl.dale@ncl.ac.uk

In the loving memory of
John Anthony Highfield
'Tony'

1948-2008

Acknowledgments

It would not have been possible to write this doctoral thesis without the help and support of the kind people around me, to only some of whom it is possible to give particular mention here.

Above all, I would like to thank my girlfriend Niamh for her personal support and great patience at all times. My mum Daphne, my brother Kevin and most importantly Tony who have all given me their unequivocal support throughout, for which my mere expression of thanks does not suffice. Also, I express my gratitude to the Lightfoot family for their kind support and ensuring I have been behaving throughout my time in Newcastle.

This research would not have been possible without the help, support and patience of my supervisors Dr. John Hedley, Dr. Neil Keegan and Prof. Calum McNeil and for their advice and unsurpassed knowledge throughout. I thank John for enrolling me as his PhD student to which I am truly grateful. I admire his endurance and calmness when attempting to teach me engineering principles. I am grateful to Neil for his patience, sagacity and sound advice throughout my PhD journey to completion; it would not have been possible without his help. I express my gratitude to Calum for his strong support and for allowing me the honour to work alongside him at DTT. Also, I must give thanks for the support and friendship of all that were involved along the journey such as Julia Spoor, Robin Page, Sunil Rana, and James Henderson, who have all been invaluable on both an academic and a personal level.

I am grateful to Sanggar Dewanto for helping me to understand ANSYS finite element modelling and put it into practice, before his help I was sunk, after his help I took to it like a Cat to water!

Amongst my fellow postgraduate students in the school of Mechanical and Systems Engineering and the Institute of Cellular Medicine, I would like to say thank you for promoting a stimulating and welcoming academic and social environment.

For any errors or inadequacies that may remain in this work, of course, the responsibility is entirely my own.

Table of Contents

Chapter 1 General Introduction

1.1. Inertial Navigation Systems and Accelerometers	1
1.1.1 Inertial navigation systems	1
1.1.2 Accelerometers	2
1.1.3 Acceleration Principles	2
1.1.4 Quality Factor	3
1.1.5 Accelerometer resonant frequency concepts	4
1.1.6 Spring constant and Hooke's Law	5
1.1.7 Mechanical Gauge Factor	6
1.1.8 Calculation of noise acceleration from Newton's 2 nd Law	6
1.1.9 Fundamentals of accelerometer design	7
1.1.10 MEMS Microaccelerometers	8
1.1.11 Piezoresistive Microaccelerometers	8
1.1.12 Piezoelectric Microaccelerometer	9
1.1.13 Capacitive Microaccelerometers	10
1.1.14 Tunneling Microaccelerometers	10
1.1.15 The performance of Microaccelerometers	13
1.2 The discovery and properties of the DNA molecule	14
1.2.1 The short history and discovery of DNA properties	14
1.2.2 The Structure of the DNA double helix	15
1.2.3 Complementary DNA Hybridisation	17
1.2.4 Enterobacteriophage Lambda DNA	17
1.2.5 The DNA molecule as a generic material	18
1.3 Chemical Self Assembled Monolayers	19
1.3.1 Organosulphur Alkanethiol SAM Layers on Gold	19
1.3.2 DNA Self-Assembled Monolayers on gold	20

1.4	DNA Nanowire Fabrication, modification and Characterisation.....	21
1.4.1	Stretching and alignment of DNA on a micromachined surface	22
1.4.2	Hydrodynamic Stretching of DNA	22
1.4.3	DNA Molecular Combing.....	23
1.4.4	Direct Current electrophoretic stretching.....	23
1.4.5	Dielectrophoretic Stretching of DNA	24
1.5	Electrical functionality and characterisation of DNA templates.....	25
1.5.1	Modification, Metallisation and Electrical Conduction of DNA.....	26
1.5.2	DNA Templated Polypyrrole DNA Nanowires	26
1.5.3	DNA Templated Silver Nanowires	27
1.5.4	Metallisation through imino substitution reactions.....	28
<u>Chapter 2 The design, modelling and fabrication assessment of a MEMS Accelerometer</u>		
2.1	Introduction	30
2.2	The principle of the novel biological accelerometer design	30
2.2.1	The possible advantage over current accelerometer designs	30
2.2.2	Aims and requirements	32
2.3	General Outline of Accelerometer design.....	33
2.4	Structural specifications of accelerometer devices	35
2.4.1	Variation in accelerometer type design.....	35
2.4.2	The structural features specific to Accelerometer type.....	37
2.5	ANSYS Finite element analysis.....	40
2.5.1	Accelerometer FEA modal analysis.....	40
2.6	ANSYS Static deflection analysis.....	44
2.6.1	Modelled Results	45
2.7	Microfabrication Processing Technology	46
2.7.1	Lithography.....	46
2.7.2	Metal Etching.....	46

2.7.3	Metal deposition techniques	48
2.8	Microfabrication Process flow for Accelerometer Device Types	49
2.8.1	Accelerometer microfabrication process flow	50
2.9	Fabrication and Characterisation Equipment	54
2.9.1	Optical microscopy imaging	54
2.9.2	Scanning Electron Microscopy	55
2.10	Summary and conclusions	59

Chapter 3 Accelerometer Testing and Characterisation

3.1	Introduction	60
3.2	Characterisation Equipment	61
3.2.1	White Light Interferometry	61
3.2.2	Laser Doppler Vibrometry	62
3.3	Accelerometer fabrication review of structural dimensions	64
3.3.1	Sensing gap	64
3.3.2	Comb drive.....	65
3.3.3	Support Spring	66
3.3.4	Calibration tip	67
3.3.5	Comparison of measured feature size between accelerometer types.....	67
3.4	Static deflection measurements of the electrostatically actuated accelerometers	68
3.4.1	A comparison of the static deflection measurements of accelerometer types ...	70
3.5	Out-of-plane Analysis of electrically actuated accelerometer type 1	74
3.6	Modal analysis of accelerometer types	77
3.6.1	In-plane analysis	77
3.6.2	Out-of-plane analysis of type 1 accelerometer	79
3.7	Star lab software modelling.....	81
3.7.1	Comparison of the mode shapes with FEA.....	83
3.8	Summary and Conclusions.....	84

Chapter 4 The Chemical Immobilisation and Metallisation of Deoxyribonucleic acid

4.1	Introduction	85
4.1.1	Biomolecular immobilisation and recognition.....	85
4.1.2	The chemical formation of M-DNA from pristine DNA templates	86
4.2	DNA biomolecular recognition.....	87
4.2.1	Capture based biomolecular recognition events	87
4.2.2	Surface Plasmon Resonance Biacore System	88
4.3	Ultraviolet-Visible light and fluorescent spectroscopy	90
4.3.1	The Beer Lambert law and the Optical density of DNA	90
4.3.2	The properties of fluorophores and the use for biological applications.....	91
4.4	Methods.....	95
4.4.1	Surface Plasmon Resonance and DNA Immobilisation Protocols	95
4.4.2	The λ -DNA hybridisation protocols	97
4.4.2.1	Complementary DNA Control.....	97
4.4.2.2	The λ -DNA pre-hybridised to probe B method	97
4.4.3	The closed ligated λ -DNA method	99
4.4.4	The DNA ligation validation method	99
4.4.5	DNA Metallisation protocols	100
4.5	Results and outcomes	103
4.5.1	The formation of a DNA capture layer	103
4.5.1.1	The immobilisation of DNA oligonucleotide probes on a gold layer.....	103
4.5.2	The hybridisation of non-modified Lambda DNA and control study.....	105
4.5.3	The comparison of λ -DNA hybridisation protocols	107
4.5.4	The ligation of Lambda DNA to the capture layer	109
4.6	The production of M-DNA using Zinc ion Metallisation Protocols.....	112
4.6.1	The formation of M-DNA validated by UV-VIS Spectroscopy	112
4.6.2	Zinc Perchlorate & CT DNA	113

4.6.3	The metallisation of λ -DNA	114
4.6.4	The metallisation of λ -DNA observed by a YOYO-1 fluorescence assay	116
4.6.5	Zinc Perchlorate Saturation analysis.....	118
4.7	Discussion	119
<u>Chapter 5 The positioning of YOYO-1/DNA on accelerometer substrates</u>		
5.1	Introduction	121
5.2	Methods.....	124
5.2.1	The molecular combing positioning techniques	124
5.2.2	The electrical positioning and dipping techniques.....	125
5.3	Results and outcomes	131
5.3.1	The molecular coming of YOYO-1/DNA on a glass surface	131
5.3.2	The placement of YOYO-1/DNA in the sensing gap	132
5.3.3	The DC electrophoretic positioning of YOYO-1/DNA.....	133
5.3.4	The dielectrophoretic positioning of YOYO-1/DNA	134
5.4	Conclusion.....	136
<u>Chapter 6 Summary and Conclusions</u>		
6.1	Summary	137
6.2	Discussion	137
6.2.1	A design improvement.....	139
<u>References.....</u>		<u>141</u>

List of Figures

Figure 1-1: A spring mass damper system.....	8
Figure 1-2: A Nintendo Wii wand.	8
Figure 1-3: A general illustration of an out-of-plane piezoresistive accelerometer.	9
Figure 1-4: A general illustration of a capacitive microaccelerometer.....	10
Figure 1-5: A generalised image of a capacitive microaccelerometer.....	12
Figure 1-6: The fine tunneling tip of tunneling MEMS microaccelerometer.	12
Figure 1-7: A comparison of the reported performances of the accelerometer classes.	13
Figure 1-8: The range of the microaccelerometers currently available	14
Figure 1-9: The structure of a DNA double helix.....	15
Figure 1-10: The base pairing in the DNA double helix by hydrogen bonding of the complementary strands.	16
Figure 1-11: A DNA fragment with cohesive ends that can be hybridised to complementary base..	17
Figure 1-12: The chemisorption and organisation of alkanethiols on a gold surface to form a Self-Assembled Monolayer.	20
Figure 1-13: A schematic of how a DNA nanowire is formed between electrodes using thiolated ssDNA probes anchored to the gold..	21
Figure 1-14: The hydrodynamic fluid flow stretching of DNA attached to a polystyrene bead..	22
Figure 1-15: An illustration of molecular combing of DNA using a receding meniscus.	23
Figure 1-16: An illustration and image of floating potential electrodes.	24
Figure 1-17: An AFM image of the electrical measurement device to measure the electrical conductivity.....	27

Figure 1-18: An AFM image (1.5 μ m) of silver characterised DNA between two gold electrodes.	27
Figure 1-19: An I-V curve for a silver coated DNA bridge.	28
Figure 1-20: The proposed scheme for zinc modified DNA..	29
Figure 2-1: An illustration showing a general accelerometer incorporating a DNA molecule as the sensing element.....	31
Figure 2-2: The key components of the accelerometer design	33
Figure 2-3: A higher detailed image of the mask design showing the 10 μ m gap between the gold sensing tips.....	36
Figure 2-4: The mask drawing of the calibration tip	36
Figure 2-5: The components of a comb drive to produce electrostatic actuation.....	37
Figure 2-6: The comb drive feature size of the type 1+2 accelerometer.	38
Figure 2-7: An illustration of a 5 μ m wide spring of the type 1 accelerometer.....	39
Figure 2-8: The ANSYS finite element graphical user interface highlighting the accelerometer device geometry and constraints.	41
Figure 2-9: A snap shot of Analysis	42
Figure 2-10: Analysis 1 generated from the FEA.....	42
Figure 2-11: The ANSYS static deflection modelling of a type 1 accelerometer.	44
Figure 2-12: A comparison of the static deflection values of the accelerometer types with the voltage applied.	45
Figure 2-13: A silicon surface patterned using a photolithographic mask.	47
Figure 2-14: An optical image of a micromachined MEMS Accelerometer device.	54
Figure 2-15: The gold sensing tips for the immobilisation of DNA.....	55

Figure 2-16: The calibration tip	55
Figure 2-17: The components of an SEM instrument.....	56
Figure 2-18: An SEM image of an entire accelerometer device.....	57
Figure 2-19: Two SEM images for comb drive of an accelerometer device.....	58
Figure 2-20: SEM images of the gold sensing tips.....	58
Figure 3-1: A schematic showing the fundamentals of a white light interferometer.....	61
Figure 3-2: A schematic showing the main components of a laser Doppler vibrometer system.	62
Figure 3-3: The Zygo profiler instrument and DC power supply during measurements.....	63
Figure 3-4: The sensing gap height map which shows sensing tip deflecting out-of-plane....	64
Figure 3-5: The height map of a type 1 accelerometer comb drive.....	65
Figure 3-6: The height map of a type 3 accelerometer comb drive.....	66
Figure 3-7: The support spring height map of a type 3 accelerometer.. ..	66
Figure 3-8: The calibration tip height map of a type 3 accelerometer.	67
Figure 3-9: A height map of the calibration tip of a type 1 accelerometer prior to electrical actuation.....	69
Figure 3-10: A comparison of mean deflection of comb drive 1 electrical actuation of all accelerometer types.....	70
Figure 3-11: A comparison of mean deflection of comb drive 2 electrical actuation of all accelerometer type,	71
Figure 3-12: The height map of comb 1 of the type 1 accelerometer actuated with 20 V	74
Figure 3-13: The height map of comb 2 of the type 1 accelerometer actuated with 30 V.	75
Figure 3-14: A graph showing the in-plane resonant frequency of a type 1 accelerometer. ...	78

Figure 3-15: The positions where the laser spot was focused for the out-of-plane modal frequency analysis.....	79
Figure 3-16: An illustration of mode shape 1 of Star lab vector animation at 2.44 KHz.	81
Figure 4-1: A compilation of schematics showing the possible routes of chemical immobilisation	86
Figure 4-2: An immunosensor capture layer with antigen receptors immobilised at the surface allowing capture of specific antigen taken from (Kumar 2000).	87
Figure 4-3: A Biacore biosensor system illustrating the flow channel and optical detection..	88
Figure 4-4: An example of a sensorgram that shows selective association, dissociation and regeneration.....	89
Figure 4-5: Light passing through a Cuvette containing a liquid sample.	90
Figure 4-6: The change of energy of a fluorophore and the subsequent fluorescent emission when returning to the ground state.....	92
Figure 4-7: A graph displaying the excitation and emission spectrum peaks of a fluorophore highlighting the resulting Stokes shift.	93
Figure 4-8: The chemical structure of the YOYO-1 iodide DNA specific dye.	93
Figure 4-9: A representative sensorgram which displays the addition of probe A to the gold sensor and subsequent SDS wash steps.	103
Figure 4-10: A representative sensorgram displaying the addition of 1 mM mercaptoethanol to the probe A self-assembled monolayer.....	104
Figure 4-11: A sensorgram depicting the hybridisation of λ -DNA to probe A on the sensor surface.	105
Figure 4-12: A representative sensorgram displaying the injection of a non-complementary probe and the further injection of λ -DNA to hybridise with probe A.	106

Figure 4-13: A representative chart showing a comparison between the DNA hybridisation protocols.....	107
Figure 4-14: A representative sensorgram showing the removal of hybridised λ -DNA from the surface.	109
Figure 4-15: A representative sensorgram showing the injection of the pH 13 buffer solution ligated λ -DNA on the surface..	110
Figure 4-16: A representative chart showing Calf Thymus DNA treated with 5 mM zinc perchlorate.....	113
Figure 4-17: A chart showing the A ₂₆₀ peak shift of CT DNA with varying Zn(ClO ₄) ₂ concentration.....	114
Figure 4-18: A ₂₆₀ Peak shift of λ - DNA with zinc Perchlorate concentration.	115
Figure 4-19: The YOYO-1 fluorophore excitation and emission maxima peaks when associated with Lambda DNA.	116
Figure 4-20: A comparison between the YOYO-1 emission maxima peaks between varying Zn(ClO ₄) ₂ concentration.	117
Figure 4-21: The fluorescent intensity of YOYO-1/DNA treated with ranging zinc Perchlorate concentration.....	118
Figure 5-1: The immobilisation and positioning scheme to position DNA in the sensing gap.	122
Figure 5-2: Schematics showing the procedure to place DNA in the accelerometer sensing gap by the dipping procedure with electrical positioning.....	123
Figure 5-3: A wire bonded and packaged accelerometer device in the dipping geometry....	125
Figure 5-4: The dipping station configuration	126
Figure 5-6: The 90° objective adapter attached to the microscope to allow imaging of the accelerometer.	128

Figure 5-5: A schematic of the 90° objective adaptor with internal mirror to allow imaging.
..... 128

Figure 5-7: The packaged accelerometer immersed in solution contained in the glassware that
was observed using the microscope..... 129

Figure 5-8: An image showing YOYO-1 stained λ -DNA combed on a glass slide. 131

Figure 5-9: A combined light microscope image and FITC fluorescent image using a taken
with an x50 objective lens..... 132

Figure 5-10: A combined light microscope image and a fluorescent image using a FITC filter
taken with an x100 objective and further digitally zoomed to obtain the image..... 133

Figure 5-11: An image compilation showing the dielectrophoretic positioning of YOYO-
1/DNA in the sensing gap. 134

Figure 5-12: The still images obtained from the video microscopy of the accelerometer
sensing gap before and after the electrical potential was applied. 135

List of Tables

Table 2-1: A list of the variation in the dimensions of the types of accelerometer.	35
Table 2-2: The mode shape frequencies for Analysis 1 and 2.	43
Table 2-3: The silicon die device layer properties.	49
Table 3-1: A comparison showing the dimensions specified for the accelerometer types and the actual measured dimensions.	67
Table 3-2: A comparison of the performance of the accelerometer types.	72
Table 3-3: A comparison of the measured static deflection of the accelerometer types with the predicted modelled values using ANSYS.	73
Table 3-4: A comparison of the in-plane mean modal frequencies measured for all accelerometer types.	78
Table 3-5: The mode frequencies for measured out of plane deflection for the type 1 accelerometers.	80
Table 3-6: The mode shapes of FEA modelled and an actual modeshape of a type 1 accelerometer.	82
Table 3-7: A table comparing the two matching modes between the measured data and the FEA results.	83
Table 4.1: the specifications of the oligonucleotide probes used in the hybridisation studies.	95
Table 4.2: The specifications of the oligonucleotide probes used for the hybridisation protocols.	96
Table 4.3: The fluorescent values of YOYO-1/DNA and $Zn(ClO_4)_2$ concentration.	119

List of Equations

Equation 1-1: The dynamic behaviour of a spring mass damper system.

Equation 1-2: The quality factor.

Equation 1-3: The natural frequency of a spring mass damper system.

Equation 1-4: Hooke's law equation.

Equation 1-5: The mechanical gauge factor.

Equation 1-6: The thermal noise equivalent acceleration.

Equation 1-7: The tunneling current calculation.

Equation 2-1: The calculation of the electrostatic force of a comb drive actuator.

Equation 4-1: The optical excitation of a fluorophore.

Equation 4-2: The optical emission of a fluorophore.

Equation 4-3: The calculation to determine the amount of YOYO-1 dye with DNA (ratio).

List of Abbreviations

AC = Alternating Current

AFM = Atomic Force Microscope

ATR = Attenuated Total Reflection

BRE = Biological Recognition Element

CT-DNA = Calf Thymus DNA

DC = Direct Current

DNA = Deoxyribonucleic Acid

DRIE = Deep reactive ion Etching

EDTA = Ethylenediaminetetraacetic acid

FEA = Finite Element Analysis

MCE = β -Mercaptoethanol

MEMS = Micro Electro Mechanical System

M-DNA = Metallised DNA

O.D. = Optical Density

PECVD = Plasma Enhanced Chemical Vapour Deposition

Q Factor = Quality Factor

RU = Response Units

RFU = Relative Fluorescent Units

SAM = Self Assembled Monolayer

SDS = Sodium Dodecyl Sulphate

SEM = Scanning Electron Microscope

SPR = Surface Plasmon Resonance

SOI = Silicon on Insulator

SPP = Surface Plasmon-Polaritons

Tris = Trizma base

UV-Vis = Ultraviolet - Visible

YOYO-1 = YOYO-1 iodide fluorescent dye

YOYO-1/DNA = YOYO-1 labelled DNA

YOYO-1/DNA+B = YOYO-1 labelled DNA with probe B hybridised

Zn-P = Zinc Perchlorate

μ g = Microgram

λ -DNA = Enterobacteriophage Lambda DNA

1 Chapter 1 General Introduction

1.1. Inertial Navigation Systems and Accelerometers

The evolution of Inertial Navigation Systems (INS) has been short but intense due to the advancement in technology of the cold war (Grewal 2001). The development of microelectromechanical systems (MEMS) could help to develop future INS technology. The future progression of the technology may provide affordable, lightweight and highly sensitive sensor systems for military and commercial purposes.

1.1.1 Inertial navigation systems

“Provide the position, velocity, orientation, and angular velocity of a vehicle by measuring the linear and angular accelerations applied to the system in an inertial reference frame. It is therefore immune to jamming and deception” (Titterton 2004).

The purpose of an inertial navigation system is to determine the position and velocity of a vehicle based on the physical laws of nature, without the need to rely on external factors such as a global navigation satellite system (GNSS). Inertial navigation is based on Newton's law of motion which states that a body in motion maintains its motion unless acted on by a force.

INS can contain accelerometers incorporated into their design that allows the determination of the vehicle velocity in its inertial reference frame. This allows the precise and accurate position of the vehicle to be calculated. The drawback of INS being that they can experience inertial drift, where for current commercial systems the standard drift is approximately 0.6 nautical miles per hour due to small sensing errors of the velocity (King 1997). The use of GNSS is becoming extremely popular due to its packaging into easy to use systems such as automobile satellite navigation systems. The signal can be easily jammed from transmitting on the same frequency at a low radio transmission power (Grant, Williams et al. 2009). The UK and US military employ a more accurate version of GNSS than civil receivers, though they can still be highly sensitive to radio jamming by an enemy force. Therefore from a military point of view; the navigational interference of a military vehicle such as a sea faring vessel, aircraft or missile may cause tactical errors. The development of highly accurate INS has been researched by the military for this purpose, to allow the accurate navigation of vehicles in the theatre of war. Also they have an abundance of commercial applications such as for game controllers, autonomous automobile and robotic navigation.

1.1.2 Accelerometers

Accelerometers can measure the acceleration and vibration of an object. An accelerometer contains a spring mass damper system where the position of the proof mass is relative to the accelerometer casing that can be measured to determine acceleration (Farell 1999). An acceleration event causes an inertial force that causes the proof mass to be displaced; the amount of displacement can be measured to determine the value of acceleration. Most usually a transducing element is used to convert the mechanical displacement to an electrical output. There are a range of accelerometers available that use varying transduction elements to measure inertial force such as piezoresistive, capacitive and tunneling current fluctuation. The proof mass of an accelerometer is generally supported by elastic flexures (support springs) along with a dampening system to restore the mass to its neutral position and allow the mechanical oscillation to decay. A common application of an accelerometer is the use in an automobile airbag system. The accelerometer measures the deceleration of the vehicle where if it reaches a certain value during a collision the airbag is activated. Accelerometers have been produced using two methods; macromechanical and micromechanical. The macromechanical class are made by conventional techniques that are expensive to manufacture which can be big and bulky in size. They require regular calibration if undergoing frequent use at a monetary and time cost. They generally operate at high voltage/current, requiring a dedicated power source, therefore limiting versatility for small autonomous systems.

The micromechanical accelerometer (microaccelerometers) class are accelerometers that are produced using microfabrication technology that allows batch production. The latest microaccelerometers are replacing the majority of conventional sensors as they are small, cheap and lightweight that offer better performance.

1.1.3 Acceleration Principles

The value of acceleration is the change of velocity with time where Newton's second law states that 'for a body with constant mass, acceleration of the body is proportional to the net force acting on it'. Velocity is a vector that describes the direction and the magnitude of an object.

The dynamic behaviour of a spring mass damper system due to external acceleration can be calculated by the second order dynamic differential equation as in equation 1-1;

$$F = m \frac{d^2 \Delta y_m}{dt^2} + b \frac{d \Delta y_m}{dt} + k \Delta y_m$$

[1-1]

where m is the mass, k is the spring constant Δy_m is the change in displacement and b is the damping coefficient

1.1.4 Quality Factor

The quality factor (Q factor) defines the properties of an oscillator, it describes the bandwidth compared to the resonant frequency. A high Q value means that the system suffers from a lower rate of energy loss relative to the stored energy whereas a low Q indicates that there is energy loss in the system, hence a low Q indicates that the resonator is not as efficient as a resonator with a high Q. In the terms of a spring mass damper system of an accelerometer it describes the air drag that will be proportional to the system velocity, the equation to derive Q factor is presented in equation 1-2;

$$Q = \frac{V_0}{\delta V}$$

[1-2]

where V_0 is the resonant frequency and δV is the full width half maximum bandwidth of the resonance. An accelerometer with a high Q will be more energy efficient. The resonant frequency or the Q factor will depend on the damping. The suspension of the springs (spring constant) do not affect the resonant frequency and Q factor of the accelerometer proof mass.

1.1.5 Accelerometer resonant frequency concepts

In theory a spring mass damper system of an accelerometer only has one resonant frequency as it only has one degree of freedom. This resonant frequency is achieved when the system absorbs energy at the natural vibration oscillation frequency; the potential energy is converted to kinetic energy giving high amplitude at a certain frequency. This means that the system oscillates at greater amplitude at a certain frequency, giving a peak at the resonant frequency. The spring mass damper system will lose energy over time that is caused by damping indicated by the Q factor. The natural frequency of a spring mass damper system of an accelerometer is determined by the mass and stiffness of the support springs

$$f = \frac{1}{2\pi} \sqrt{\frac{k}{m}}$$

[1-3]

The natural frequency can be calculated with the formula in equation 1-3, where ***m*** is the mass and ***k*** is the spring constant. The architecture of an accelerometer is highly dependent on the application that it will be used.

1.1.6 Spring constant and Hooke's Law

When a mass is added to a spring mass damper system it becomes a harmonic oscillator, using Hooke's law the natural frequency can be calculated. The most commonly used version of Hooke's law is stated in equation 1-4;

$$F = -kx$$

[1-4]

where F is the restoring force, X is the displacement of the spring from its equilibrium point and $-k$ is the spring constant. The spring constant may have a negative value due to acting in the opposite direction of displacement to return to the equilibrium point. The illustration in Figure 1-1 shows a spring mass damper system of a harmonic oscillator where the mass (m) is held by the spring where the motion is reduced by the dashpot due to the viscous damping coefficient (c).

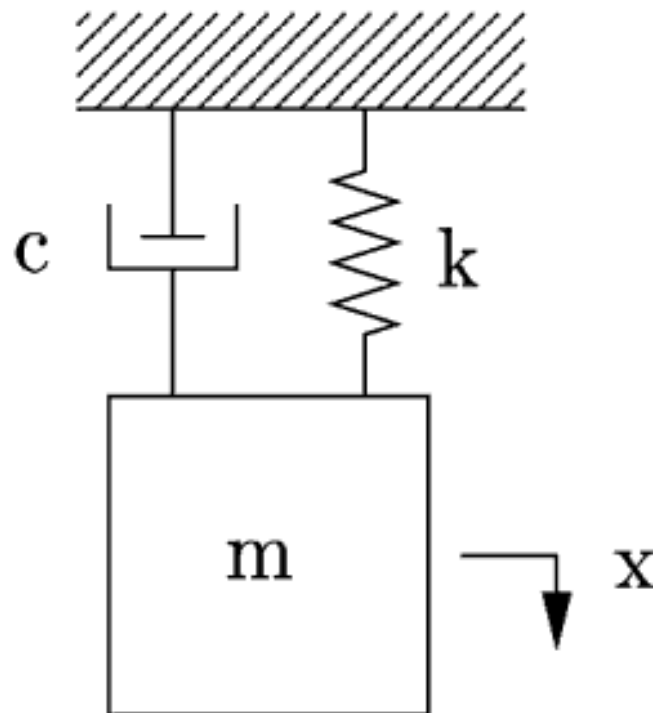


Figure 1-1: An illustration of a spring mass damper system of a harmonic oscillator.

1.1.7 Mechanical Gauge Factor

The gauge factor is the ratio of change in electrical resistivity of a strain gauge with relation to mechanical strain. A piezoresistive accelerometer takes advantage of this by exploiting a Wheatstone bridge to measure strain. Equation 1-5 below gives the change in gauge factor (GF) due to the change in length of the material.

$$GF = \frac{\Delta\rho}{\rho \varepsilon}$$

[1-5]

Where ε is the strain, ρ is the unstrained resistance and $\Delta\rho$ is the change in strain gauge resistance.

1.1.8 Calculation of noise acceleration from Newton's 2nd Law

The total noise caused by Brownian motion of the proof mass relative to the fixed frame and surrounding air can be calculated by equation 1-6 below;

$$TNEA = \frac{\sqrt{4k_B T D}}{M}$$

[1-6]

where $TNEA$ is the 'thermal noise equivalent acceleration, k_B is the Boltzmann constant, T is the temperature, D the damping factor and M is the proof mass.

1.1.9 Fundamentals of accelerometer design

The manufacturing of a novel microaccelerometer can be designed to its specific use as many factors can influence the performance of an accelerometer. The different classes of accelerometers that are available contain varying properties regarding performance. The parameters that are considered when designing an accelerometer are as follows;

- **The sensitivity**- is measured in Farads per gee (F/G) or Volts per gee (V/G) which gives an indication of the change of the electrical properties with regards to external acceleration. The larger the change in electrical properties for a given acceleration the more sensitive the accelerometer.
- **The resolution**– gives an indication of the smallest increment of acceleration that can be measured taking into account the noise floor.
- **The dynamic range (+/- gee)** - gives an indication of the operating gee of the accelerometer that allows it to measure external acceleration. The dynamic range being an important choice for the application required. Outside this range the accelerometer will fail to function.
- **The bandwidth**- the range in which the resonant frequency of the accelerometer can measure accurate acceleration.
- **The minimum detectable acceleration (milli-gee)** - indicates the minimum acceleration that can be detected. When designing an accelerometer the minimum detectable acceleration may be influenced with the application needed. Tunneling accelerometers offering the most efficient detection of small acceleration values.

1.1.10 MEMS Microaccelerometers

Microaccelerometers have become widely used in an array of technology whether it be navigational systems or highly manufactured commercial devices. The commercialisation of the product has caused millions of microaccelerometers to be sold worldwide every year. They have large advantages compared to conventional accelerometers such as being lightweight, batch fabricated, low cost and low power consumption allowing them to be consolidated onto an integrated circuit (IC). The Nintendo Wii games console wand contains an 3 axis microaccelerometer which measures movement of the players arm that is interpreted into the game which is displayed on the screen (Nintendo 2006). The image in Figure 1-2 shows the 3 axis sensitivity of the wand; highlighting the pitch, yaw and roll angles. The Apple iphone also contains an microaccelerometer (Apple 2010) that allows the orientation of screen display to change when the phone moves from portrait to landscape orientation. The main classes of transducing elements of accelerometers include piezoresistive, piezoelectric, capacitive and tunneling.

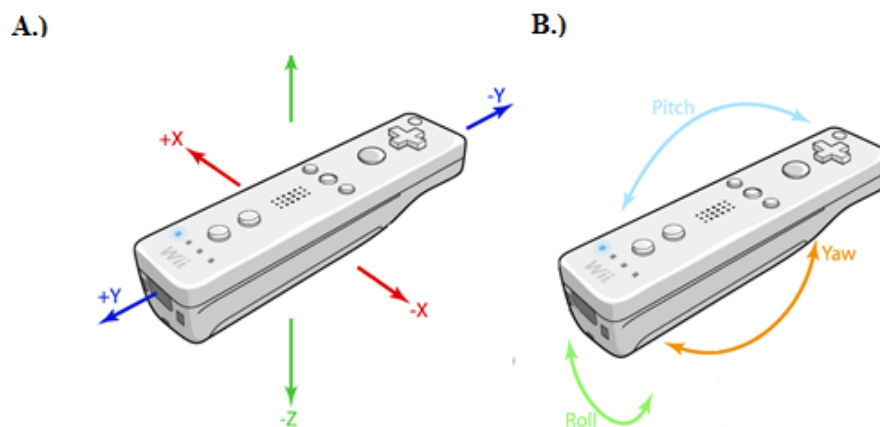


Figure 1-2: A.) A Nintendo Wii wand that utilises accelerometer technology for movement detection showing the 3-axis of orientation. B.) The pitch, yaw and roll angle of the wand.

Images adapted from (HacknMod.com 2011)

1.1.11 Piezoresistive Microaccelerometers

The piezoresistive microaccelerometer is a commercially successful product. It was first designed in 1979 by Roylance and Angell (Roylance and Angell 1979) using silicon microfabrication techniques. This class of accelerometer has been used extensively in avionics due to its operation at a 'high gee'. It is not susceptible to electromagnetic interference (EMI) allowing it to be used for space applications without the need for custom

packaging. An accelerometer of this class is generally manufactured where the proof mass attached to a cantilever beam deflects out-of-plane as shown in Figure 1-3. The cantilever beam moves relative to the proof mass due to acceleration causing the suspension beam to undergo strain. The change in stress of the cantilever beam due to acceleration will be detected by the change in resistivity of the piezoresistors. The piezoresistors are placed between the support rim and proof mass for maximum detection of stress due to the acceleration event. The change of electrical resistivity of the piezoresistor due to linear acceleration being the transducing element that allows acceleration to be measured. This class of accelerometer is generally a simple design that does not suffer from parasitic capacitances unlike other classes of commercial microaccelerometers. The drawback is the fact that they can be sensitive to temperature drift, with the need for temperature compensation elements to be employed. The piezoresistive class are generally used for ‘high gee’ applications (Ning, Loke et al. 1995).

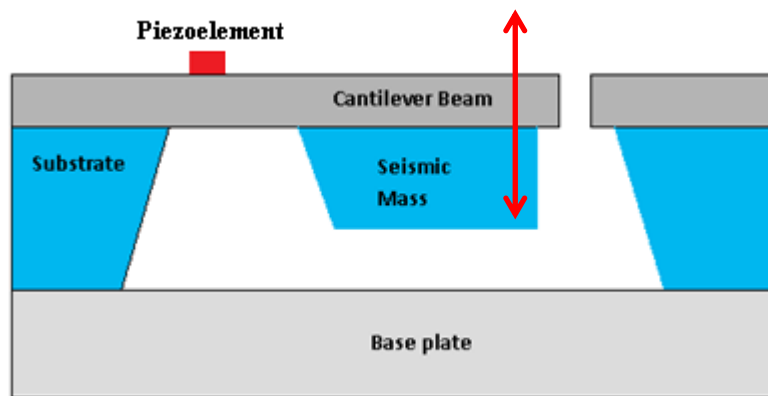


Figure 1-3: A general illustration of an out-of-plane piezoresistive accelerometer.

1.1.12 Piezoelectric Microaccelerometer

The piezoelectric microaccelerometer class has subtle differences to its piezoelectric counterpart. The piezoelectric accelerometer is based on the same acceleration detecting principle as piezoresistive though the transducing element is somewhat different. As displayed in Figure 1-3 the cantilever beam and proof mass are displaced due to external acceleration, the displacement of the proof mass causing strain in the cantilever beam, where for this class a piezoelectric sensing element (piezoelement) will allow acceleration to be determined. Piezoelectric accelerometers are used for measuring shock and vibration where they are capable of measuring with a good range and high sensitivity.

1.1.13 Capacitive Microaccelerometers

Capacitive microaccelerometers have been commercialised because they are capable of operating at low and high gee, allowing for use in the avionics and automobile industry. This class of accelerometer is commercially sold mostly for higher gee applications due to high sensitivity in this range. The capacitive microaccelerometer is based on a gap variation between a proof mass and a fixed electrode that varies capacitance uniformly due to acceleration. The illustration in Figure 1-4 shows a general capacitive microaccelerometer, illustrating the proof mass held between two counter electrodes by the suspension beam. The change of capacitance in the sensing axis due to the displacement of the proof mass is calculated to give the value of acceleration. This class of microaccelerometer has been said to suffer from parasitic capacitance in some designs that can affect the performance of the device, due to the high noise floor. They do not suffer from temperature sensitivity problems that can be common with the piezoresistive class that does not allow them to be used in diverse environments such as for use in deserts and arctic conditions. The application of electronic shielding needs to be undertaken in some circumstances, as this class of accelerometer can be sensitive to EMI making it unsuitable for certain applications. The use of capacitive accelerometers is used commonly for inertial navigation purposes.

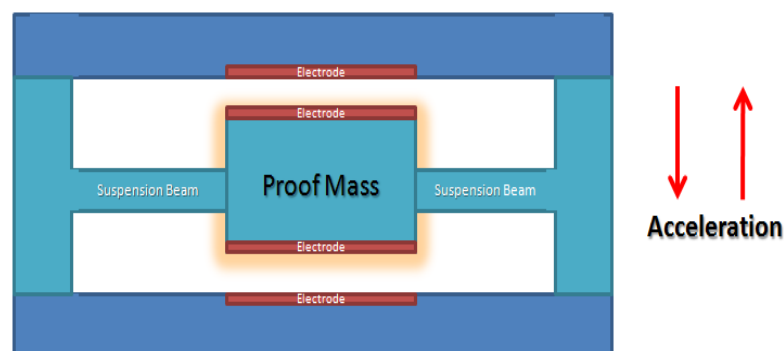


Figure 1-4: A general illustration of a capacitive microaccelerometer within its axis of acceleration.

1.1.14 Tunneling Microaccelerometers

The phenomena of quantum mechanical tunneling has been theorised and investigated since the 19th century. Research into tunneling was started at the time of the discovery of radioactive natural decay by Henri Becquerel in 1886 (Halibel 2008). Tunneling is described where a particle can travel through a barrier that it could not usually pass because its kinetic

energy is lower than the potential energy required to pass. The theory was further investigated by Pierre and Marie Curie who won the Nobel Prize (Halibel 2008) for their work on this subject.

Quantum mechanics states that an electron has a non-zero probability of passing through a barrier through a physical barrier; this is regardless of whether the potential energy of the barrier is greater than the kinetic energy of the electron. This theory has been explained using the Heisenberg uncertainty principle (Hensinger, Haffner et al. 2001) that states that precise inequalities of certain pairs of physical properties such as position and momentum can't be known precisely (Heisenberg 1927). Hence if one property is measured precisely the other property will not. The rate of acceleration in a tunneling microaccelerometer causes the relative displacement of the proof mass and change in tunneling current properties that can be calculated by the exponential dependence as shown in equation 1-7.

$$I_t \propto V_B \times \exp(-\alpha_I \sqrt{\Phi \chi_{tg}})$$

[1-7]

where V_B is the tunneling bias across the tunneling gap, α_I is the tunneling constant at $1.025 (\text{\AA}^{-1} \text{eV}^{-0.5})$, Φ is the effective height of the tunneling barrier or the effective work function, χ_{tg} being the shortest tunneling gap between tunneling tip and the proof mass electrode and I_t being the tunneling current.

1.1.14.1 Tunneling Class Microaccelerometer operation

This class of microaccelerometer has been shown to operate with high sensitivity with a resolution of 'nano gee'. The maximum input acceleration is in the 'milli gee' range, though offering a high bandwidth and reduced size. They operate by using a cantilever tip where the deflection electrode deflects the proof mass on a spring by electrostatic voltage to the tunneling position. The suspension beam is held in position using a servo system that maintains the critical gap between the tip and the deflection electrode. This causes the proof mass to move back to the zero position to maintain the tunneling current. The proof mass is displaced due to acceleration and the circuit responds to the change of tunneling current, adjusting the voltage of the deflection electrode. The illustration in Figure 1-5 displays the key feature of a tunneling microaccelerometer. To maintain the tunneling current a 2\AA gap is

achieved by a closed loop system, as maintaining the tunneling position is crucial for operation. A displacement of an Ångstrom can cause a current change with exponential behaviour which can make a huge change in the tunneling current. The acceleration is quantified by the change in voltage of the deflection electrode system to maintain the tunneling position. The current range of tunneling microaccelerometers offer sensitivity at ‘low gee’ but poor range at ‘high gee’ that makes them less favoured for commercial applications, as many uses are in the field of automotive and aeronautical systems that require sensitivity and high resolution at high gee. The advantages of tunneling microaccelerometers are the fact they have one degree of freedom, offering a high bandwidth that suffer from less noise effects.

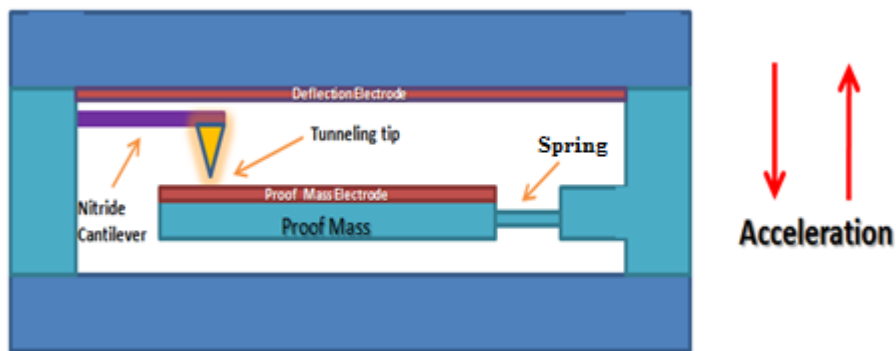


Figure 1-5: A generalised image of a capacitive microaccelerometer within its axis of acceleration.

The SEM image in Figure 1-6 shows a tunneling tip of tunneling microaccelerometer that has a tip plane area smaller than $0.1 \mu\text{m}^2$ that was fabricated by wet chemical etching microfabrication techniques (Dong, Jia et al. 2005).



Figure 1-6: The fine tunneling tip of tunneling MEMS microaccelerometer. The scale bar being 1 μm . Taken from (Dong, Jia et al. 2005).

1.1.15 The performance of Microaccelerometers

A comparison of the reported performances of the various accelerometer classes are highlighted below in Figure 1-7. The most commonly produced being the tunneling and capacitive class.

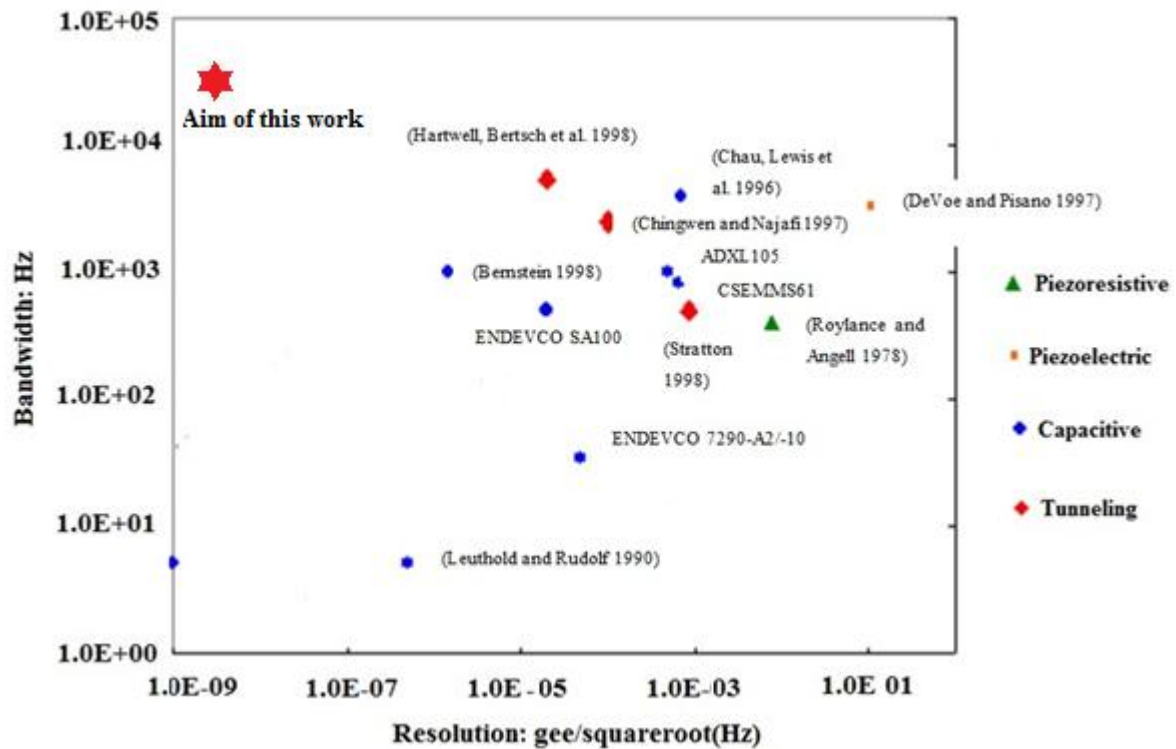


Figure 1-7: A comparison of the reported performances of the accelerometer classes discussed.

As can be seen no class can operate across the whole dynamic range, hence an accelerometer must be chosen carefully to fulfil the application required.

1.1.15.1 Can biological accelerometers be the next future class?

The progression of nanotechnology has allowed a crossover of disciplines that has allowed more technology development. Novel multidisciplinary research has been performed in a wide range of areas, but engineering life sciences have been a major driving force in many instances. Many biological molecules are well characterised making them ripe for exploitation outside their natural environment and applied in highly novel ways. The chemical placement of biological molecules on microfabricated devices can be performed to assemble biological MEMS (Bio-MEMS) (Herne and Tarlov 1997; Levicky, Herne et al. 1998; Steel, Levicky et al. 2000). This may allow the next class of accelerometers to be

realised using biological molecules to act as the sensing element which is discussed further in chapter 2.

This research has focused on the production of a biological accelerometer using deoxyribonucleic acid (DNA) as the sensing element. A biological accelerometer could allow sensitivity at low-high gee, allowing it to surpass the technology previously described. The use of a DNA as a mechanical strain gauge in an accelerometer may allow the molecule to have a large gauge factor. This may allow this hybrid biological accelerometer sensor to cover the entire dynamic range of what is presently commercially available, as highlighted in Figure 1-8.

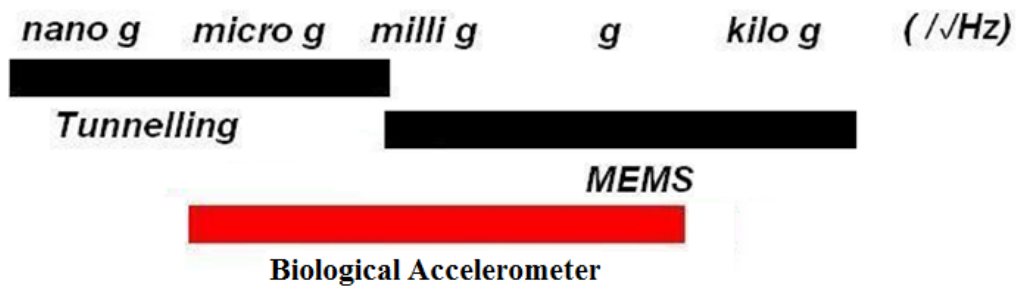


Figure 1-8: The range of the microaccelerometers currently available whilst also highlighting the aim of this research.

1.2 The discovery and properties of the DNA molecule

DNA is a simple, well characterised molecule which properties have been utilised in novel situations (Braun, Eichen et al. 1998; Aich, Labiuk et al. 1999). It is a central tool for many nanotechnologists, material scientists and biotechnologists wishing to create a recognition interface. The DNA molecule is well characterised due to nearly 60 years of precise research.

1.2.1 The short history and discovery of DNA properties

The DNA molecule was first discovered by the Swiss scientist Friedrich Miescher in 1869, who described it as microscopic puss (Dahm 2005). The substance was named ‘Nuclein’ as it was derived from the nuclei of cells. Phoebus Levene in 1919 suggested that DNA consisted of a series of nucleotides made from sugars in a repetitive fashion held together by phosphate groups (Levene 1919). The main role of DNA was realised in 1952 when Alfred Hershey and Martha Chase proved that DNA is hereditary genetic material with experiments using the T2 phage (Hershey and Chase 1952). In 1953 Watson and Crick proposed the structure of the

DNA double helix as we know it today as illustrated in Figure 1-9 and Figure 1-10 (Watson JD 1953).

1.2.2 The Structure of the DNA double helix

DNA is a right handed double helix molecule held together by complementary base pairs. DNA is simply two polymers containing a sugar phosphate backbone and organic bases wound around each other in a defined structure. The specificity of the bases presents DNA with its replication and recognition abilities. The pyrimidine aromatic bases Thymine (abbreviated T) and Cytosine (C) base pair with the purine bases Adenine (A) and Guanine (G) through hydrogen bonds in the centre of the double helix. The base pairing between A and T contains two hydrogen bonds whereas G and C are paired by three hydrogen bonds. The DNA molecule is 2.2 to 2.6 nm wide with 0.34 nm between each. A nucleotide being a nitrogenous base linked to a five carbon pentose sugar (2-deoxyribose) and two phosphate residues as shown in Figure 1-9 and Figure 1-10 where each sugar is joined by a phosphodiester bond.

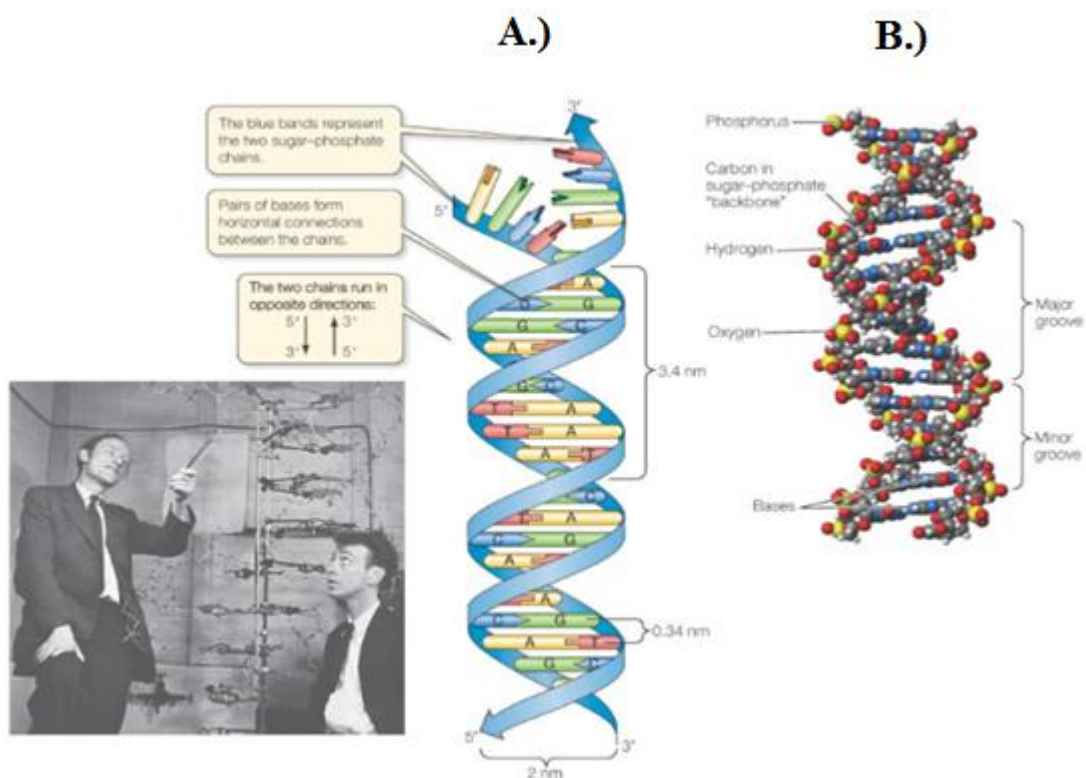


Figure 1-9: A.): The structure of a DNA double helix with complementary pairing between bases. B.): The detailed information on the grooves of the DNA molecule and position of bases and sugar phosphate backbone. Inset: Watson and Crick with the first proposed model of the DNA double helix in 1953. Image adapted from (Pray 2008).

The DNA molecule can exist naturally thousands to millions of base pairs long, allowing them to be manipulated for nanotechnology techniques. The molecule has asymmetric ends that can be 3 prime (3 ') or 5 prime (5'), 3' being a terminal hydroxyl group and the 5' end having a terminal phosphate residue. The sugar phosphate backbone is polyanionic allowing electrostatic interactions with cationic molecules along the DNA template. The DNA molecule contains spaces between the antiparallel helical strands known as grooves. The DNA polynucleotide contains two types of groove; the major groove that is 2.2 nm wide and the minor groove 1.2 nm wide. The grooves can act as binding sites especially the major groove that due to the size can be more accessible. Proteins such as transcription factor can bind to do the DNA molecule in this manner. The grooves have also been used for the modification of the DNA molecule to investigate electrical conductivity (Dong, Hollis et al. 2007).

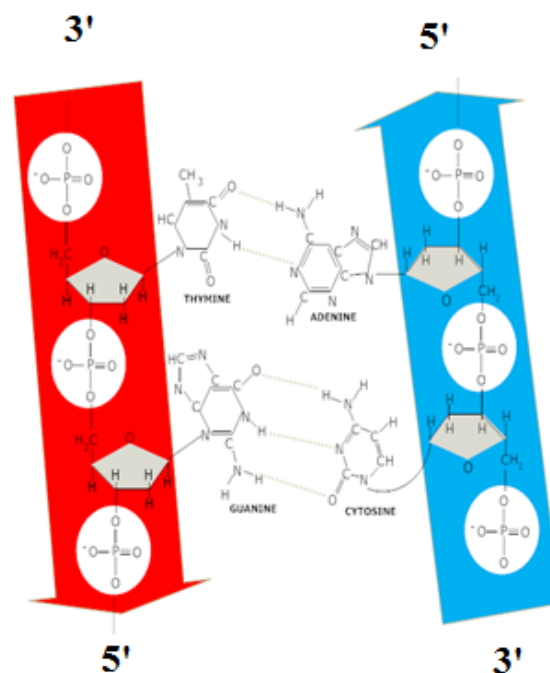


Figure 1-10: The base pairing in the DNA double helix by hydrogen bonding of the complementary strands.

Genetic material exists in all living organisms, resulting in protein translation to give phenotypical identity but abundant research has also been performed where DNA is used as a generic building material. It is increasingly becoming of interest as basic building blocks for 'bottom up fabrication', this being the building up of a desired feature using small fundamental constituent parts usually by self-assembly.

1.2.3 Complementary DNA Hybridisation

The complementary base pairing that holds together the two helices in the DNA molecule can be exploited for bottom up approaches. When DNA strands are intentionally associated in-vitro by complementary base pairing it is known as hybridisation. Many types of DNA isolated from a range of hosts exist in a circularised form that once linearised contain ssDNA overhangs known as cohesive ends (sticky ends) that can hybridise to a complementary DNA sequence by hydrogen bonding. The illustration in Figure 1-11 shows cohesive ends of DNA that hybridise together by Watson and Crick base pairing. Hybridisation will only occur if the target has the same correct corresponding DNA base sequence.

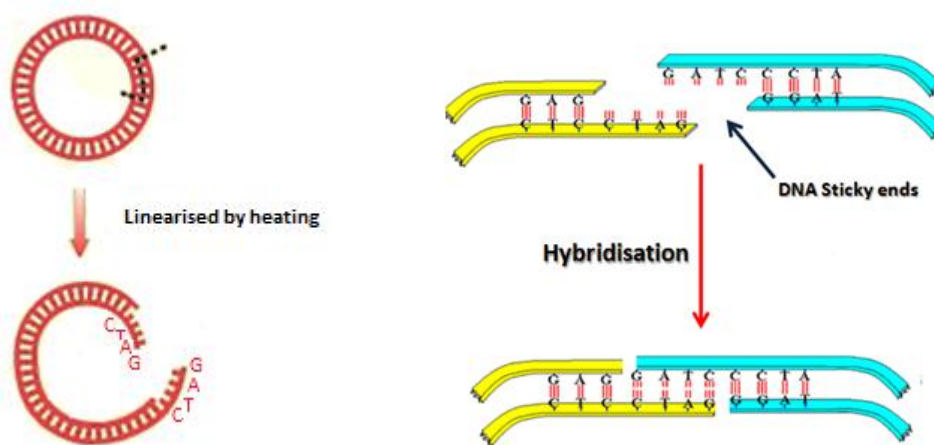


Figure 1-11: A DNA fragment with cohesive ends that can be hybridised to complementary base adapted from ref (Slic2 2005).

Once DNA has hybridised to a complementary target strand it can be further modified along the sugar phosphate backbone that still has a “nick”. This means that a phosphodiester bond is broken along the backbone. To repair the phosphodiester bond a method called DNA ligation is commonly undertaken. The procedure is regularly used in molecular biology to repair single stranded discontinuities in double stranded molecules. It is performed by using the natural enzyme DNA ligase which was first documented in 1968 (Weiss, Jacquemin-Sablon et al. 1968). This may allow the DNA molecule to be more robust to mechanical stress and environmental factors.

1.2.4 Enterobacteriophage Lambda DNA

Enterobacteriophage Lambda (λ phage) is a temperate bacteriophage that was discovered in 1951 by Esther Lederberg who was a scientist from New York. He was an avid molecular biologist that accidentally discovered Lambda phage in 1951 and in 1953 (Lederberg 1951)

(Lederberg and Lederberg 1953). Much research was done on lambda phage over the many years since its first discovery by Lederberg. The lambda phage genome (λ -DNA) is well characterised allowing it to be manipulated for a variety of purposes. The genome can be accessed online (NCBI 2007) containing a host of genetic information regarding lambda DNA. The λ -DNA contains single stranded sticky ends when linearised from its circular form, allowing it to anneal to complementary DNA molecules. This property has been widely exploited for specific immobilisation of DNA on substrates (Alivisatos, Johnsson et al. 1996; Mirkin, Letsinger et al. 1996; Braun, Eichen et al. 1998). The crystallographic length of λ -DNA is 16.2 μm (Lederberg and Lederberg 1953), the availability of this engineering parameter makes it a good model in microscale systems, easing fabrication tolerance that would be a problem with short DNA molecules.

1.2.5 The DNA molecule as a generic material

The use of DNA as functional molecular wire (DNA nanowires) has been of some interest in the past years. DNA is suitable for nanowire assembly because of the size, organised structure and molecular recognition ability of the molecule (Gu, Cheng et al. 2006). The molecular recognition of DNA allows nanowires to be selective placed on microfabricated structures. This research has been furthered by using the DNA as a metal addition and electrical functionality. The application of sequence specific lithography has also been performed using DNA for the developmental fabrication of field effect transistors (FET'S) and interconnection of nanoelectronic circuits (Keren, Krueger et al. 2002).

The application of a fabricated DNA nanowire could potentially produce nanoscale self-assembling electronic systems. DNA nanowires have been promoted to produce the next generation biological microelectromechanical systems (BioMEMS). Research has been undertaken into fabricating DNA nanowires for the construction of novel biological systems (Braun, Eichen et al. 1998; Mbindyo, Reiss et al. 2001; Richter 2001). A novel application may be the assembly of a physical measurement system that exploits nanowire synthesis, allowing DNA to be used as a strain gauge for a biological microaccelerometer. In the literature λ -DNA is most frequently employed when preparing DNA nanowires for these exciting applications.

1.3 Chemical Self Assembled Monolayers

Self-assembled monolayers (SAMS) are 2-dimensional structures which form by chemisorption of functional molecules on to a substrate. SAMS are used for their ability to immobilise a variety of molecules onto an array of substrates. This allows the self-assembly of immobilised biomolecules onto a microfabricated surface. There is much chemistry that has been investigated allowing chemical immobilisation of SAMS on substrates such as; thiol (Braun, Eichen et al. 1998; Germishuizen, auml et al. 2003), biotinylation (Zimmermann and Cox 1994) and organosilanes (Chrissey, Lee et al. 1996) to mention a few. The popular protocol for SAM immobilisation is the thiol, allowing covalent tethering of molecules to the target noble metal substrate.

1.3.1 Organosulphur Alkanethiol SAM Layers on Gold

An alkanethiol contains a sulphur and hydrogen atom (-SH) linked to a hydrocarbon chain; it is a sulphur analogue of an alcohol group often called mercaptans. Thiols covalently attach to gold spontaneously through the sulphur atom to form epitaxial bonding (Laibinis 1991). An Alkanethiol ($X-(CH_2)_n-SH$) contains a functional group which is denoted X, the end functional group can be used to bind a multitude of chemical crosslinkers that have been used in a numbers of ways (Piscevic, Knoll et al. 1995; Steel, Levicky et al. 2000; Peelen and Smith 2004). The hydrogen atom is lost when the sulphur atom binds to the gold which has been argued to be lost as di-Hydrogen or H^+ as it can occur in the absence of oxygen (Ulman 1996). The gold thiolate bond is strong with high stability, the homolytic bond strength being 44 Kcal/mole (Linkopings 2007). Alkanethiols covalently anchored to a gold surface have a 30° tilt between the backbone and the surface normal. A reason for this is the gold surface causes the thiols to form a lattice constant of 0.50 nm whereas the alkyl chain are only 0.42 nm in diameter; therefore filling the space by tilting (Butt 1993). Alkanethiols form monolayers on a crystalline gold surface with orientation in the (111) direction (Nuzzo, Zegarski et al. 1987). It has been demonstrated that with increasing time, monolayers become more organised due to steric, electrostatic and van der Waals lateral interactions (Steel, Levicky et al. 2000).

George Whitesides first understood the potential of using thiol chemistry to form a monolayer. In 1989 Whitesides co-authored a scientific communication (Bain 1989), in which he discussed the properties of the thiols to form thin monolayers on gold. The ability of the thiol bond has allowed a range of molecules to be immobilised on gold using varying

protocols. The image in Figure 1-12 shows alkanethiols immobilised on a gold substrate with a 30° tilt to the surface normal and highlighting the ability to incorporate a functional group on the alkanethiol. The functional group can be varied depending on the application needed, though DNA oligonucleotides are commonly employed for DNA microarray analysis or DNA nanowire construction.

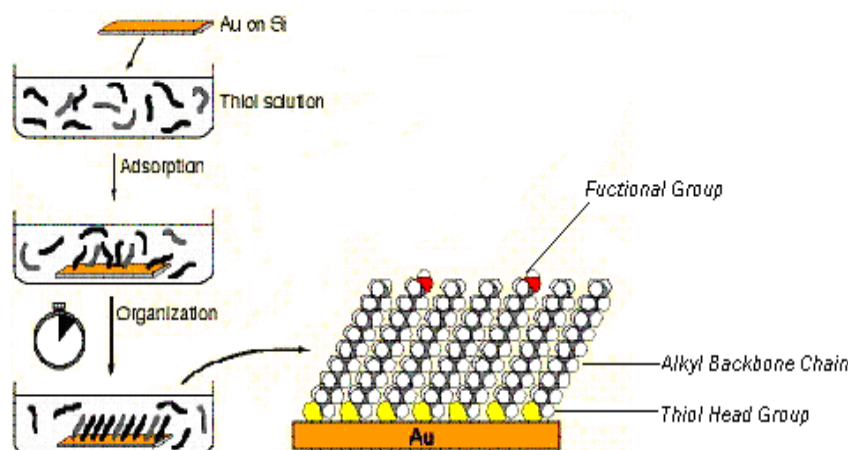


Figure 1-12: The chemisorption and organisation of alkanethiols on a gold surface to form a Self-Assembled Monolayer. Picture adapted from ref. (Linkopings 2007).

1.3.2 DNA Self-Assembled Monolayers on gold

The earlier alkanethiol research performed gave researchers the idea of modifying DNA oligonucleotides with thiol analogues to make an orientated monolayer on gold. To incorporate the thiols spacers (C3 or C6) were used between the thiol and DNA bases,. More recently the spacers have been questioned to present a barrier for electron transfer (Zhang 2002). The DNA probe immobilised on the surface will have a complementary sequence to a target molecule, allowing hybridisation of DNA molecules on the substrate surface. This approach can be used to place longer DNA molecules onto a surface, for example DNA nanowire formation (Braun, Eichen et al. 1998).

DNA SAM organisation and hybridisation has been investigated in detail over the years to which thiolated probe density (Peterson, Heaton et al. 2001), DNA probe immobilisation time and probe length (Steel, Levicky et al. 2000) have all been investigated on the ability to make an organised monolayer. Thiolated oligonucleotides less than 24 base pairs, have been shown to have better hybridisational efficiencies than longer molecules (Steel, Levicky et al. 2000). This could be due to the formation of rod like structures in an upright geometry, allowing

DNA to be highly accessible for hybridisation. The efficiency using DNA above 24 base pairs in the same study showed a decline. Mercaptoethanol (MCE) is an alkanethiol that is commonly used when preparing DNA SAMS, backfilling plain gold so that DNA does not nonspecifically bind to the surface. When MCE is mixed to the monolayer, the probe density is said to be reduced. The treatment with MCE may cause the probe DNA to extend further into solution causing a less constrained tethered geometry which makes the probe highly accessible for hybridisation. It has been suggested that this is due to steric and electrostatic interactions of the alkyl chain. MCE can displace non-specifically bound DNA probes to be from the surface increasing monolayer quality (Steel, Levicky et al. 2000).

1.4 DNA Nanowire Fabrication, modification and Characterisation

DNA nanowires have been deposited on various substrates such as silicon (Liqin Dong 2007) or gold (Braun, Eichen et al. 1998). In 1998 at a research institute in Israel, a particular attractive approach was used by Erez Braun and co-workers who fabricated a λ DNA nanowire between a micro gap that consisted of two gold electrodes that were 12-16 μm apart (Braun, Eichen et al. 1998). In the study, the use of self-assembled monolayers was employed to immobilise a 12 base complementary ssDNA probe (Oligo A) to one gold electrode of the micro gap using alkanethiol chemistry. The DNA probe Oligo A being complementary to a specific λ -DNA sticky end allowing DNA hybridisation to occur between the molecules. To further align and position the λ -DNA towards the opposing electrode hydrodynamic stretching was employed. This allowed the molecule to migrate perpendicular to the opposing electrode, allowing it to hybridise to the additional complementary ssDNA probe (Oligo B). This allowed a DNA nanowire to be spanned between the electrode micro gap as highlighted in Figure 1-13.

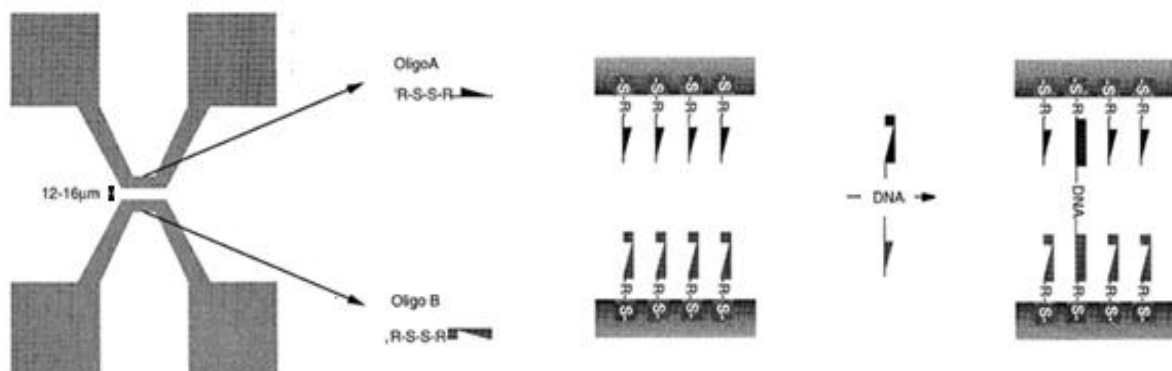


Figure 1-13: A schematic of how a DNA nanowire is formed between electrodes using thiolated ssDNA probes anchored to the gold. Adapted from (Braun, Eichen et al. 1998).

1.4.1 Stretching and alignment of DNA on a micromachined surface

Once the selective immobilisation of DNA has been achieved, alignment and stretching have to be applied to position the nanowire in the required location. This application of stretching and aligning DNA is regularly utilised to span the molecule on a substrate surface (Bensimon, Simon et al. 1994; Bensimon, Simon et al. 1995). As longer DNA molecules can be randomly coiled that are tricky to position in the orientation required. A variety of approaches have been employed to align and stretch DNA such as; hydrodynamic stretching, molecular combing and electrophoretic stretching.

1.4.2 Hydrodynamic Stretching of DNA

Hydrodynamic stretching allows the migration of DNA in the desired direction, using fluid flow of DNA anchored on a substrate. The substrate for example being a polystyrene bead (Perkins, Smith et al. 1995) or an microelectrode surface (Braun, Eichen et al. 1998). Figure 1-14 shows how DNA anchored to polystyrene bead held by optical tweezers can be stretched by fluid flow of the buffer solution. The DNA molecule is stretched by shear force of the fluid flow in the given direction by micropipetting. The DNA extension can depend on the rate of the fluid flow, viscosity of the liquid and original contour length.

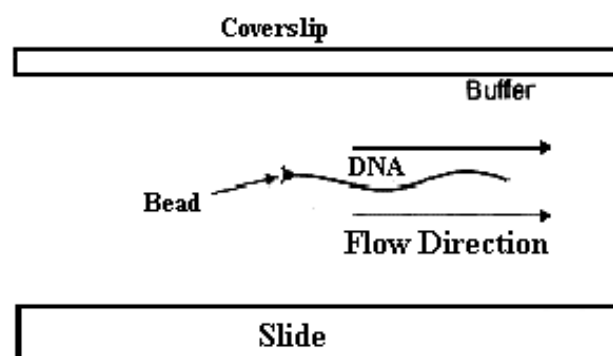


Figure 1-14: The hydrodynamic fluid flow stretching of DNA attached to a polystyrene bead.

Adapted from ref (Perkins, Quake et al. 1994).

Smith et al. managed to stretch λ -DNA to 170% of its original contour length using this method (Smith, Cui et al. 1996), though it was noted that overstretching may irreversibly alter the structure of the DNA molecule. Braun et al. (Braun, Eichen et al. 1998) took advantage of this technique to position λ -DNA between gold electrodes.

1.4.3 DNA Molecular Combing

Molecular combing is a technique that exploits a receding meniscus to stretch and migrate the DNA on a surface spontaneously (Bensimon, Simon et al. 1994). In this method DNA can be specifically or non-specifically deposited on a substrate surface. A glass coverslip is actuated along the surface to align DNA parallel to the motion using the air/water interface. A variety of surfaces have been investigated for combing efficiency; where the stretched DNA contour length can be dependent on the surface used. One study examined a variety of substrates for the ability of DNA to be combed effectively, where hydrophobic substrates were proposed to be the most effective to give longer DNA lengths (Bensimon, Simon et al. 1995). The degree of DNA extension of λ DNA has been shown to be combed to 26 μm on a polystyrene surface and 22 μm on a silanised surface (Allemand, Bensimon et al. 1997).

Bensimon et al (Allemand, Bensimon et al. 1997) found that pH affected the way that the DNA behaved when stretched. They found that lower pH extended DNA to longer contour lengths stating that pH 5.5 was the most suitable. Yokota et al fashioned a method to quickly straighten and align DNA using molecular combing by mechanical control of the meniscus to stretch DNA molecules (Yokota, Johnson et al. 1997). The real time observation of stretched molecules was undertaken in many studies using fluorescent microscopy and DNA specific fluorescent dyes.

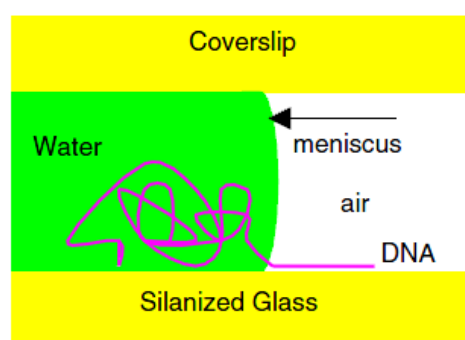


Figure 1-15: An illustration of molecular combing of DNA using a receding meniscus.

Adapted from (Allemand, Bensimon et al. 1997)

1.4.4 Direct Current electrophoretic stretching

Direct current (DC) electrophoretic stretching can be used to stretch and position DNA. Gel electrophoresis is based on the same principle, which is used to separate DNA fragments in

the gel matrix. The polyanionic DNA molecules migrate towards the anode due to their electrical charge with regards to the size. Unlike DEP, the molecule must be chemically anchored to the substrate to stretch the molecule in the DC field. The ability to align DNA using a DC field has been investigated, allowing anchored DNA molecules to become uncoiled like unwound springs in the presence of the DC field. In one study a solution of DNA was anchored to gold using biotin-streptavidin chemistry which by using a 5 V cm^{-1} DC electrical field the DNA molecules were stretched to their full length (Zimmermann and Cox 1994). This was termed “free electrophoresis”, where the stretched DNA was observed by fluorescent microscopy.

1.4.5 Dielectrophoretic Stretching of DNA

Dielectrophoresis (DEP) is a non-uniform electric field that can align di-polar objects in the electric field. The DNA molecule has a polyanionic backbone which is surrounded by counterions at equilibrium that makes it polarisable allowing it be positioned using DEP. Washizu et al used DEP to align λ -DNA between two opposing electrodes using a 1 MHz and $>1 \times 10^6 \text{ V m}^{-1}$ field (Washizu, Washizu et al. 1990; Washizu, Washizu et al. 1995). Cheng et al used floating potential electrodes (FPE) which showed to increase the number of highly aligned λ -DNA molecules as shown in Figure 1-16. The FPE’s were used to reduce thermal fluctuations that can cause turbulent flow allowing the anchored DNA to be stretched efficiently in the electrical field.

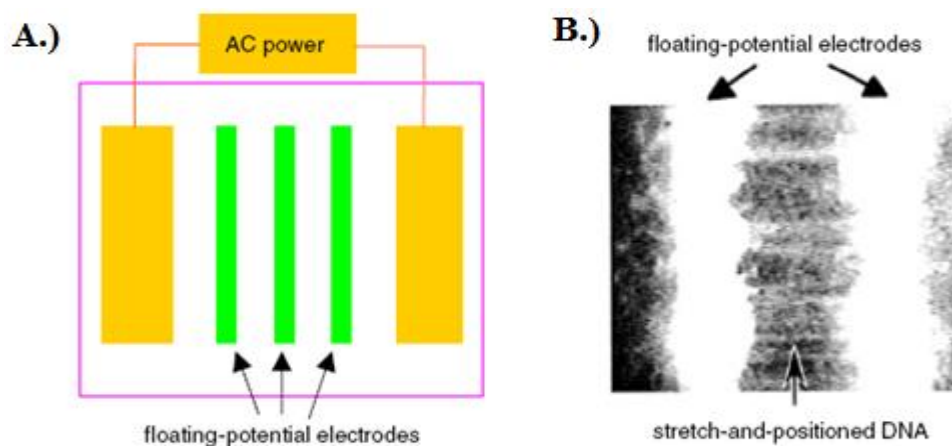


Figure 1-16: An illustration and image of floating potential electrodes. A.) shows a drawing of the FPE’s connected to the AC power. B.) shows λ -DNA molecules stretched and positioned between electrodes, the DNA was stained with YOYO-1 and observed in real time. Both pictures adapted from (Gu, Cheng et al. 2006).

DEP has been shown to elongate λ DNA in a polymer based polyacrylamide solution to 21 μm in a 1 MHz and $3 \times 10^5 \text{ V cm}^{-1}$ field between gold electrodes 40 μm apart (Namasivayam, Larson et al. 2002). A range of parameters have been reported in the literature for stretching DNA using DEP from low to higher frequencies (Washizu, Washizu et al. 1990; Washizu, Kurosawa et al. 1995; Washizu, Washizu et al. 1995; Rakitin, Aich et al. 2001). Germishuizen et al performed stretching of DNA immobilised on a gold surface using a 300–500 KHz AC field elongating λ -DNA to 15 μm , which is not the full molecular extension (Germishuizen, auml et al. 2003). The DEP method gives the ability to stretch and align DNA that may allow DNA to be integrated into future nanosized devices efficiently.

1.5 Electrical functionality and characterisation of DNA templates

The electrical characteristics of naked DNA has been reported to have a variety of properties from conducting, insulating (Storm, van Noort et al. 2001), ohmic and even superconducting. This caused investigations to be performed where DNA has been modified with a metal (metallisation) to enable electrical conductivity of the molecule. The electrical conducting properties of DNA of long lengths have been reported to be low. Arnold Storm and co-workers found that DNA of 40 nm in length positioned between two nanoelectrodes measured an infinite ($>10^{13}$ ohm) resistance (Storm, van Noort et al. 2001). Similarly, the λ phage DNA molecule has been noted for its electrical resistance and insulating properties (de Pablo, Moreno-Herrero et al. 2000), but the magnitude of resistance in λ -DNA molecules is not yet clearly understood. Many research groups have scrutinised the possibility of DNA metallisation to increase conductivity allowing an application in bioelectronics. The outcome of the different investigations of DNA electrical conductivity could be effected by various factors such as; the contacts between the electrodes and the DNA molecule, the DNA length, DNA sequence, DNA character (ropes or bundles), the environment of the DNA, microstructure of DNA (surface immobilisation protocol such as combing procedure), interfacial character (i.e. stretched on mica or suspended) and preparation protocols. These factors can be extremely hard to control giving rise to the variation in findings.

1.5.1 Modification, Metallisation and Electrical Conduction of DNA

A popular method for the metallisation of DNA is exploiting the polyanionic backbone to perform DNA templated assembly. This has been achieved using metals such as; gold (J. K. N. Mbindyo. 2001), silver (Braun, Eichen et al. 1998) (Keren, Krueger et al. 2002; Keren, Berman et al. 2004), palladium (Richter 2001) (Richter, Seidel et al. 2000; Richter, Mertig et al. 2001; Richter, Mertig et al. 2002) and polypyrrole (Dong, Hollis et al. 2007). A further metallisation method involves the imino proton substitution of the bases Thymine and Guanine with metal ions forming 'M-DNA'. The M-DNA method has been undertaken using Zinc (Aich, Labiuk et al. 1999; Rakitin, Aich et al. 2001; Wettig, Li et al. 2003) (Omerzu, Mihailovicacute et al. 2007), Nickel (Aich, Labiuk et al. 1999) and Cobalt (Aich, Labiuk et al. 1999) The metallisation can be accomplished before or after DNA has been aligned and positioned on a substrate. The choice of metallisation protocol may be dependent on the method employed to deposit the DNA on the substrate.

1.5.2 DNA Templated Polypyrrole DNA Nanowires

In a study by Dong et al, the synthesis of a polypyrrole (PPy) DNA nanowire was undertaken (Dong, Hollis et al. 2007). A DNA template was modified with pyrrole, a cationic heterocyclic aromatic organic compound. The oxidation of a pyrrole monomer with FeCl_3 yields a solution that contains polypyrrole, a polycationic charged polymer. The DNA template being polyanionic creates an association forming a PPy/DNA nanowire complex. To provide initial evidence for the formation of the two hybrid polymers, Fourier transform infrared spectroscopy (FTIR) was employed. The FTIR data confirmed that the DNA template was suitable for directing the growth of polypyrrole wires. The synthesis was performed in solution which was then deposited onto alkylated silicon (111) surface to analyse the DNA complex using Atomic Force microscopy (AFM). The resulting nanowire formed a smooth structure with consistent polypyrrole coverage throughout the DNA template. Interestingly when the DNA was polymerised by PPy immobilised on a silicon (111) surface, AFM studies showed that the PPy/DNA nanowire complex resembled a beads on a string structure as shown in Figure 1-17. The electrical properties of the resulting PPy/DNA nanowires showed conducting properties with a slight current plateau at around zero bias Voltage, suggesting a formation of Schottky barriers at the nanowire/electrode interfaces (Van and et al. 2000; Abthagir and Saraswathi 2001). The authors suggest that the wire shows similar conducting properties to bulk polypyrrole powder.

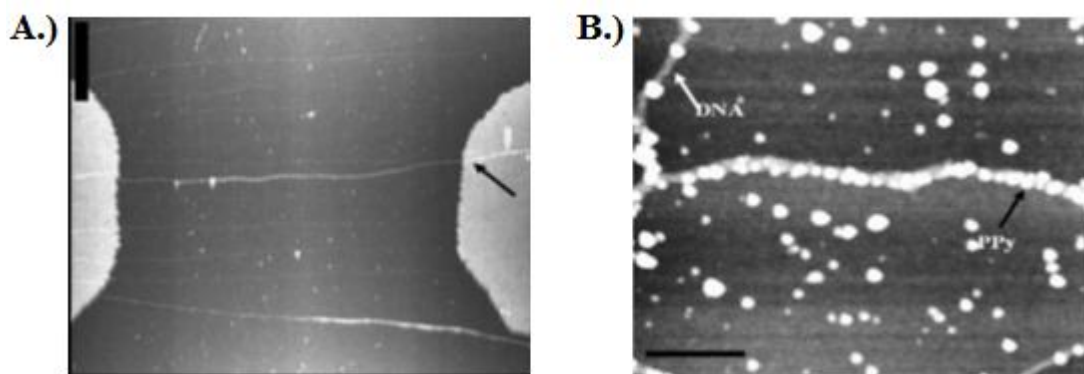


Figure 1-17: A.) An AFM image of the electrical measurement device to measure the electrical conductivity, the black arrow shows a PPY/DNA nanowire spanned across the electrode gap. B.) An AFM image of a PPY/DNA nanowire formed in-situ on the silicon surface showing the beads on a string structure.

1.5.3 DNA Templated Silver Nanowires

The most cited research on DNA templated assembly allowing metallic nanowire production was produced by Braun et al. (Braun, Eichen et al. 1998). They were the first group to covalently anchor a DNA nanowire between electrodes, allowing metallisation and allow electrical testing. The DNA template was further metallised using silver ions, forming a silver templated DNA. The DNA deposition process employed was highly selective to the DNA template, occurring specifically on the DNA molecule where not depositing nonspecifically on the surrounding substrate. The polyanionic character of the DNA template allowed silver ions to associate by an $\text{Ag}^+\text{-Na}^+$ ion exchange mechanism. The resulting DNA templated silver DNA nanowire was imaged using atomic force microscopy (AFM) that was shown to have a width of 100 nm compared to the natural width of 2 nm. Figure 1-18 shows the AFM image of the Silver DNA wire, the area of analysis being $1.5 \times 1.5 \mu\text{m}$.

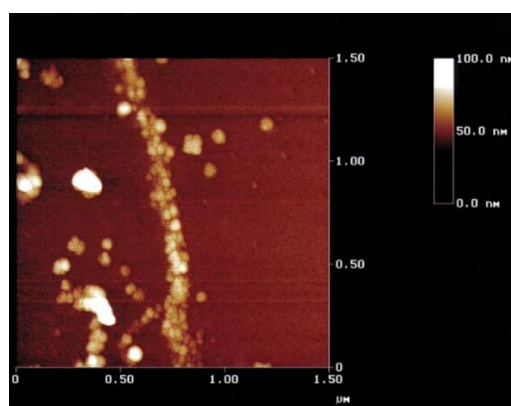


Figure 1-18: An AFM image ($1.5\mu\text{m}$) of silver characterised DNA between two gold electrodes. Picture taken from ref (Braun, Eichen et al. 1998)

The electrical property of the silver modified DNA wire was investigated after the metallisation process. The wire showed a zero current plateau approaching zero voltage from negative or positive bias that developed with differential resistance larger than the internal resistance. The wire became conductive again at higher bias with a differential resistance lower than the original bias polarity. It is unclear why this occurs, the article suggests that it may happen for two reasons. The first being the coulomb blockade phenomenon where the grain size can affect the electrical charging energy, the second being that corrosion of the Silver ions may be happening forming an electrical barrier. As a control element, naked non metallised DNA was tested for its electrical properties that suggested it to be an electrical insulator. As a further step a positioned DNA wire was extensively treated with silver ions that allowed the current plateau to be eliminated giving Ohmic behaviour. The silver deposition process was performed between the electrodes where no DNA was present, no current was observed with varying bias, as shown in Figure 1-19.

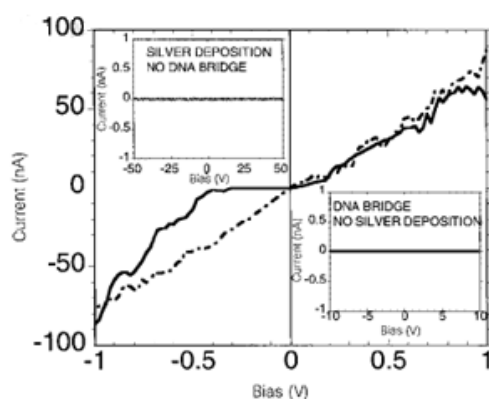


Figure 1-19: An I-V curve for a silver coated DNA bridge. Inset left being for silver deposition alone and inset right for a non-modified DNA bridge. Adapted from ref (Braun, Eichen et al. 1998).

1.5.4 Metallisation through imino substitution reactions

M-DNA is the engineering of DNA by a substitution reaction of the imino proton of base pairs with a metal ion. This allows the metal ion to be inserted every 4 Ångstroms regardless of DNA sequence. The DNA template has been metallised using cationic metal ions to form M-DNA to investigate the electrical properties. Metal ions such as; zinc (Aich, Labiuk et al. 1999; Rakitin, Aich et al. 2001; Wettig, Li et al. 2003) (Omerzu, Mihailovicacute et al. 2007), Nickel (Aich, Labiuk et al. 1999) and cobalt (Aich, Labiuk et al. 1999) have been studied with the effect of intercalating into the DNA template using spectrophotometric and structural analysis techniques such as nuclear magnetic resonance (NMR). The ability to form M-DNA

has been shown to be pH dependent in the literature suggesting that a high pH range to be the optimum condition for metallisation (Aich, Labiuk et al. 1999; Wettig, Wood et al. 2003). The use of lower pH, below 7 does not allow M-DNA to be formed. The mechanism of metal ion binding has been stated to be the replacement of the imino proton of the base pairs of DNA (Rakitin, Aich et al. 2001) where the NMR studies have suggested that the imino protons in M-DNA were not present at pKa 9.9 and 9.4 of T and G respectively. This leads to a more sophisticated protocol for metallising DNA as fully doping and covering the DNA template can lead to vast thickness increase. If the desired structural properties of a metallised DNA molecule are to be kept nearest to the native form, then intercalation of metal ions will give the desired structure. The image in Figure 1-20 shows the proposed structure of intercalation of the Zn^{2+} ions by replacing the imino protons of the pyrimidine bases.

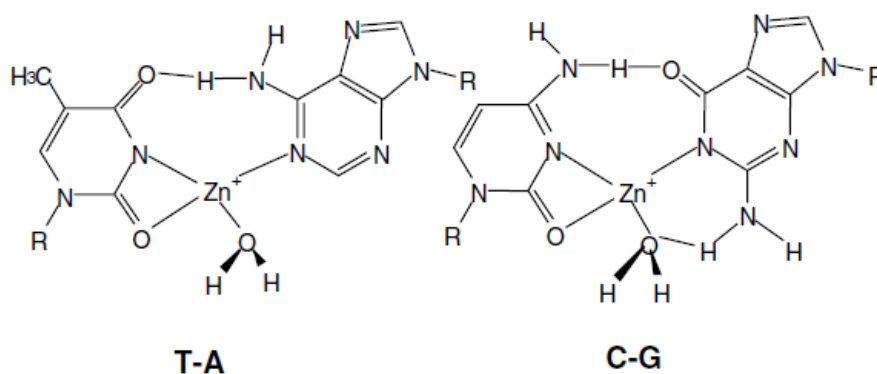


Figure 1-20: The proposed scheme for zinc modified DNA. The imino proton of the N3 position of thymine and the N1 position of guanine are replaced by the Zn^{2+} ions. Picture taken from ref (Rakitin, Aich et al. 2001).

As discussed there is a wide range of literature discussing many protocols to immobilise, position and make the DNA molecule a conductive material. Through exploiting these techniques a novel bio-microaccelerometer design has been proposed to where the DNA molecule is used as a tunneling strain gauge. This is desirable as it could produce a class of accelerometer that will cover the whole dynamic range of sensitivity, unlike the current state of the art.

2 Chapter 2 The design, modelling and fabrication assessment of a MEMS

Accelerometer

2.1 Introduction

This chapter discusses the design rationale, structural specifications, finite element analysis (FEA) and performance modelling of a novel accelerometer to undergo biological functionalisation. The aim being to investigate the construction of a hybrid biological/mechanical inertial sensing device. The ultimate goal being to construct a highly sensitive biological accelerometer device with a large dynamic range that can be integrated into an inertial navigation system. Three varying types of accelerometer device which were subtly structurally different (known as ‘types’ herein) were designed and fabricated using microfabrication technology. The devices were firstly designed using L-edit layout editing software and modelled using ANSYS FEA to determine the natural resonant frequency and static deflection performance prior to fabrication. The use of microfabrication allowed the fabrication of the three types of accelerometers giving the desired structural dimensions from Silicon on Insulator (SOI) wafer. The chapter starts by discussing the principle of the biological accelerometer device for the use with INS technology.

2.2 The principle of the novel biological accelerometer design

The principle aim of the research features the design and fabrication of a novel biological MEMs accelerometer. The novel element being an accelerometer that consists of a metallised DNA molecule acting as the sensing element, to investigate the possibility of measure accurate acceleration in the sensing axis.

2.2.1 The possible advantage over current accelerometer designs

The natural width of a DNA molecule is approximately 2 nm (Lyubchenko and Shlyakhtenko 1997) and the length determined by the genome used, has been reported to be stretched to 1.7 times of the original contour length (Bensimon, Simon et al. 1994). The DNA molecule has structural similarities to a helical spring with relation to the elasticity of the contour length that is described by the ‘worm like chain model’ (Vologodskii 1994; Marko and Siggia 1995; Bouchiat, Wang et al. 1999; Bustamante, Smith et al. 2000).

The image in Figure 2-1 displays the principle components of a biological accelerometer that illustrates a DNA strain gauge covalently attached to the inertial (proof) mass and opposing constraint (known as ‘the sensing gap’ herein), allowing elongation/stretching of the molecule with applied acceleration. The degree of stretching of a metallised DNA in this configuration could allow acceleration to be determined by monitoring the change of the electrical properties. The mechanical properties of DNA theoretically may allow low and high gee accelerations to be measured. This being due to the electrical properties changing significantly with a small degree of DNA stretching, though this is dependent on the degree of metallisation.

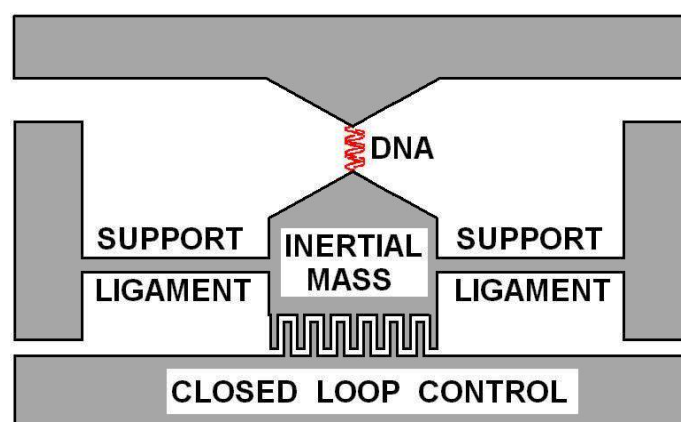


Figure 2-1: An illustration showing a general accelerometer incorporating a DNA molecule as the sensing element.

There were two options to investigate for the metallisation of the DNA to allow sensing in this configuration;

- The DNA molecule could be entirely coated in a metal to give a conformal metallic layer on the template, though the nanowire will be rigid and will only allow a strain sensor with a gauge factor of 2 to be produced.
- DNA could be metallised to change the electrical properties and give the ability to retain the spring like properties of the molecule, thus forming M-DNA. Through the application of an electrical potential across the M-DNA template, a tunneling current could be formed in this configuration that may allow a measurable change of current for small displacements. In the literature the DNA molecule has been reported to have been stretched over twice its contour length (Bouchiat, Wang et al. 1999) equating to a potential current change of 5 orders of magnitude for this application. The gauge factor of the DNA molecule can potentially be as high as 100,000 in this configuration.

In the accelerometer configuration where DNA is spanned across the sensing gap under compression it will fold unpredictably, therefore it was envisaged for the molecule to be stretched to 50 % of the contour length to a 'start position'. This typically allows the measurement of positive and negative accelerations; if a longer length of DNA is used it will give a larger absolute value and remove the problem of crashing that is common for tunneling accelerometers.

The degree of chemical metallisation of the DNA molecule was a key factor for this research to discover the optimum protocols effectively perform metallisation whilst retaining the spring like properties. Future work would involve the investigation of the conductivity/resistivity change per unit strain, where the accelerometer was intended to be within the 100 g range with a noise floor of $1 \mu\text{g}/\sqrt{\text{Hz}}$. The whole aim being to develop an accelerometer with an increased dynamic range to what is commercially available at the present time. For the biological accelerometer to be constructed to have an increased dynamic range with a higher sensitivity than what is commercially available, the following aims were undertaken.

2.2.2 Aims and requirements

To construct the biological MEMs accelerometer discussed in this research the following were required;

- The design of microaccelerometers that can actuate in the sensing axis effectively.
- The fabrication of the silicon MEMs accelerometer to be suitable for closed loop control (3 x Types).
- The electrical actuation of accelerometer comb drives to measure the degree of static deflection using as an optical deflection measurement system such as a Zygo profiler interferometer.
- The measurement of the natural resonant frequencies of the accelerometer using a non-contact resonance frequency measurement system, such as a Laser Doppler Vibrometer (LDV).
- The metallisation of DNA to potentially enhance the electrical properties which was monitored using spectrophotometric and fluorometric analysis.
- The placement of fluorescently labelled DNA in the sensing gap of an accelerometer observed using an epi-fluorescent microscope.

2.3 General Outline of Accelerometer design

The silicon MEMS accelerometers were designed specifically for the placement and stretching of DNA; three types were designed and fabricated. Each type was designed with subtle differences to certain structural features (see Table 2-1) such as the comb drive finger spacing and the support spring width, the features are highlighted in Figure 2-2. This was performed for the ease of fabrication to ensure that an accelerometer type was successfully made without any structural defects. The natural resonant frequency and degree of static deflection of the proof mass by electrostatic actuation were investigated prior to fabrication by ANSYS modelling. The features also playing a role in the performance of the accelerometer which are explained below;

1. A sensing gap to place the DNA strain gauge (gold sensing tips to allow biofunctionalisation with alkanethiol chemistry).
2. An inertial proof mass.
3. A calibration tip to allow a measurement of static deflection and natural frequency.
4. Gold bond pads to allow electrical connections to be made to dual inline packaging.
5. A type design indicator to allow easy identification.
6. Comb drive actuators for electrostatic actuation and static deflection (variable)
7. Support springs (variable)

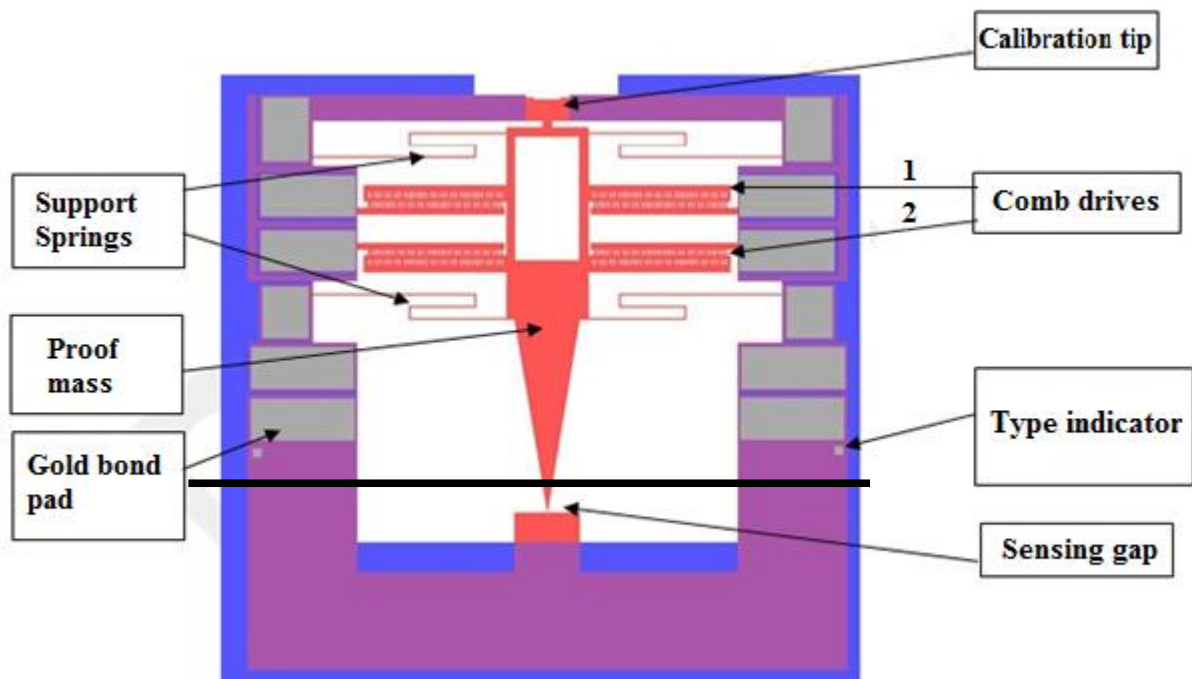


Figure 2-2: The key components of the accelerometer design, the black line shows the level that the device is designed to be dipped.

The structural features of a single accelerometer consists of 12 gold contact bond pads, 4 comb drive actuators (2 for each actuation direction), a proof mass, a sensing gap and a calibration tip. A device type indicator (gold) was used to allow an easy determination of the types, as the differences between the designs are subtle and can be difficult to identify easily. The device was further designed specifically to allow dipping in liquid media without causing malfunction. The gold contact bond pads and actuating structural components were designed to be a suitable distance from the sensing gap. The gap was designed to be submerged in a deposition solution for the DNA immobilisation protocols, therefore protecting the actuating structures to allow device operation during and after dipping. The black line in Figure 2-2 shows the level to which the accelerometer die was to be dipped in the deposition solution. The individual features of the accelerometer design and the rationale for the specific dimensions is discussed further in section 2.4.

A single designed die contained 4 accelerometer devices of the same type which was common for all types. The image in Figure 2-2 also depicts the overlaid masks used in the fabrication process; depicting the handle layer gold layer and device layer. The handle layer that is shown in blue was simply designed to allow mechanical support for the floating device layer. The gold layer was to allow the formation of electrical contacts to specific features of the accelerometer and to produce the gold sensing tips for DNA immobilisation. The device layer shown in red illustrates the suspended proof mass and comb drive actuators that are constrained by the support spring attached to the handle layer. The electrostatic actuation of the accelerometer comb drives will cause a deflection of the proof mass along the sensing axis. The direction of deflection will depend on which comb drive pair has been actuated. Comb drive pair 1 was designed to deflect the proof mass so that the sensing gap distance decreases whereas the actuation of comb drive 2 increases the distance.

2.4 Structural specifications of accelerometer devices

The designs were produced using ‘Tanner L-edit’ layout editing software prior to fabrication so that they could further be used to produce photolithographic masks. The mask drawings are shown in this chapter to explain the structural feature dimensions that were desired.

2.4.1 Variation in accelerometer type design

The variation of the accelerometer type feature size for the comb drives and spring width are listed below in Table 2-1.

Design constraints	Spring Width (μm)	Fingers per comb pair	Finger Gap (μm)	Finger Length (μm)	Overlapping finger length (μm)	Finger Width (μm)
Device type 1	5	56	2.5	60	20	5
Device type 2	12	56	2.5	60	20	5
Device type 3	12	28	10	60	20	5

Table 2-1: A list of the variation in the dimensions of the types of accelerometer.

The accelerometer types 1-2 were designed and fabricated with equal comb drive dimensions but a differing spring width where types 2-3 had the same spring width but with contrasting comb drive feature sizes. The rationale for the three types of accelerometer with regards to structural specifications is discussed further in the next section.

2.4.1.1 Sensing gap

The image in Figure 2-3 shows in detail the sensing gap indicated previously in Figure 2-2, which is the region of positioning and stretching of the DNA molecule. The sensing gap was designed with two opposing tips that were deposited with gold to allow the use of alkanethiol chemistry to allow the immobilisation and positioning of DNA spanned across the gap. The distance between the gold sensing tips was designed specifically to be $10\ \mu\text{m}$ ($\pm 2\ \mu\text{m}$). This was performed to allow the positioning of λ -DNA with a specific length of $16.2\ \mu\text{m}$ in the gap. The long length DNA was chosen to ease fabrication tolerances that allowed it to be performed using standard lithography and chemical etching techniques, as opposed to employing technologies such as e-beam lithography to make nanosized features for small length DNA which would be time consuming with a higher cost. The sensing gap dimension was extremely critical between all types to allow the biofunctionalisation with the DNA molecule.

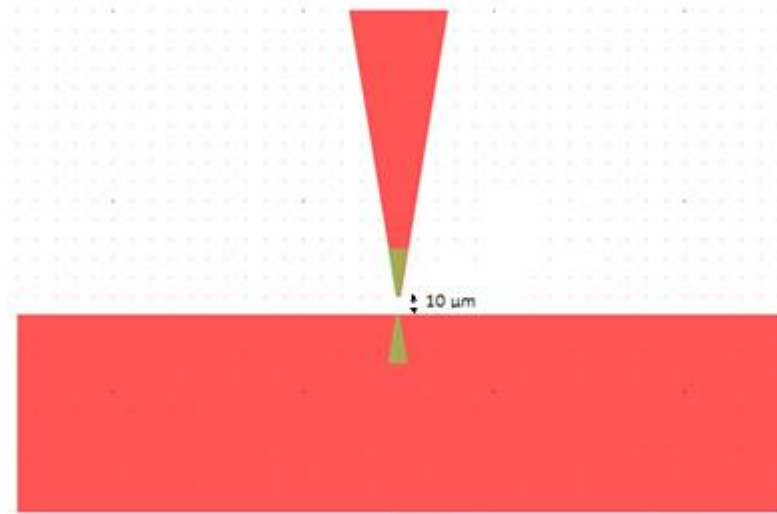


Figure 2-3: A higher detailed image of the mask design showing the 10 μm gap between the gold sensing tips

2.4.1.2 Calibration tip

As previously illustrated in Figure 2-2 the accelerometer designs of all types contain a structural feature named the ‘calibration tip’ that has a constant size. The calibration tip was designed to permit access to the proof mass, allowing a cross sectional plane measurement for the static deflection and resonant frequency measurements in real time. The deflection of the proof mass will move the central calibration tip proportionally as shown in Figure 2-4 to the magnitude and direction of the deflection. The degree of static deflection can be measured by comparing the calibration tip to the zero position that was determined by the static reference planes.

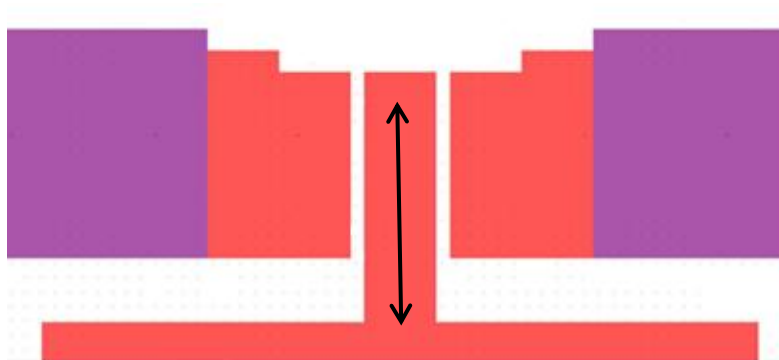


Figure 2-4: The mask drawing of the calibration tip that is typical of all types which shows the possible direction of deflection indicated by the arrow. The non-actuating planes are the static reference planes which can be compared with the calibration tip to determine the amount of static deflection.

The calibration tip was monitored during the static deflection measurements to give an indication of the operational characteristics of the three types of accelerometer due to the variable structural features that were employed.

2.4.2 The structural features specific to Accelerometer type

The following section discusses the subtle differences of the comb drive actuator and spring features between the accelerometer types. The variation of the features was undertaken to investigate the accelerometer structures that could be produced using the fabrication process discussed in this thesis. Initially the comb drive features were kept small (types 1-2) so that a low driving voltage could generate a suitable electrostatic force to perform effective static deflection. If the small features were not realised in the fabrication process, the accelerometer with larger comb features (type 3) could be employed.

2.4.2.1 The Comb Drive pairs

The electrostatic comb drive actuator is commonly employed because of its force/electrical power ratio (Legtenberg R and M 1995). An illustration of the principles of electrostatic actuation of a comb drive is shown in Figure 2-5, depicting that one side of the comb drive is fixed (the stator) and the other becomes deflected (rotor), where the rotor generally consists of an additional finger to the stator to reduce deflection in the 'X' axis. A DC electrical voltage applied to the comb causes the rotor to be displaced towards the stator shown as in the 'Y' axis. The amount of displacement is dependent by the electrostatic force generated by the comb and the spring constant which is determined by the spring structural dimensions. The actuation of the comb drives for the accelerometers in this research causes deflection of the proof mass and calibration tip which was measured using optical interferometry and laser Doppler vibrometry.

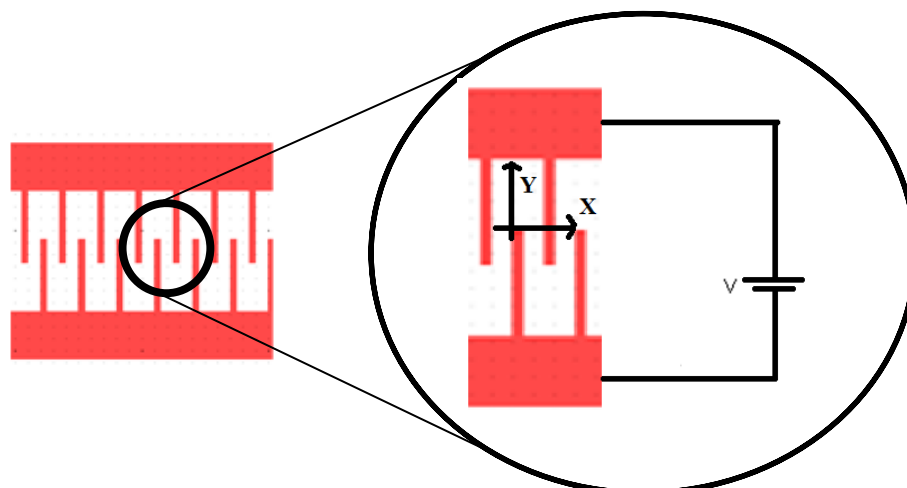


Figure 2-5: The components of a comb drive to produce electrostatic actuation.

The accelerometer types were fabricated to contain 2 comb drive pairs to actuate the proof mass in either direction for closed loop control and to stretch the DNA molecule as required. The variation of the overlapping finger distances of the comb drives between the types are highlighted in Table 2-1 on page 35. The overlapping finger distance of a type 1+2 accelerometer was designed to be 2.5 μm (see Figure 2-6) and type 3 to be 10 μm . The type 3 having a higher success of being fabricated to specification due to having a more relaxed tolerance than type 1+2.

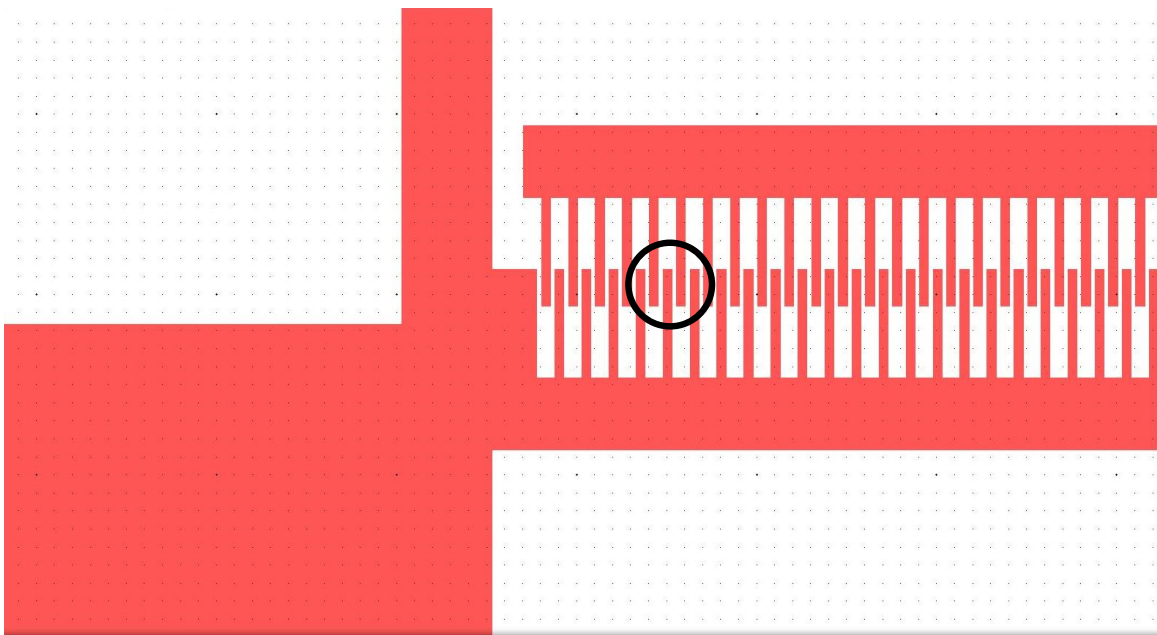


Figure 2-6: The comb drive feature size of the type 1+2 accelerometer, the circle indicating the overlapping finger region.

The electrical actuation of the combs was sourced from a DC voltage power supply, where an increase in voltage was envisaged to cause an increase in deflection in the given direction. The electrostatic force generated is determined by many factors such as the overlapping finger distance, the width and length of the fingers and the number of fingers on one comb. These parameters determine the electrostatic force that will be generated to deflect the proof mass in the actuation plane.

2.4.2.2 Spring flexures

The support springs were specifically designed to constrain the floating proof mass to the handle layer to allow a spring restoring force. The spring geometry of the accelerometer types in this research were designed to have a serpentine flexure as shown Figure 2-7. This geometry was employed to reduce the space needed for the spring and to theoretically decrease the problem of lateral displacement that can be a common for comb actuators.

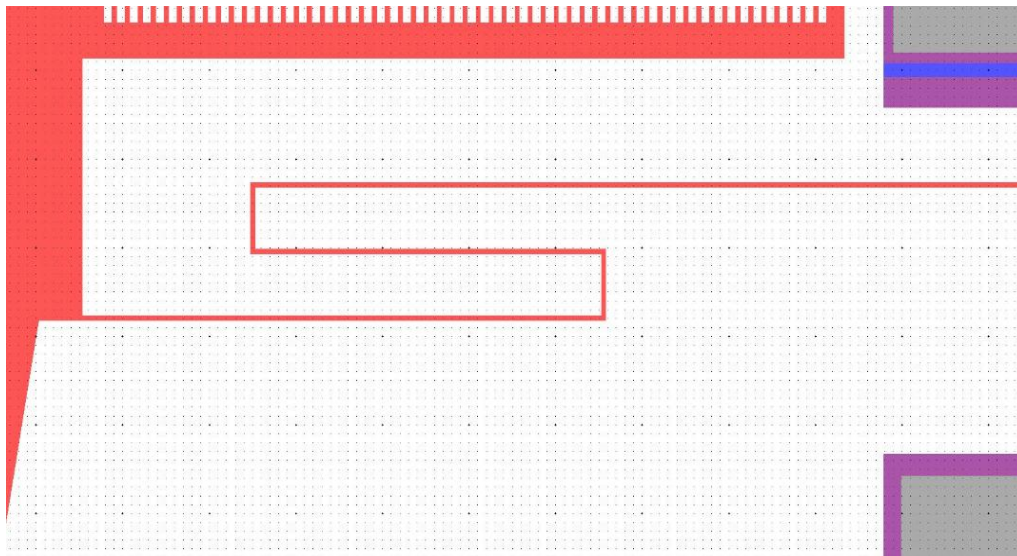


Figure 2-7: An illustration of a 5 μm wide spring of the type 1 accelerometer.

The variation of the spring width feature size between type 1 and type 2+3 accelerometers were designed with varying thickness to increase the chance of a successful of fabrication. The spring thickness also determining the spring restoring force value; theoretically type 2+3 should have a higher value than type 1. Therefore the degree of deflection was initially predicted to be smaller with electrostatic actuation; this is further discussed in section 2.6.

2.4.2.3 Further design considerations

The following points below were considered when designing the accelerometer for all types;

1. To modify the accelerometer packaging to be open at one end to allow access for cross sectional observation of the calibration tip with the measurement apparatus
2. To allow the ease of dipping of the sensing gap into a biological medium for the DNA immobilisation protocols to be undertaken. This was to be achieved without immersing the gold bond pads and structural device layer. This was critical as the bio-

immobilisation protocol is specific to gold substrates and also to stop the possibility of irreversible stiction of the comb drives in an aqueous medium occurring.

3. To allow an ease of gold bond pad access with a suitable geometry to allow wirebonding to dual inline packaging (DIP).
4. To be of a die size that allows ease of handling for testing and biofunctionalisation protocols.
5. To be suitably designed as to reduce the amount of torsional deflection during harmonic excitation. The accelerometer consisted of two pairs of springs with varying widths to allow the structure to resonate with a low frequency in the actuation plane where at a high frequency torsionally.

2.5 ANSYS Finite element analysis

First, a finite element analysis was performed prior to fabrication to investigate the predicted mode shapes of the accelerometer types. ANSYS finite element analysis (FEA) software is commonly used prior to the fabrication of a microstructure to give theoretical information on the performance (Houlihan and Kraft 2005; Hyeon Cheol, Seonho et al. 2005; Lee, Yoon et al. 2005; Sun, Wu et al. 2009). This allows an estimation of the deformation and displacements of the structure during transient motion. The FEA method allowed the mode shapes of the accelerometer to be determined theoretically to envisage how it will operate in-plane and out-of plane for the DNA strain gauge sensing application. A continuous structure will have unlimited degrees of freedom (DOF), the finite element modal analysis using ANSYS allows an approximate structure to be calculated giving a finite number of DOF. For the purpose of this research, FEA was employed to perform a modal analysis to indicate the natural resonant frequency of the structure and the predicted mode shapes.

2.5.1 Accelerometer FEA modal analysis

The natural frequency of the accelerometer types was designed to be greater than 0.8 KHz to reduce the problems associated with background mechanical noise. The ANSYS FEA modal analysis software was employed to determine the theoretical natural frequencies and mode shapes of the structures. The geometry of the structure was inputted into the FEA script to simulate the fabricated accelerometer. The comb drive features were not inputted exactly, the equivalent mass was used for the simulation as shown in Figure 2-8 to reduce problem size. The springs were constrained at the ends to allow a true representation of the floating proof mass structure by using load constraints, highlighted by the blue crosses.

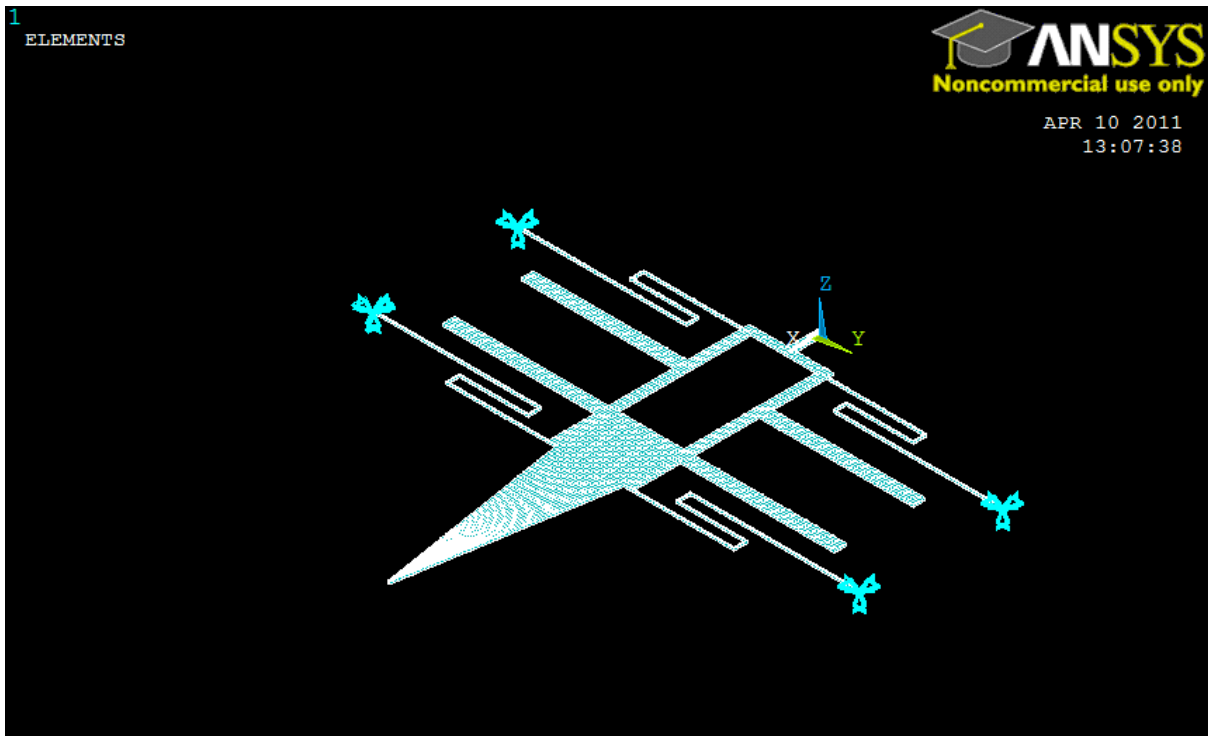


Figure 2-8: The ANSYS finite element graphical user interface highlighting the accelerometer device geometry and constraints.

2.5.1.1 Mode shapes of accelerometer types

Although there were three types of accelerometer only two modal analyses were undertaken, as the spring width is the only varying feature between taken into account. Hence the analyses did not include the electrostatic force generated by the combs which is discussed further in 2.6. The Type 1 accelerometer being ‘Analysis 1’ with the 5 μm spring width and type 2+3 being ‘Analysis 2’ with the 12 μm spring width. The analyses were performed with a 10 μm mesh size and set to formulate the first 10 mode shapes.

The ANSYS FEA undertaken for the type 1 accelerometer with the mode shapes and structural deformations determined are discussed in this section. The first 3 mode shape snapshots are shown in this section and Table 2-2 highlights the first 5 calculated mode frequencies.

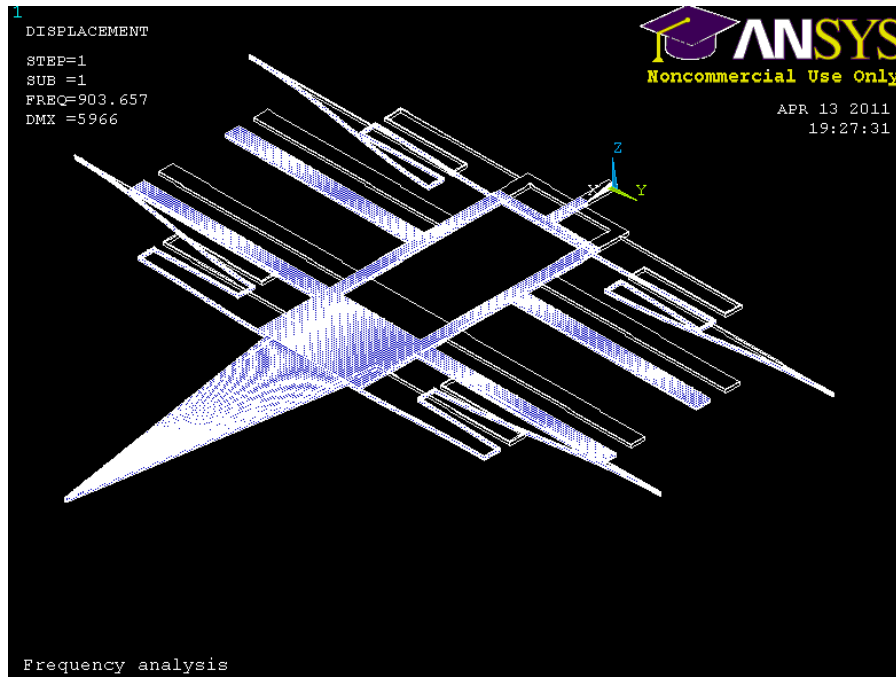


Figure 2-9: A snap shot of Analysis 1, mode shape 1 generated by ANSYS finite element analysis.

The first mode generated for analysis 1 shows the accelerometer structure undergoing in-plane displacement that is depicted in Figure 2-9. The mode shape shows the in-plane displacement along the sensing axis (x axis in the image) and having a natural resonant frequency of 0.9 KHz.

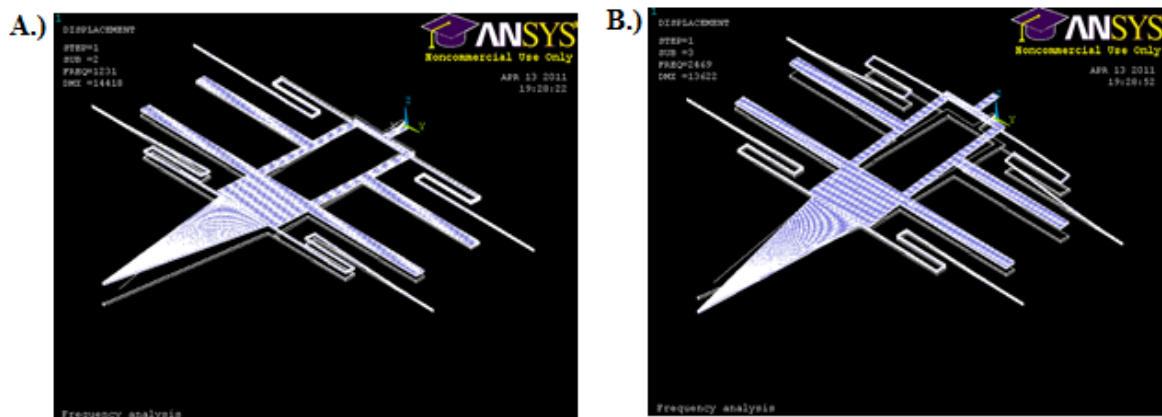


Figure 2-10: Analysis 1 generated from the FEA. A.) mode shape 2 B.) modeshape 3 generated by the ANSYS FEA.

The mode shapes in Figure 2-10 illustrate out-of-plane deflection from the sensing axis at 1.2 KHz and 2.4 KHz respectively. These mode shapes could theoretically increase the sensing gap distance in a non-linear fashion in the out-of-plane direction. The first 5 mode shapes that were generated for both analyses are listed in Table 2-2 below.

Mode	<u>Analysis 1:</u>	<u>Mode Plane</u>	<u>Analysis 2:</u>	<u>Mode Plane</u>
	<u>Frequency</u> <u>(KHz)</u>		<u>Frequency</u> <u>(KHz)</u>	
1	0.9	In-plane	2.0	Out-of-plane
2	1.2	Out-of-plane	2.5	In-plane
3	2.4	Out-of-plane	3.8	Out-of-plane
4	2.8	Out-of-plane	4.8	Out-of-plane
5	3.0	Out-of-plane	7.9	Out-of-plane

Table 2-2: The mode shape frequencies for Analysis 1 and 2.

It is preferred that the in-plane resonant frequency is lower for than that of out-of-plane torsional resonance. To reduce the out-of-plane resonance a thicker spring and proof mass would be beneficial, though the fabrication was limited to 15 μm . The limit was imposed on a fabrication run undertaken with many research partners; hence a common thickness had to be determined for the entire dies on the wafer.

2.6 ANSYS Static deflection analysis

To determine the performance of static deflection of the accelerometer types prior to fabrication ANSYS static analysis was undertaken. The geometries for the simulations were the same as in the FEA analysis. The electrostatic force generated by the combs for each type was calculated using equation 2-1 and inputted in to the analysis to determine the amount of deflection at a given voltage.

$$F = 1/2 \frac{nt \epsilon_0 \epsilon_r V^2}{d}$$

[2-1]

where F is the electrostatic force, n is the number of pairs of fingers, ϵ_0 is the permittivity of free space, ϵ_r is the relative permittivity of free space, V is the voltage applied and d is the overlapping finger distance. As illustrated in Figure 2-11, the direction of force in the x axis is balanced by the adjacent fingers giving actuation of the proof mass in the y axis. The electrostatic force was calculated with increments of the voltage applied for all three accelerometer types and the deflection theoretically determined.

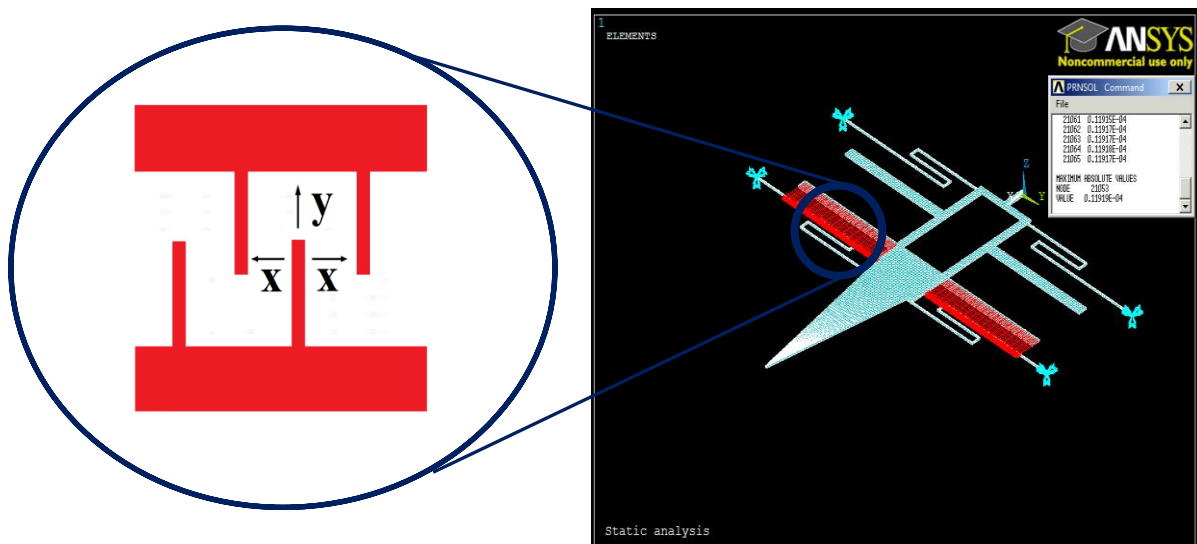


Figure 2-11: The directions of force for a comb drive actuator undergoing electrostatic actuation, shown in parallel with the ANSYS static deflection modelling of a type 1 accelerometer. The electrostatic force that is generated by the comb causes actuation which is highlighted with red on the simulation animation. The top inset window showing the value of deflection ($11.9 \mu\text{m}$) at 50 V ($2,500 \text{ V}^2$).

2.6.1 Modelled Results

The chart in Figure 2-12 displays the outcome for the static deflection modelling that was performed. A linear trendline was applied to the data series of each type as displayed in the chart; this allowed the gradient to be calculated which allows the value of deflection gradient per V^2 applied ($\mu\text{m}/V^2$) to be obtained. As can be seen the type 1 showed the best overall performance with a deflection gradient of $4.8 \text{ E-}03 \mu\text{m}/V^2$ which was ideally required for the operation with λ -DNA as the strain gauge. The type 2+3 showed a deflection gradient of $4.0\text{E-}04 \mu\text{m}/V^2$ and $5.0\text{E-}05 \mu\text{m}/V^2$ respectively. Therefore a large voltage would be needed to deflect the proof mass $10 \mu\text{m}$.

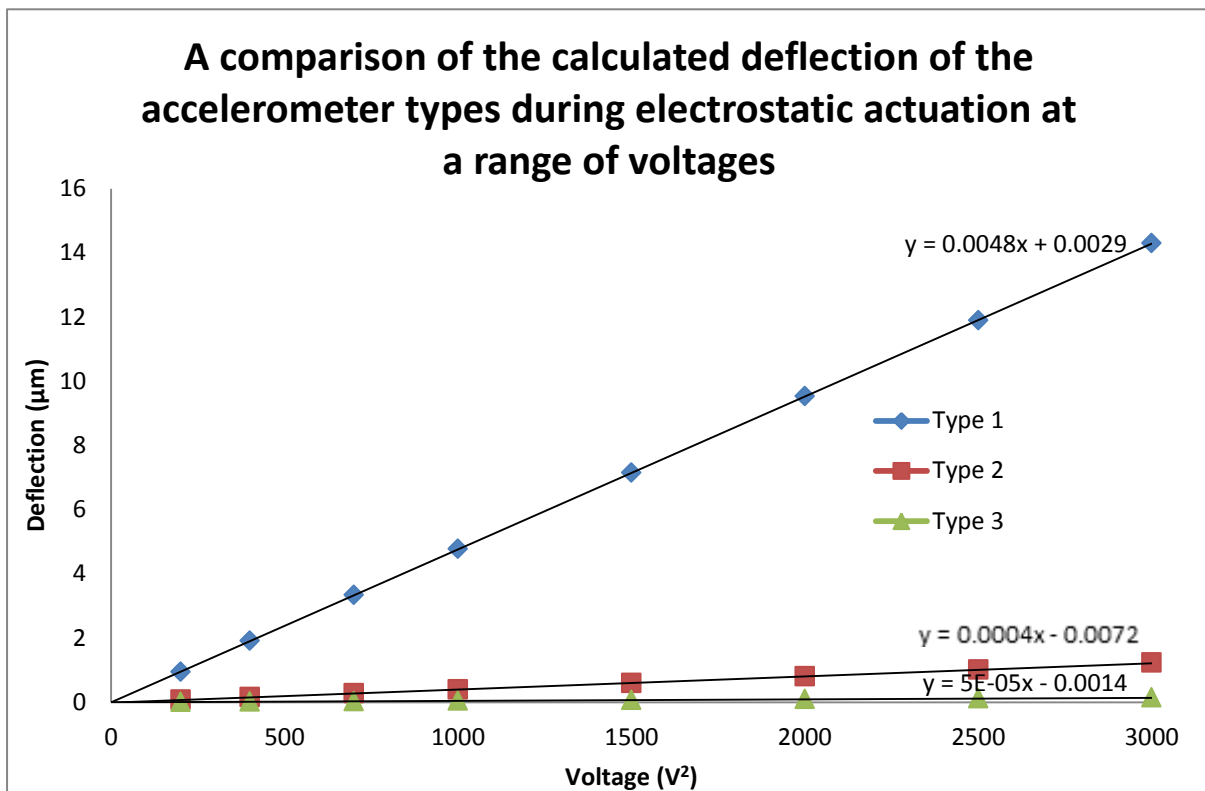


Figure 2-12: A comparison of the static deflection values of the accelerometer types with the voltage applied. A linear trendline was applied to all data series to calculate the gradient of deflection with V^2 .

The value obtained from the modelling are compared with the empirical results obtained in chapter 3.

2.7 Microfabrication Processing Technology

Most commonly microfabrication is used for the fabrication of micrometre size features for semiconductor technology and computer processor production. The fabrication of a micromachined device involves several processing steps that are required to give the final product. The microfabrication processes such as lithographic patterning, etching and metal deposition being the common steps performed, that can be repeated several times until the exact structures are produced from a silicon substrate. This section will firstly give a basic introduction to microfabrication technology and discuss the process flow for the fabrication of the accelerometer devices.

2.7.1 Lithography

Lithography is a common techniques used to pattern silicon wafers usually using photolithography (UV light) or e-beam lithography to pattern the desired structure onto a deposited photoresist layer on the substrate. The deposition of photoresist is commonly used to protect the substrate from a deposition/etch step that may be employed. In standard photolithography, a photolithographic mask is designed with the initial 2 dimensional surface pattern that is required and through the use of a UV light source the underlying surface is patterned characteristic to the mask. The photoresist layer either being hardened (positive resist) or softened (negative resist) depending on microfabrication process flow and instrument used. Hence the photoresist layer on the substrate is patterned and subsequently chemically removed leaving the hardened layer that is used to protect the substrate in subsequent etching steps that involves removing features that are not protected by photoresist. Alternatively the patterned photoresist layer can be used as a lift off layer to pattern metals such as chrome or gold in specified locations on a substrate surface, where after a deposition step the protecting photoresist is fully removed giving a specifically patterned metal layer on the substrate. The use of multiple masks is commonly used in a single fabrication to develop the required micromachined structure with specifically placed metal layers for electrical contacts.

2.7.2 Metal Etching

Etching is used for making features on a substrate, commonly for materials such as silicon in microfabrication by removing layers specifically. The type of etching employed is dependent on the property of the substrate to be removed and the depth of the etching to be undertaken. As used in this research and illustrated in Figure 2-13 a photoresist layer can be used to

pattern the surface to fabricate a micromachined device. Once the patterning is complete, the photoresist layer can later be removed by a wet chemical etching processes giving the desired structure. There are many types of etching techniques such as wet chemistry using strong acid (Williams and Muller 1996; Kovacs, Maluf et al. 1998) or alkaline (Elwenspoek 1996) solutions and dry techniques such as plasma etching (Standaert, Schaepekens et al. 1998; Fredriksson, Chakarov et al. 2009). The type of etching used to fabricate the accelerometer devices in this study being deep reactive ion etching.

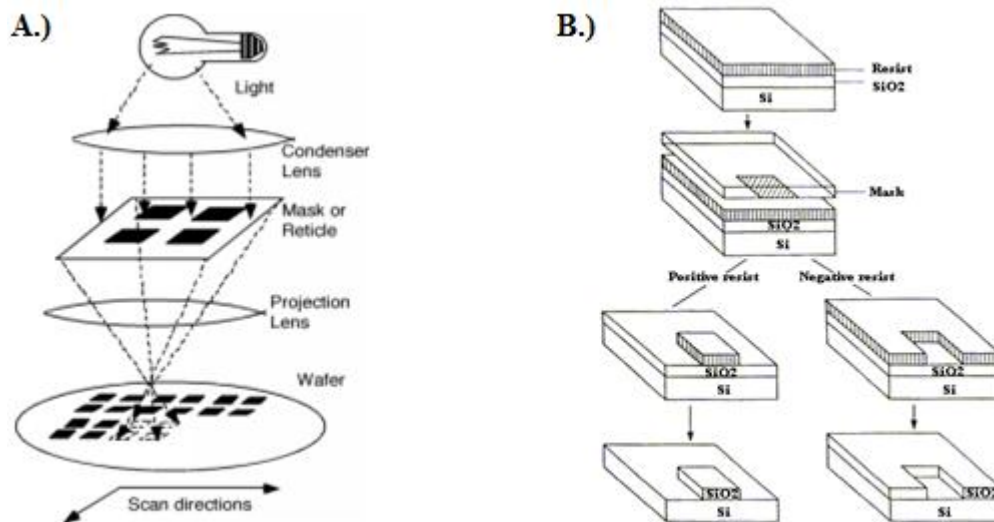


Figure 2-13: A.) Illustrates how the silicon surface can be patterned using a photolithographic mask using silicon wafer processing. B.) Shows how chemical etchants give the desired structure after photolithography.

2.7.2.1 Deep reactive ion etching

Reactive ion etching (RIE) is used in microscale fabrication to allow etching of large microscale vertical walls of 90°, but the walls can often be 88° and 92°. Reactive ion etching is a technique commonly being performed to fabricate integrated circuits, though it can only etch to short depths around approx. 10 μm. The use of deep reactive ion etching (DRIE) allows deeper vertical walls to be formed to a scale of 600 μm at faster rates (20 μm/min) than reactive ion etching. There are currently two popular types of DRIE, the patented ‘Bosch’ process (Laermer and Urban 2003) and the ‘Cryogenic’ process (Marty, Rousseau et al. 2005).

This research involved using the Bosch process which is a two-step process to give nearly vertical 90° walls. Firstly, the silicon wafer is bombarded from a vertical direction by plasma ions. In the case of silicon, a gas is used named sulphur hexafluoride (SF₆). The second

process involves the deposition of a chemically inert passivation layer such as Teflon like substance produced by a gas source such as (C_4F_8) that protects the silicon substrate. In the following etching step the passivation layer at the bottom of the sample is bombarded with plasma ions etching the silicon. The passivation layer at the sides is sputtered off as the ions collide but the silicon is not etched, therefore deepening the trench in a near vertical dimension. These two steps are performed repeatedly over and over again to produce deep vertical side wall trenches on the silicon substrate. Short cycles produce smoother well defined walls at a slower etch rate with faster cycles producing a faster etch rate with lower quality of a defined wall to that of short cycles.

2.7.3 Metal deposition techniques

In silicon wafer processing the deposition of metals may be required in highly specific locations to give the desired structure and functionality of the finished product. Metal deposition processes such as the sputtering deposition process giving an atomically rougher topography (Xia and Whitesides 1996; Maya, Vallet et al. 1997) and the atomically smoother evaporation deposition process with a low root mean square (RMS) surface roughness (DeRose, Thundat et al. 1991; Ajit, Adina et al. 2006) that is most commonly employed. The deposition process performed is dependent on further processes used in the fabrication and topography required. As for the fabrication of the accelerometers; gold was selectively placed in specific locations to produce the gold bond pads and gold sensing tips. To allow gold to be deposited onto substrates such as silicon or glass, a titanium or chrome adhesion layer is commonly used. The use of an adhesion layer of titanium is used to deposit gold on silicon substrates as it allows better adhesion without affecting the dielectric properties of the gold (Vogt, Kohl et al. 1994). A titanium adhesion layer was used in this research to produce the evaporated gold layers (200 nm) on the accelerometers as outlined in the process flow.

2.8 Microfabrication Process flow for Accelerometer Device Types

The accelerometer devices were fabricated at the INEX MEMS foundry at Newcastle University by Mr Barry Dunne. Once the devices had been fabricated a detailed characterisation was performed to investigate the suitability for the application required. The next chapter will discuss the detailed characterisation of the accelerometers fabricated.

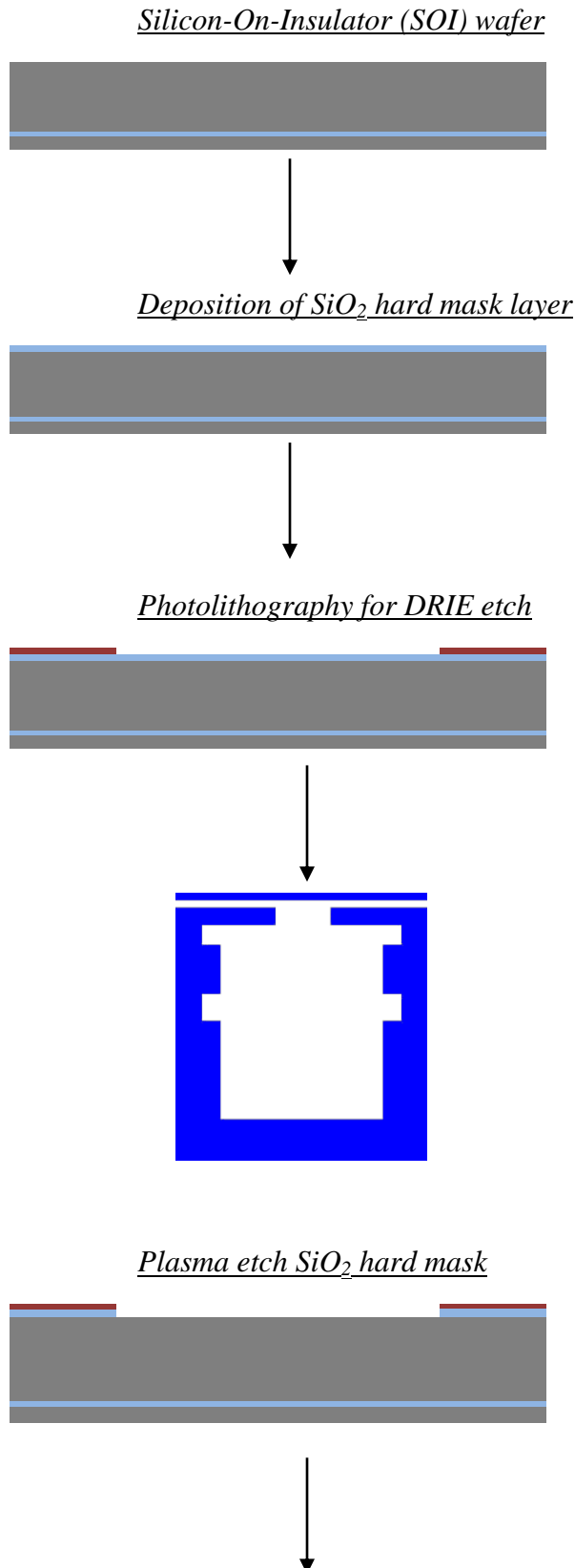
The information in Table 2-3 displays the properties of the silicon die device layer that was used to fabricate the accelerometer types.

Manufacturer	Ultrasil corporation, California	Comments
Device layer		
Die dimensions	900 x 900 μm	
Devices per die	4	
Masks used	3	
Silicon Type	p-type wafer	A p-type wafer was used to provide an ohmic contact
Crystal Orientation	<100>	
Thickness	15 μm	
Resistivity	0.1 Ohm/cm	
Finish	Polished	

Table 2-3: The silicon die device layer properties.

2.8.1 Accelerometer microfabrication process flow

The fabrication of the microaccelerometers was a three mask process that involved standard microfabrication techniques as discussed in the process flow below.



A SOI wafer with a 500 μm handle layer, 2 μm buried oxide (BOX) and 15 μm silicon thickness.

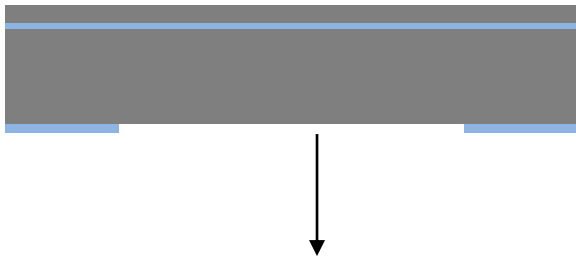
A hard mask was later used as the mask for DRIE of handle silicon

Positive photo-resist photolithography to pattern surface for DRIE

Mask Required (Mask#1)

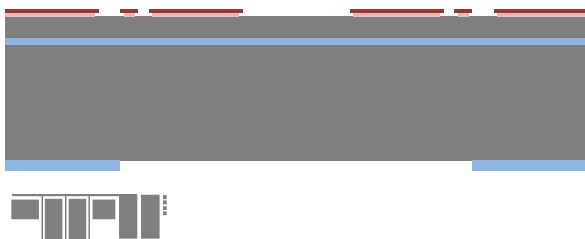
The use of a laser end-point system to determine etch time was performed. An Oxygen plasma etch to remove the SiO₂ in the desired locations.

Wet & dry removal of remaining photo-resist



Photoresist removal performed using wet chemistry with acetone.

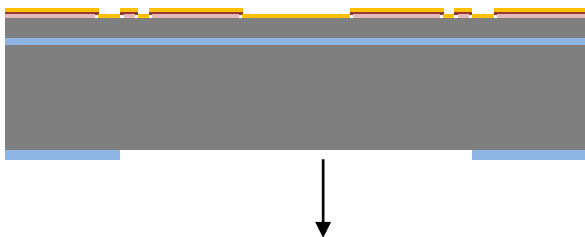
Photolithography of bi-layer pattern for lift-off of metal



Photolithography of bi-layer used to improve track definition
Front-to-back alignment

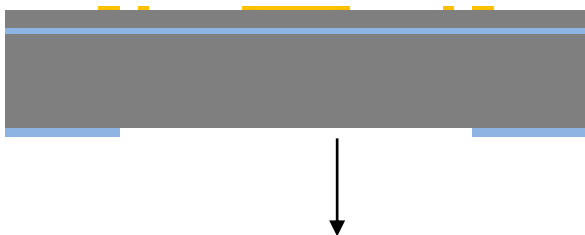


Deposit metal layer



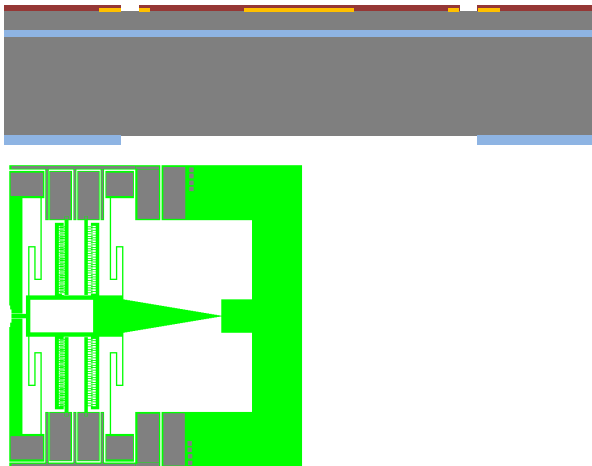
Ti/Au Metal Evaporation to selectively deposit Gold on the substrate surface.

Lift-off of residual metal/photo-resist



The photoresist being removed to allow gold to be removed specifically leaving a patterned gold surface.

Photolithography of device side silicon pattern



Photolithography of device side to define the membrane shape

Mask used to define final device geometry (mask#3).



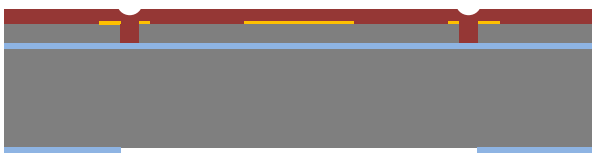
DRIE of device side silicon, stopping on BOX layer



Deep reactive ion etching was performed to etch through the device silicon to the BOX layer.



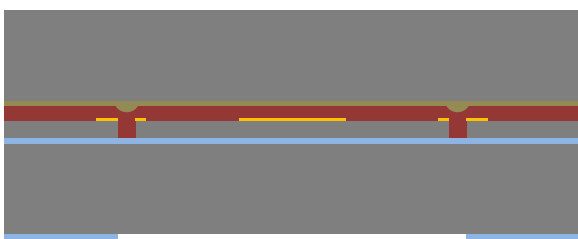
Resist Protection



A photoresist protection step is employed to assist with protecting the membranes during the DRIE of the handle layer silicon



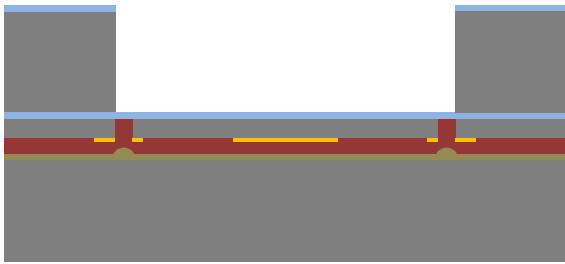
Wafer bond



The formation of a temporary bond to a backing wafer was performed to assist with the DRIE etch process of the handle silicon.



DRIE Handle silicon layer



The DRIE was stopped on the BOX layer.



Plasma etch BOX layer



An Oxygen plasma etch was undertaken to remove BOX layer.



Solvent release of die from backing wafer



A plasma clean was undertaken once the dies were removed from the solvent.

The fabricated dies are completed.

2.9 Fabrication and Characterisation Equipment

This section discusses the brief characterisation of the fabricated accelerometer types before the detailed in-depth characterisation that is discussed in chapter 3. The use of optical light microscopy and scanning electron microscopy was employed for the initial characterisation to give an observation of the fabricated structures.

2.9.1 Optical microscopy imaging

The fabricated accelerometer devices were first characterised using a Nikon eclipse 80i optical microscope equipped with a brightfield light filter to give a quick determination of how successful the fabrication met the required structural criteria. The image in Figure 2-14 shows the device to have the features required with relation to the geometry of the structures and the selective gold deposition process. The gold electrode contact pads crucially meet the criteria required that can be seen in the optical image, ensuring the gold regions are deposited correctly.

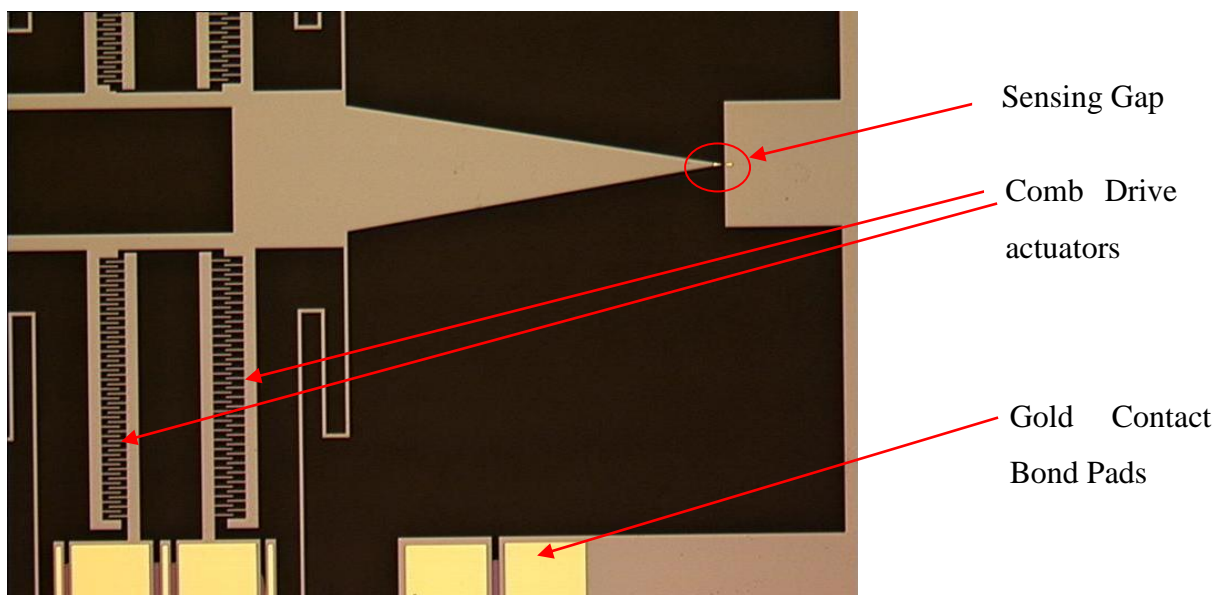


Figure 2-14: An optical image of a micromachined MEMS Accelerometer device.

The sensing gap with the gold tips being critical for the DNA functionalisation is shown in greater detail in Figure 2-15. The gold regions appeared to be correctly deposited in the required location for DNA positioning to be achieved.

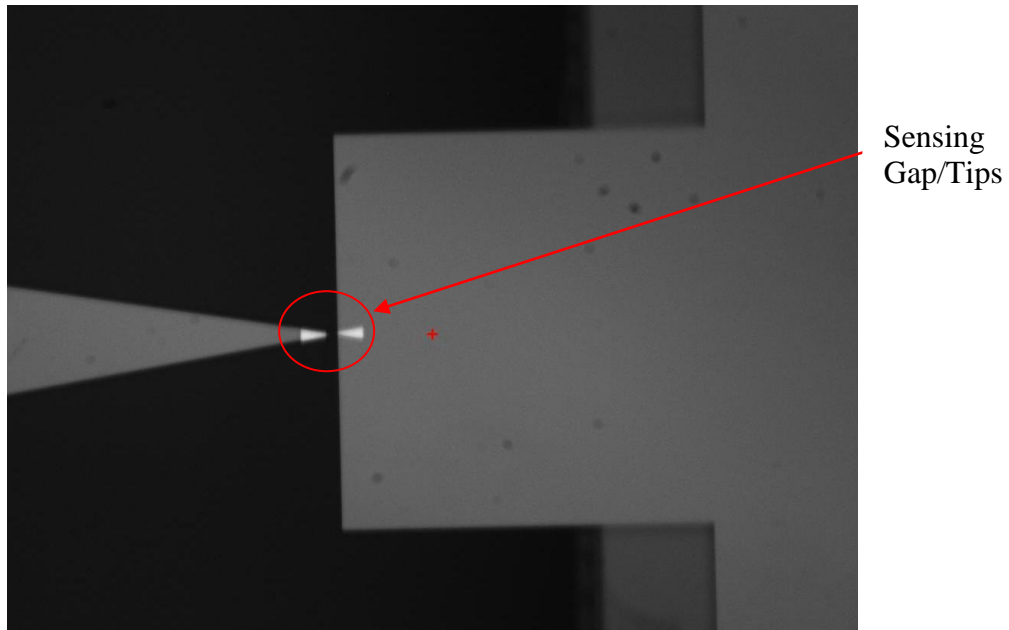


Figure 2-15: The gold sensing tips for the immobilisation of DNA, taken with an x20 objective lens.

The calibration tip of the accelerometer is shown in Figure 2-16 where the arrow indicates the in-plane motion along the sensing axis.

2.9.2

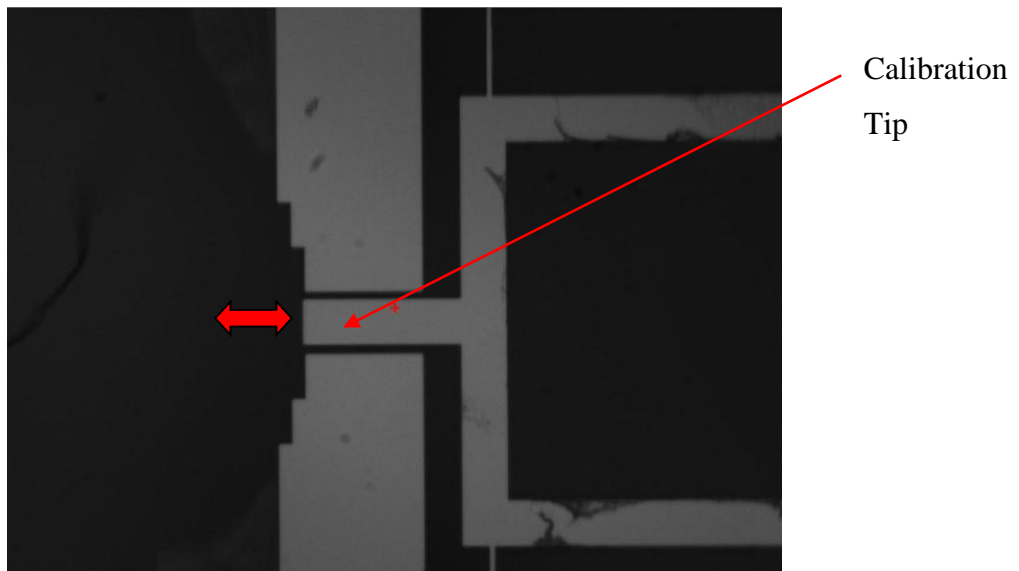


Figure 2-16: The calibration tip where the arrow indicates designed plane of motion, taken with an x20 objective lens.

2.9.2 Scanning Electron Microscopy

Scanning electron microscopy (SEM) is a non-contact method of acquiring high resolution images with a high magnification, superior to that of optical microscopy. SEM is not reliant on the power of a light which allows high magnification images to be obtained with a resolution of an nm to μm scale (Goldstein 2004). Unlike atomic force microscopy (AFM), SEM allows high magnification images to be produced rapidly without the need of physical contact. SEM has a large depth of field that produces images that appear to be 3 dimensional allowing the ability to produce feature rich images. The SEM imaging is achieved by scanning the sample with a high energy beam of electrons that interact with the atoms of the sample producing information about the samples electrical conductivity and surface topography. In a typical SEM an electron beam is emitted from an electron gun that can be focused by the use of condenser to reduce the spot size to 0.4 nm in diameter. The electrons are back scattered producing ‘back scattered electron’ beams, ‘secondary electrons’ and ‘X-rays’ from the surface of the sample. An electron detector is used to detect the electrons from the surface, a detector for each type of electron returning from the sample as illustrated in Figure 2-17. Hence, the SEM relies on imaging by the electrical conductivity of the surface, so therefore most samples need to be covered with a thin layer of gold to be deposited to allow high resolution images to be obtained.

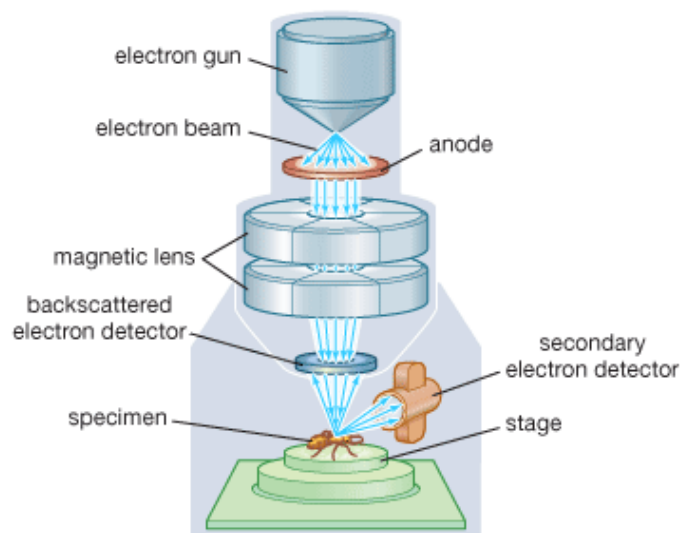


Figure 2-17: The components of an SEM instrument, taken from ref (Britannica 2009).

2.9.2.1 SEM imaging of fabricated accelerometer

SEM imaging was performed to obtain a general analysis of the fabricated accelerometer device types. The imaging was performed at the Electron Microscopy Research Services unit at Newcastle University under the supervision of Ms Tracey Davey. To ensure that high magnification images could be produced, a 10 nm gold layer was deposited onto the samples prior to being inserted into the instrument. The imaging was performed at an acceleration voltage of 8 kV using a working distance of 29 mm and 7 mm that was dependent on the tilt angle employed.

2.9.2.2 Complete accelerometer die imaging

The SEM analysis of a fabricated accelerometer die is shown in Figure 2-18 that is an entire accelerometer device. The imaging revealed that there are no obvious defects in the device. The springs, gold bonds pads and calibration tip are shown to be fabricated to the standard required though higher magnification images were obtained to give a more detailed investigation.

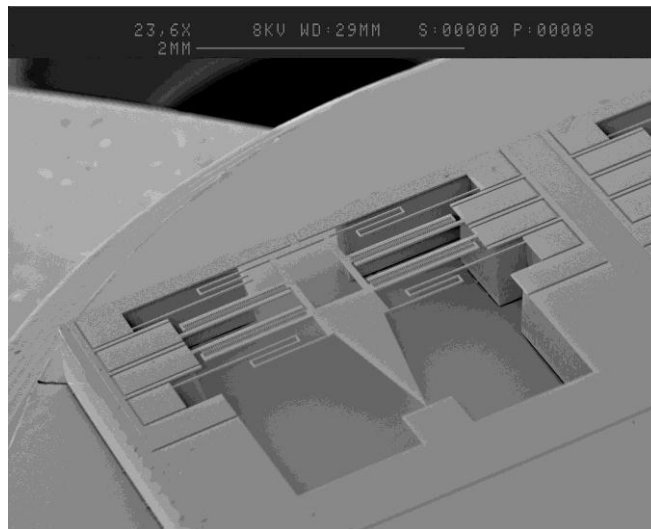


Figure 2-18: An SEM image of an entire accelerometer device with a tilt angle of 45 ° giving a 3 dimensional appearance.

2.9.2.3 Comb drive

The comb drive dimensions, one of the critical factors for the accelerometer device to be fully functional were investigated. It is mostly important that the comb drive fingers between stator and rotor have not become interlocked by static friction (stiction) that can occur when wet chemical processes have been used in the fabrication (Mastrangelo and Hsu 1993) (Spengen and et al. 2002). The images in Figure 2-19 show that the comb drives were fabricated to the standard needed and the fingers spaced evenly.

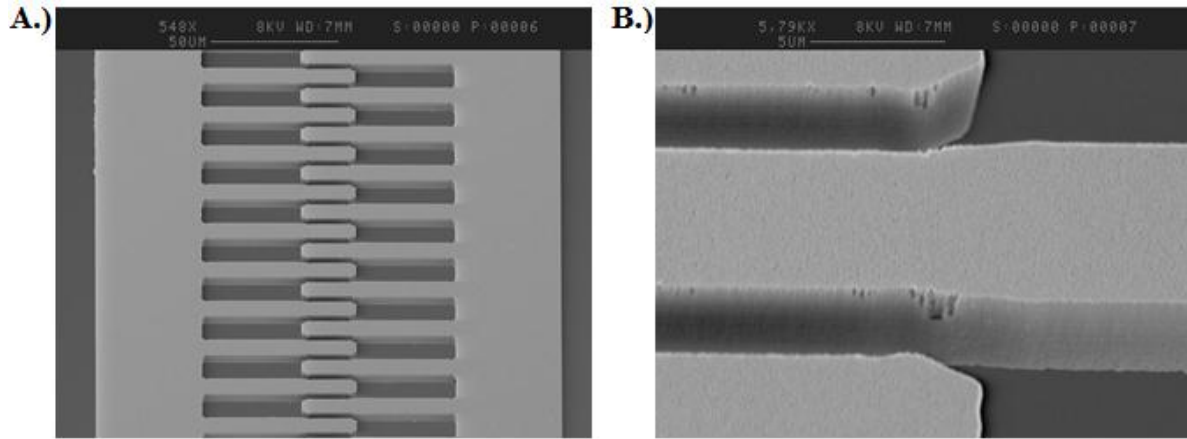


Figure 2-19: Two SEM images for comb drive of an accelerometer device. The left image shows an overview of the comb drive, the scale bar being 50 μm. The right image showing a higher magnification image of the overlapping comb drive fingers, the scale bar represents 5 μm.

2.9.2.4 Sensing gap

The SEM analysis allowed an initial analysis to confirm if the sensing gap was fabricated without any obvious defects and to give an indication of the surface roughness. The images obtained that are displayed in Figure 2-20 confirmed that the gold tips were deposited correctly with a low surface roughness, though a more detailed characterisation was performed using Zygo interferometry that is discussed in chapter 3. The sensing tips are shown to be relatively parallel and in-plane to the opposing sensing tip. The scale bar on the image is not accurate as a tilt angle to the surface normal was employed which gives a $\pm 10 \mu\text{m}$ tolerance.

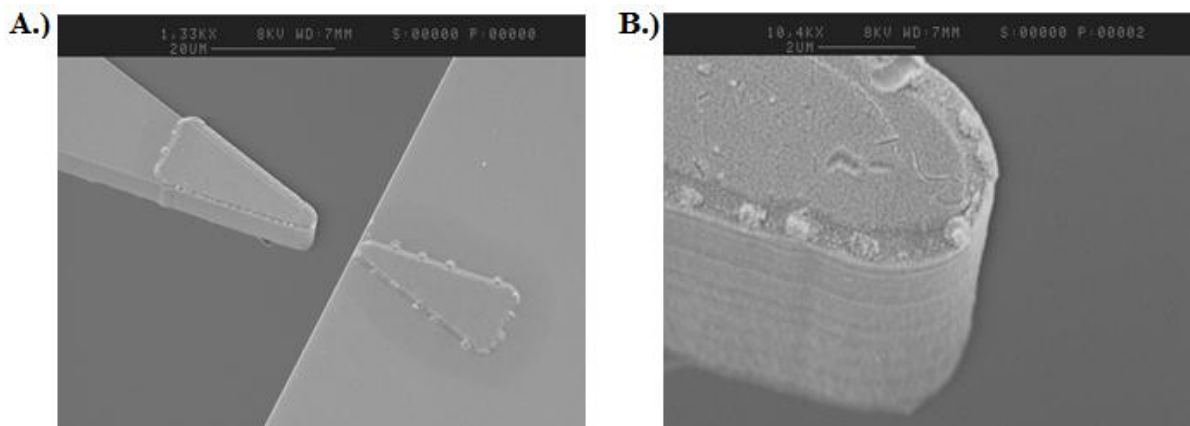


Figure 2-20: SEM images of the gold sensing tips. The left image shows the sensing gap between the tips, the scale bar represents 20 μm. The right image shows a high magnification image of the floating sensing tip, the scale bar equals 2 μm.

2.10 Summary and conclusions

The accelerometer types were designed, modelled and fabricated to allow the application of a biological accelerometer. The modelling allowed the envisaged performance to be determined before fabrication regarding the mode shapes and static deflection properties. The type 1 accelerometer was modelled to give the largest deflection per volt applied to combs. All the accelerometer types were all successfully fabricated to the structural criteria specified without any major problems which could be from the brief characterisation by optical microscopy and SEM.

3 Chapter 3 Accelerometer Testing and Characterisation

This chapter discusses the detailed characterisation that was undertaken to measure the outcomes of the performance between the accelerometer types. The testing first involved using the Zygo metrology instrument to determine the sensing gap distance and to further perform electrostatic deflections measurements to investigate the suitability to stretch positioned DNA. Secondly, a frequency analysis was performed using the laser vibrometer where mode shapes were compared to the ANSYS FEA undertaken prior to fabrication.

3.1 Introduction

The process of the testing and characterisation of the accelerometer types was carried out in three parts;

1. The determination of fabrication success where the feature size for; the sensing gap, comb drives, support springs and calibration tip of the three types were analysed using a white light interferometry (Zygo profiler) metrology system. This allowed the devices to be characterised within a sub-micron resolution in the *X*, *Y*, and *Z* axis.
2. The electrostatic deflection measurements of the accelerometer types were performed using a range of voltages applied to the comb drives and the degree of static deflection was measured. The values obtained are compared with the modelled data from chapter 3.
3. The determination of the natural resonant frequency and mode shapes of the accelerometer types were measured by employing laser Doppler vibrometry. A comparison of the frequencies and mode shapes between the theoretical and empirical results are compared.

3.2 Characterisation Equipment

3.2.1 White Light Interferometry

White light interferometry (WLI) is a non-contact method of surface profiling a substrate allowing the surface topography and step heights to be measured (Deck and de Groot 1994). The technique relies on optical interference fringes to surface profile the sample by a beam of white light. The beam of light generated by the bulb is split into two parts by a beam splitter, one beam passing to a reference surface and the other to the sample. The returned beams are recombined through a Mirau objective and sent to the charged coupled device (CCD) detector array system for imaging, as highlighted in Figure 3-1. The supporting computer software named 'Newview Metropro' allows the user to retrieve metrological data from the sample surface.

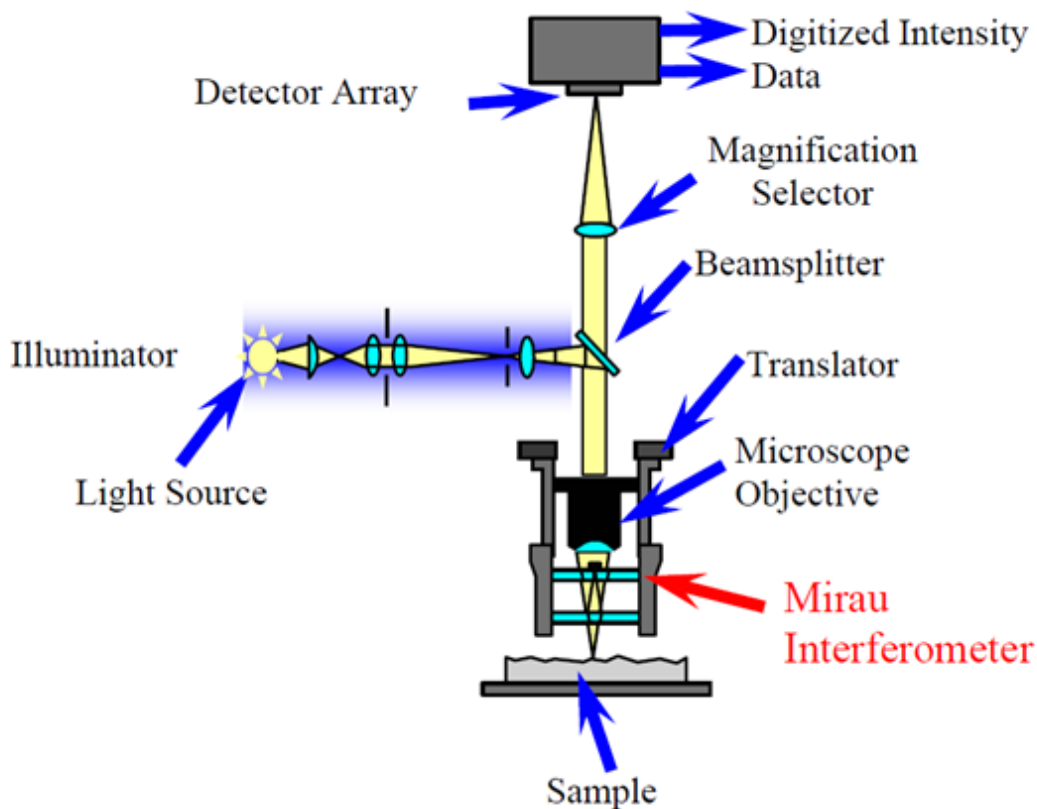


Figure 3-1: A schematic showing the fundamentals of a white light interferometer.

The Zygo interferometry system was employed to measure the static deflection induced by electrostatic actuation using a range of driving voltages that was compared between the three accelerometer types. The Zygo profiler apparatus used in this research to perform the static

deflection measurements by observing the calibration tip is displayed in Figure 3-3 alongside the laser Doppler vibrometer instrument.

3.2.2 Laser Doppler Vibrometry

The laser Doppler vibrometer (LDV) is a non-contact instrument that is employed to measure the resonant frequency of a system; for the case of this research it was used to monitor the calibration tip of the accelerometers to determine the frequency and modeshape. LDV relies on the use of a laser and photodiode assembly to perform measurements quickly and accurately. There are many commercial variations though generally a LDV is a laser interferometer that incorporates an internal reference beam and test beam produced by a beamsplitter as highlighted in Figure 3-2. The test beam is directed to the target substrate, where the motion of the substrate causes a Doppler shift of the laser beam. A portion of the reflected test laser beam is reflected along to the photodetector by the beamsplitter and combined with the reference beam. The LDV works by using a heterodyne system; where a frequency shift is attributed to the test beam by the Bragg cell which is reflected back alongside the reference beam to the photodetector, allowing the generation of a signal at a known frequency before modulation. The modulation of the combined test and reference beams by a signal analyser allows the resonant frequency shift of the test substrate to be measured.

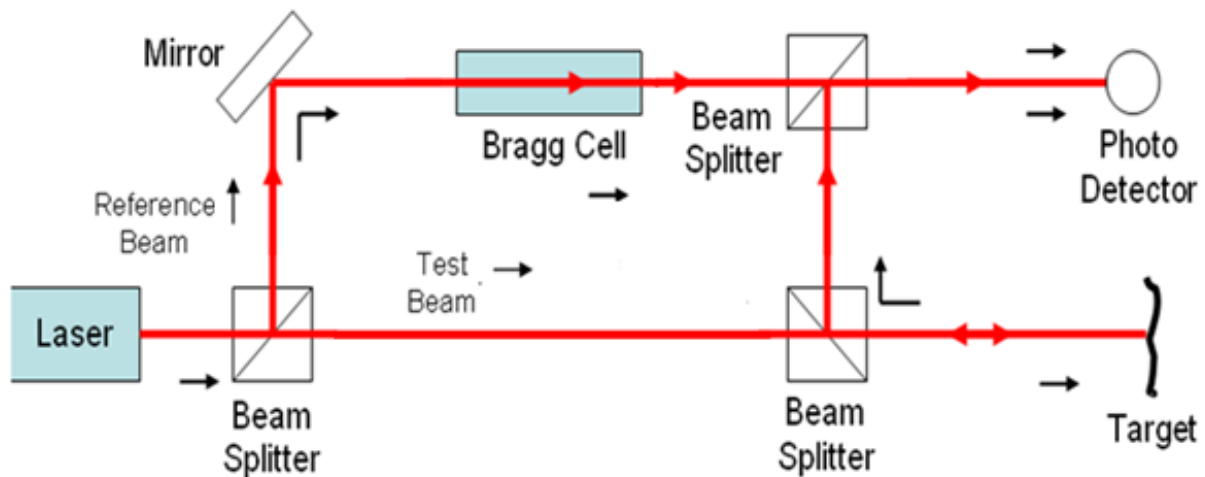


Figure 3-2: A schematic showing the main components of a laser Doppler vibrometer

The Polytec LDV system was employed for this research which was used in conjunction with a Hewlett Packard signal analyser coupled to a Zygo profiler that contained a custom made beam splitting objective. This allowed the laser spot to be focused on the accelerometer calibration tip for the frequency and static deflection measurements. The LDV assembly that

was employed is shown in Figure 3-3 panel A where panel B shows an accelerometer device situated onto one half of a DIP for the measurements. The accelerometer DIP assembly was stuck firmly using wax to a piezoelectric shaker to orientate the accelerometer in an upright geometry, giving access for the LDV laser spot from above. This arrangement permitted the frequency measurements to be performed alongside the static deflection measurements with the same basic setup. The images shown in Figure 3-3 include an accelerometer DIP assembly attached to the piezoelectric shaker and the Zygo profiler alongside a power supply employed to generate the DC voltage that were used in this study.

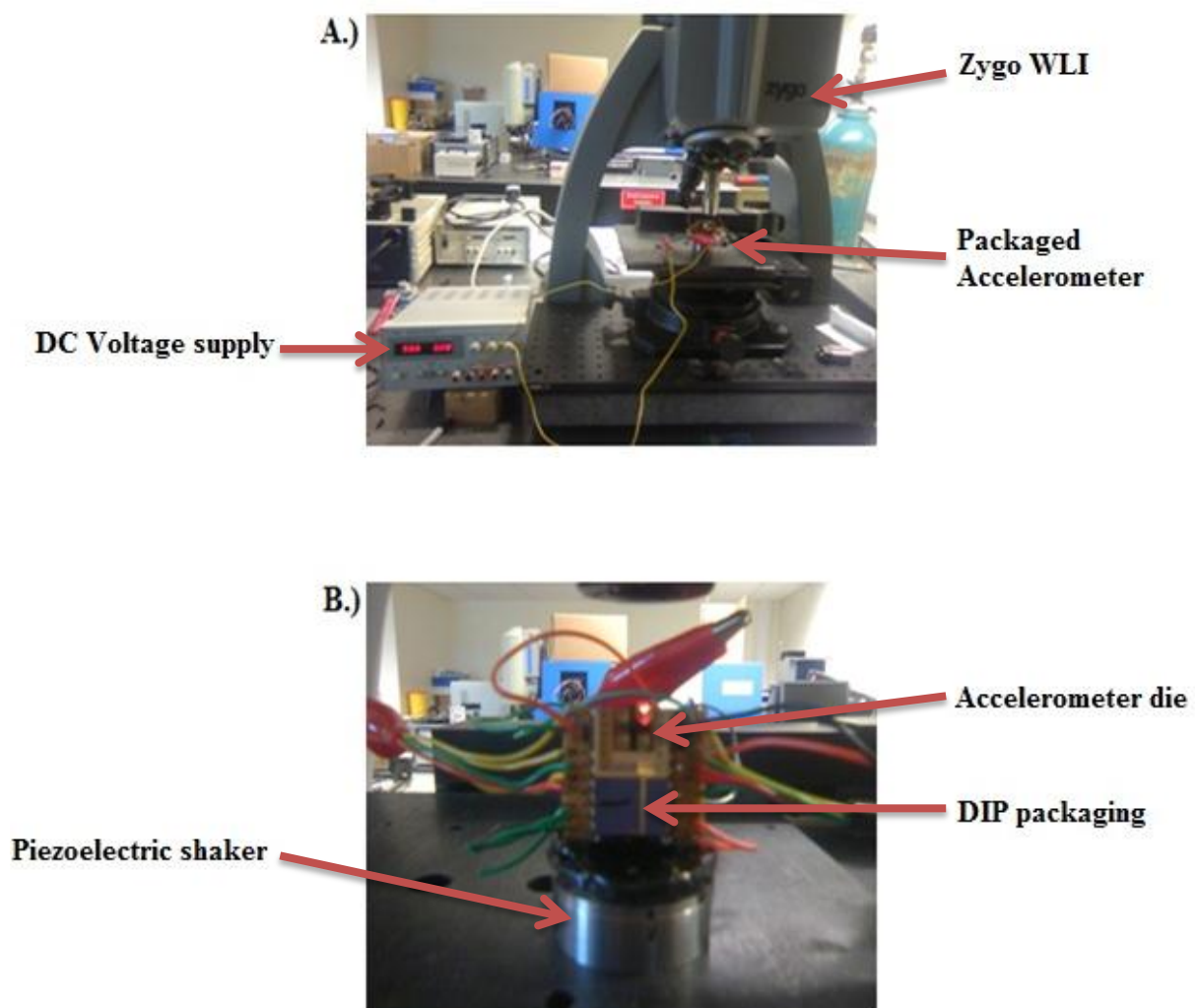


Figure 3-3: A.) The Zygo profiler instrument and DC power supply during measurements. B.) The packaged and mounted accelerometer that was electrically connected to the DC power supply.

3.3 Accelerometer fabrication review of structural dimensions

The structural criteria that was outlined in chapter 2 is discussed further this section. The features of high interest being; the sensing gap, the comb drive finger spacing, spring width and calibration tip. The varying feature dimensions between the accelerometer types were envisaged prior to fabrication by modelling to affect the natural frequencies and amount of static deflection performed. This section discusses the outcome of the fabrication by employing WLI to scrutinise the features with LDV to provide empirical data of the performance of the accelerometer types.

3.3.1 Sensing gap

The sensing gap was investigated to ensure that the distance was suitable for the application of DNA molecule placement, the distance was highly important for device operation. The decision to use λ -DNA was made because the crystallographic length of the molecule is 16.2 μm , a molecule of this length allowed for lower tolerances in the fabrication.

A non-contact analysis was performed using the Zygo profiler to obtain metrological information of the sensing gap proportions. The sensing gap distance was measured to be 10 μm (± 0.4) rest without electrical actuation as detailed in Table 3-1. The images in Figure 3-4 show the metrological data of the sensing gap of one of the accelerometers investigated, where the sensing tips are insignificantly out-of-plane by 0.5 μm which was not envisaged to effect device operation.

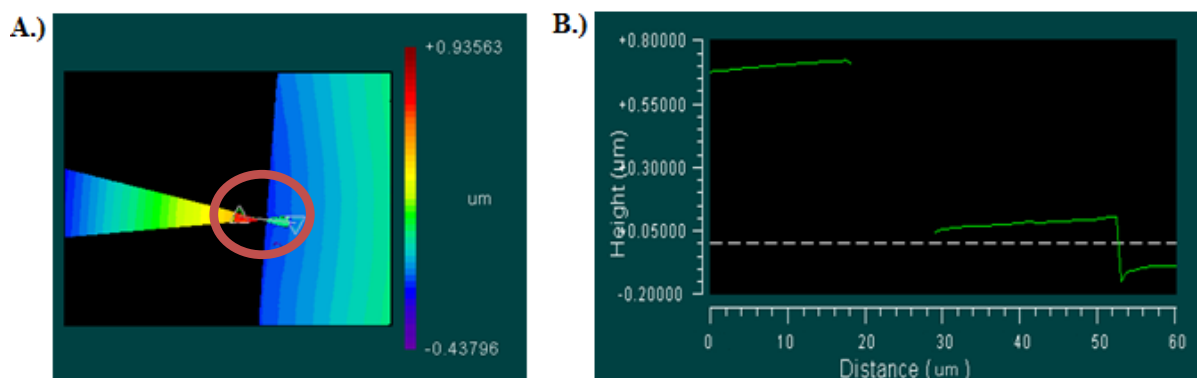


Figure 3-4: A.) The sensing gap height map which shows sensing tip deflecting out-of-plane. B.) The corresponding height profile of the region which is indicated by the circle in A.)

3.3.2 Comb drive

The three accelerometer types that were fabricated with differing comb drive features were examined. The comb drives of the types were analysed with the Zygo profiler so that the performance of the types could be scrutinised with regards to the feature size. The type 1-3 comb drives were investigated to determine if stiction had occurred during the fabrication and to see if they underwent out-of-plane deflection that may affect performance during actuation. The metrological data in Figure 3-5 shows the dimensions of type 1 comb drive. The height profile indicates that out-of-plane displacement of the comb rotor and stator had occurred along the Z axis by $2.2\ \mu\text{m}$, which is 14 % of the device layer thickness. The overlapping finger distance for the type 1 was measured to be $2.3\ \mu\text{m}$ (± 0.2).

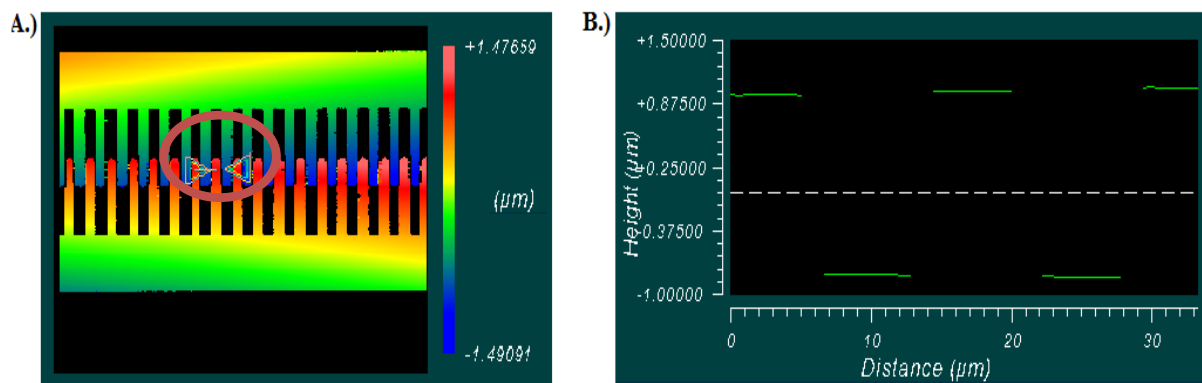


Figure 3-5: A.) The height map of a type 1 accelerometer comb drive. B.) The corresponding height profile indicated by the region indicated by the line in the circle in A.).

The height map and profile displayed in Figure 3-6 for a type 3 accelerometer shows the overlapping finger spacing to be approximately $9\ \mu\text{m}$, the average value is listed in Table 3-1. The comb drive stator and rotor appear to be out-of-plane with a constant distance in the Z-axis across the entire length of comb. The height profile indicates that the proof mass is elevated out-of-plane by a value of $0.26\ \mu\text{m}$.

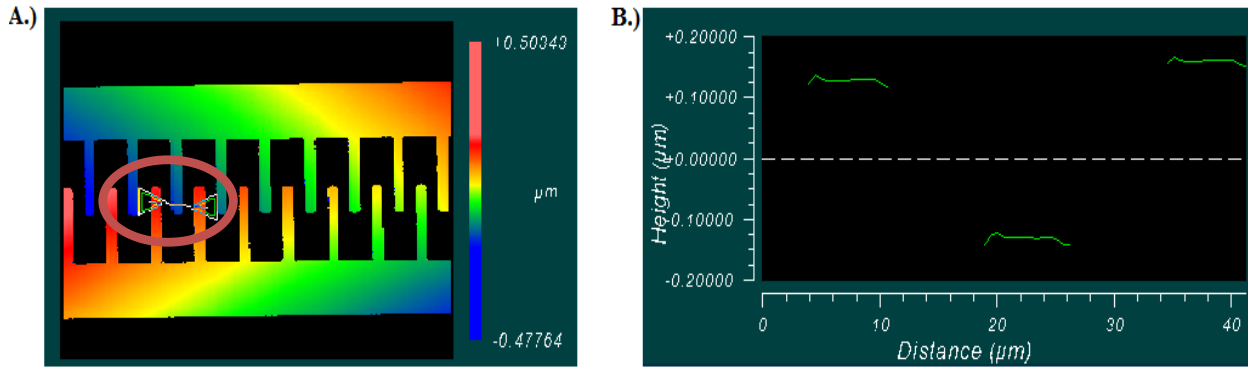


Figure 3-6: A.) The height map of a type 3 accelerometer comb drive. B.) The corresponding height profile indicated by the region indicated by the line in the circle in A.).

3.3.3 Support Spring

The support springs of the accelerometer types are scrutinised in this section to determine if they were fabricated to specification. As discussed, the spring width was specified to vary between types, where type 1 was designed to have a spring width of 5 μm and type 2+3 to be 12 μm.

The support spring examined for a type 3 accelerometer is illustrated in Figure 3-7 which indicates that the spring width is approximately 13. μm. The spring width values showed little variation for this type, the average value obtained is presented in Table 3-1 alongside the measurements of the other accelerometer types.

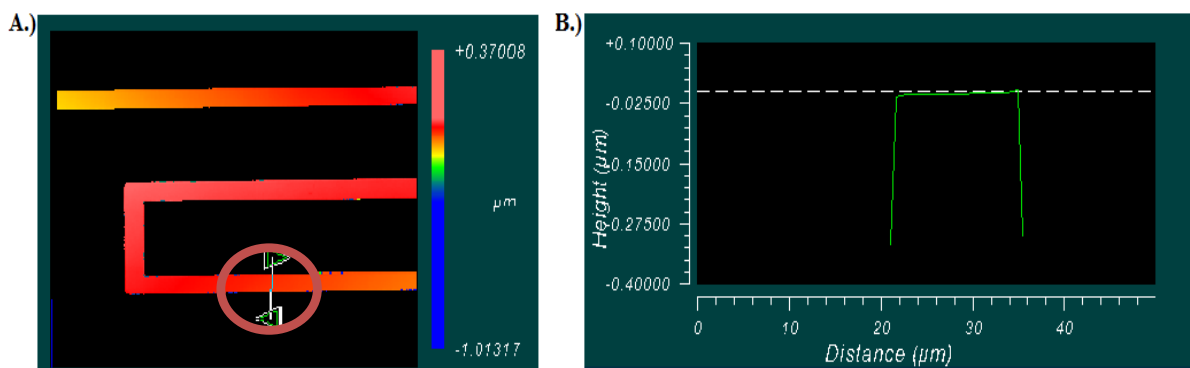


Figure 3-7: A.) The support spring height map of a type 3 accelerometer. B.) The corresponding height profile indicated by the region indicated by the arrow in the circle in A.).

3.3.4 Calibration tip

The calibration tip that was designed to provide access for measurements to be obtained was analysed. The feature size was in agreement with the limits that were proposed with the initial designs. The data displayed in Figure 3-8 highlights the calibration tip dimensions were fabricated to specification, though showing an out-of-plane displacement of 0.6 μm which was not problematic for undertaking the performance measurements.

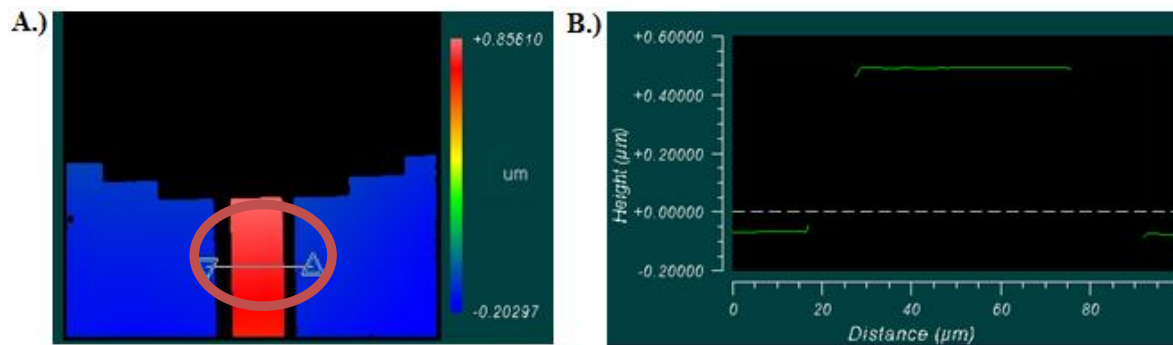


Figure 3-8: A.) The calibration tip height map of a type 3 accelerometer. B.) The height profile of the region indicated by the line in the circle in A.).

3.3.5 Comparison of measured feature size between accelerometer types

The metrological data that was collected for the three accelerometer types is listed in Table 3-1 that highlights the specified values and the actual values measured.

Device type n=3	Type 1 (μm)	Type 2 (μm)	Type 3 (μm)
Envisaged spring width feature size	5	12	12
<i>Measured mean value</i>	5.4 (± 0.3)	11.4 (± 0.3)	13.3 (± 0.5)
Envisaged comb overlapping finger distance	2.5	2.5	10
<i>Measured mean value</i>	2.3 (± 0.2)	2.2 (± 0.5)	8.9 (± 0.3)
Envisaged sensing gap distance	10	10	10
<i>Measured mean value</i>	10.4 (± 0.3)	10.8 (± 0.4)	10.6 (± 0.4)

Table 3-1: A comparison showing the dimensions specified for the accelerometer types and the actual measured dimensions. The standard deviation is indicated by \pm .

The spring width and the overlapping finger distance values that were measured for accelerometer types 1-3 indicated that the structural specifications were met. For the fabrication to be fruitful the sensing gap was primarily the most important feature to be fabricated to specification. The spring width and comb drive dimensions being secondly as important for the increasing decreasing the sensing gap by the electrical actuation of the combs. As shown in the table, the sensing gap was fabricated to specification for all accelerometer types. This established that all accelerometer types were suitable to be employed for the DNA immobilisation and positioning protocols. The accelerometers deflecting out-of-plane prior to actuation will allow less overlap of the comb fingers and a larger voltage may be required to compare with the modelled behaviour. The next section involves the static deflection measurements by electrostatic actuation of the combs for all types.

3.4 Static deflection measurements of the electrostatically actuated accelerometers

An investigation was undertaken to measure the degree of static deflection of the accelerometer types when electrostatically actuated by a range of DC voltages. The modelling predicted that deflection would increase linearly with the applied voltage, this will increase or decrease the sensing gap distance depending on the comb drive actuated. The metrological data displayed in Figure 3-9 shows the calibration tip of an electrically connected accelerometer DIP assembly in the upright orientation as displayed in Figure 3-3. The degree of static deflection of the proof mass was determined by observing the deflection of the calibration tip compared to the calibration planes positioned at either side. The calibration planes are static features that don't undergo actuation, therefore giving two reference surfaces to allow a zero plane to be used to measure the degree of static deflection.

The images in Figure 3-9 show the calibration tip before and during the electrostatic actuation of comb drive 2 giving a positive deflection in the Z-axis compared to the calibration planes. An electrical potential of 20 V (400 V^2) was applied to the comb that deflected the proof mass whilst increasing the sensing gap distance. The calibration tip deflecting in the Z axis is highlighted red in panel C compared to the static reference planes which remain stationary that are highlighted blue. The height profile indicates that the calibration tip had deflected by $2.29 \mu\text{m}$ in the actuation plane. Alternatively the electrostatic actuation of comb drive 1 decreased the sensing gap distance (not shown in the figure) by deflecting the proof mass in the opposite direction.

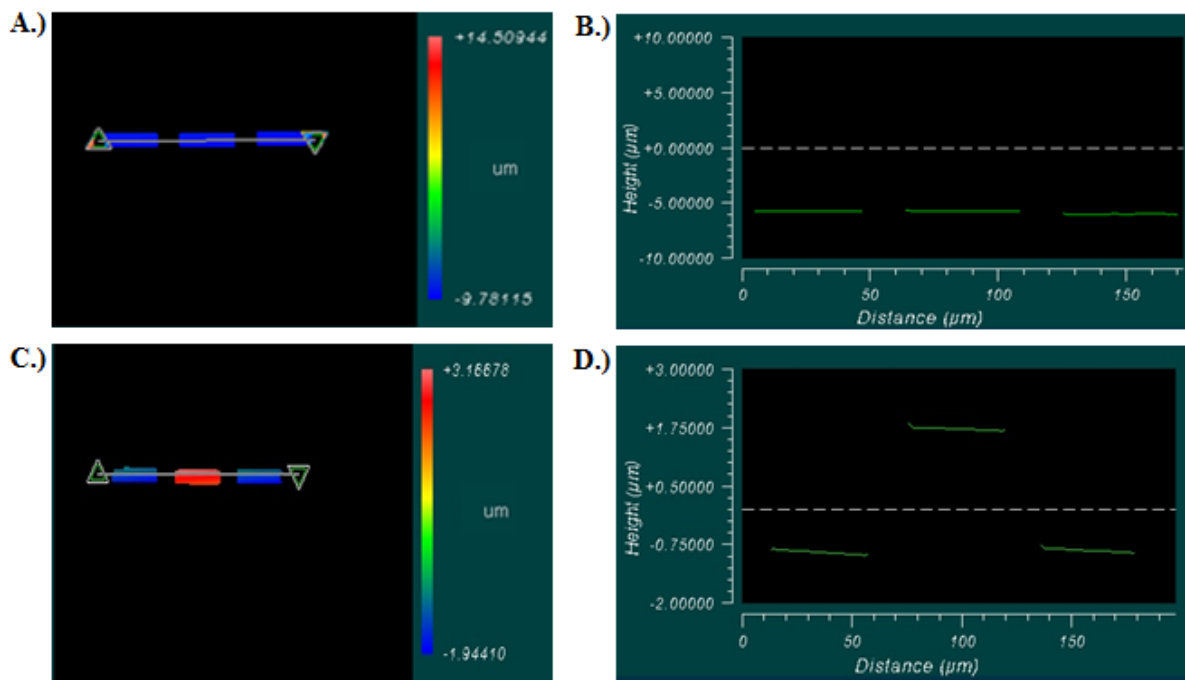


Figure 3-9: A.) A height map of the calibration tip of a type 1 accelerometer prior to electrical actuation. B.) The corresponding height profile of the region indicated by the line in the height map. C.) A height map of the calibration tip undergoing static deflection by electrical actuation of comb drive 2 with an applied voltage of 20 V (400 V^2). D.) The corresponding height profile of the region indicated by the line in the height map.

3.4.1 A comparison of the static deflection measurements of accelerometer types

The degree of static deflection for the accelerometer types was investigated by electrostatically driving the comb drive actuators with an applied voltage. The comb drives 1+2 were electrostatically actuated separately and the amount of static deflection measured.

3.4.1.1 Electrostatic Comb actuation

The maximum voltage applied to the type 1 accelerometer varied slightly between combs as they were prone to electrical shorting due to lateral displacement that caused irreversible mechanical damage to the structures. The combs of each actuation direction (1+2) of type 1 were separately applied with an electrical potential of 30 V (900 V²) and 20 V (400 V²) respectively. The type 2+3 combs (1+2) were all applied with a maximum voltage of 55 V (3025 V²) before failure, the larger spring width may have reduced the possibility of lateral displacement from occurring that may be the cause of electrical shorting. The voltage was increased linearly from 0-24 volts DC in 2 volt increments and in 5 V increments thereafter to 55 V. The data in Figure 3-10 and Figure 3-11 displays the mean measured deflection with the voltage applied for all accelerometer types.

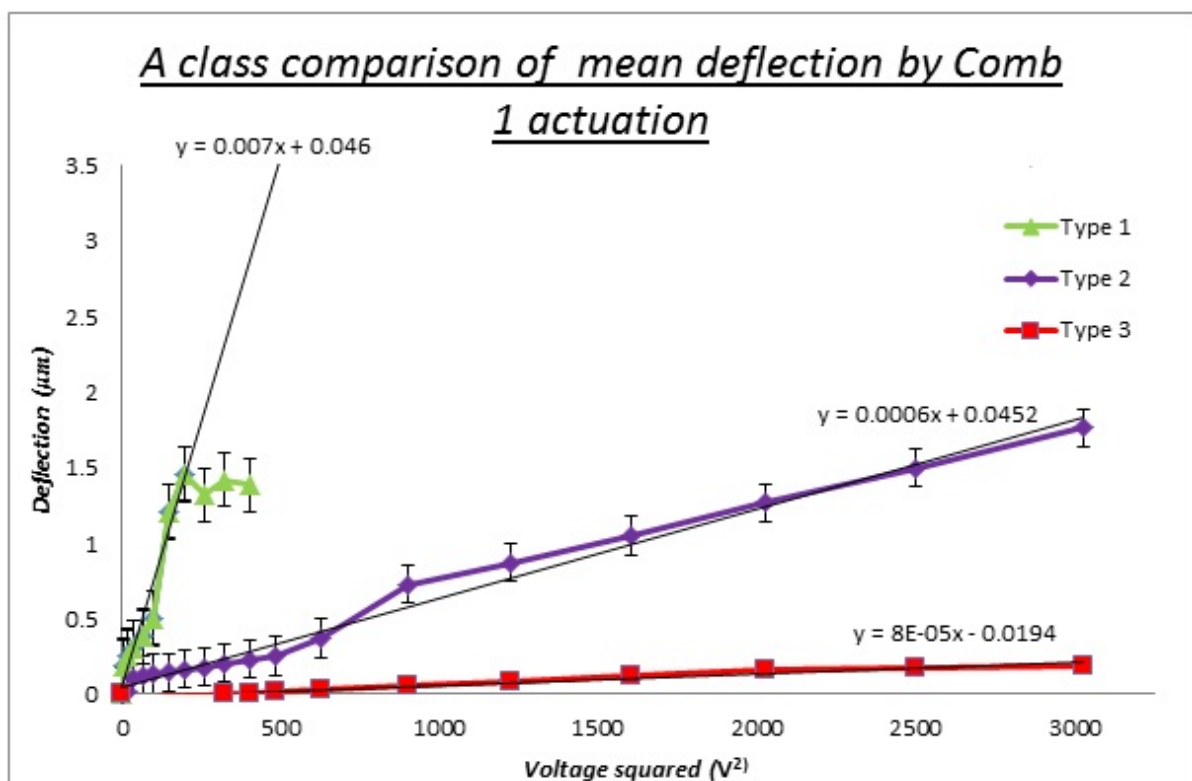


Figure 3-10: A comparison of mean deflection of comb drive 1 electrical actuation of all accelerometer types, $n=5$ for each accelerometer type. The trendlines indicate the $\mu\text{m}/\text{V}^2$ gradient value for each type.

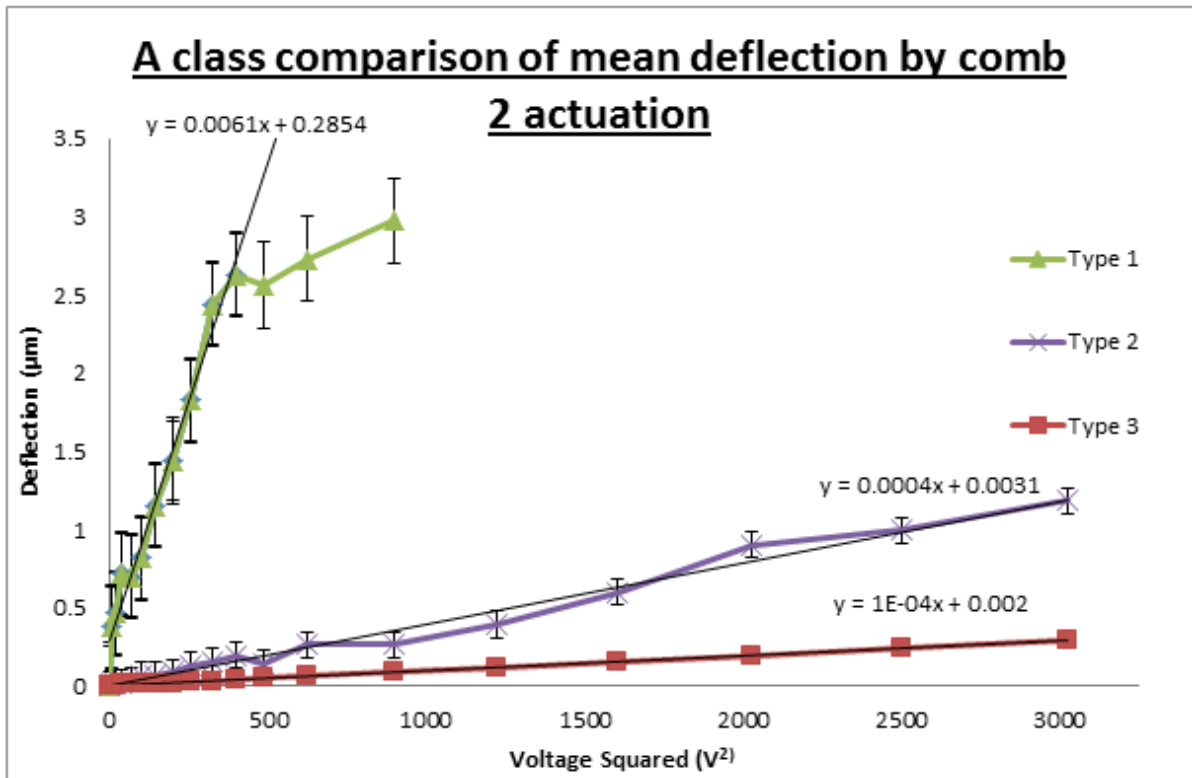


Figure 3-11: A comparison of mean deflection of comb drive 2 electrical actuation of all accelerometer types, $n=5$ for each accelerometer type. The trendlines indicate the $\mu\text{m}/\text{V}^2$ gradient value for each type.

The type 1 accelerometer performed the largest mean deflection measured with comb 2. The rate of static deflection initially began to plateau before structural failure which is more apparent for comb 1, indicating that a structural constraint may be the contributing factor. An example of a constraint being the interlocking of the comb fingers during actuation which can be common for this type of actuator. The investigation indicated that the combs may have reached the maximum physical deflection limit that could be achieved. The combs were designed to have $40 \mu\text{m}$ room to deflect in-plane which indicates that lateral displacement may have occurred. The next section discusses the investigation to determining the cause of the lower than envisaged performance.

Accelerometer type (n=5)	Type 1	Type 2	Type 3
Comb drive 1 maximum mean static deflection (decreasing sensing gap)	1.39 μm (± 0.6)	1.76 μm (± 0.5)	0.19 μm (± 0.1)
Comb drive 2 maximum mean static deflection (increasing sensing gap)	2.98 μm (± 0.4)	1.18 μm (± 0.3)	0.29 μm (± 0.06)
Maximum voltage applied before failure	30 V	55 V	55 V

Table 3-2: A comparison of the performance of the accelerometer types.

As determined by modelling discussed in chapter 2, the performance of the accelerometer types by the electrostatic force generated by the combs and the spring restoring force was confirmed by the empirical data. It is shown that the comb 1 showed similarity of performance with the maximum deflection values with type 1+2, though type 2 was performed with a greater applied voltage. The type 1 maximum deflection may have been much larger if the structures had not undergone premature mechanical failure during actuation. As envisaged the type 3 accelerometer performed the lowest measured mean deflection when the combs were actuated (combs 1+2) with a maximum mean value of 0.29 μm with comb 2.

The data in Table 3-3 displays a comparison of the deflection gradients of the modelled and empirical data obtained, the comparison of the gradients between the types are in close agreement with one another. As was envisaged the type 1 accelerometer showed the largest empirical value of $7.0 \text{ E-}03 \mu\text{m}/\text{V}^2$ compared the modelled value of $4.8 \text{ E-}03 \mu\text{m}/\text{V}^2$. Though these were calculated by disregarding the deflection plateau that was observed for the type 1 accelerometer. The empirical values of the deflection gradients for the type 2+3 are in closer agreement with the modelled data than type 1 as a deflection plateau was not observed. The difference observed between the values being due to small errors that always involved with modelling.

Accelerometer type (n=5)	Type 1	Type 2	Type 3
Modelled deflection gradient ($\mu\text{m}/\text{V}^2$)	4.8 E03	4.0 E04	5.0 E05
Empirical deflection gradient ($\mu\text{m}/\text{V}^2$) comb 1	7.0 E03	6.0 E04	8.0 E05
Empirical deflection gradient ($\mu\text{m}/\text{V}^2$) comb 2	6.1 E03	4.0 E04	10 E05
Maximum voltage applied before failure	30 V	55 V	55 V

Table 3-3: A comparison of the measured static deflection of the accelerometer types with the predicted modelled values using ANSYS.

As expected from the static analysis modelling the type 1 accelerometer showed the best measured performance which allowed it to be chosen as the most suitable for the application of a DNA biological accelerometer. It was initially unclear the reason for the deflection plateau and mechanical failure that was observed for the type 1 accelerometer. An investigation was performed to determine the reason which is discussed in the next section on page 74.

3.5 Out-of-plane Analysis of electrically actuated accelerometer type 1

An analysis was performed to determine if the deflection plateau observed for the type 1 accelerometer devices was due to lateral displacement of the combs. A type 1 accelerometer was electrically connected exactly as the static deflection investigation and actuated with the maximum applied voltage and observed in the out-of-plane orientation using the Zygo profiler. The actuating comb structures were scrutinised to determine if irregularities occurred during actuation and to provide a conclusion to the performance outcome.

3.5.1.1 Comb 1

The comb drive 1 was electrically actuated with the maximum applied voltage that was applied to this type for the static deflection experiments at 20 V (400 V^2). The profile measurements confirmed that lateral displacement of the comb drive rotor and stator did occur, which is highly likely to be the explanation of the deflection plateau observed. The metrological information that was obtained is displayed in Figure 3-12 which shows the comb drive undergoing lateral displacement and out-of-plane deflection of the comb rotor to the stator. The height map confirms that lateral deflection had taken place. This confirms that two fingers were undoubtedly stuck together due to lateral displacement.

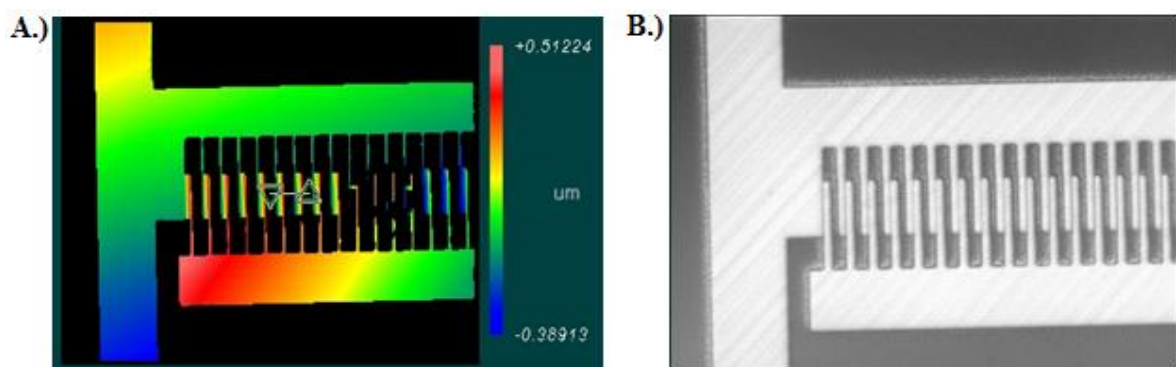


Figure 3-12: A.) The height map of comb 1 of the type 1 accelerometer actuated with 20 V (400 V^2). B.) The intensity plot highlighting the comb drive undergoing lateral displacement.

3.5.1.2 Comb 2

The comb drive 2 was likewise electrically actuated and viewed in the out-of-plane orientation. The comb was actuated with the maximum applied voltage for comb 2 of type 1 during the deflection measurements. The image in Figure 3-13 shows the lateral displacement of the comb drive and the unintended out-of-plane deflection. As displayed in Figure 3-11, the degree of deflection when actuating comb 2 decreased before mechanical failure occurred. The performance of the type 1 accelerometer when actuated with a higher applied voltage is uncertain as the combs were not actuated using more than 30 V ($900V^2$) because of the risk of mechanical failure caused by lateral displacement.

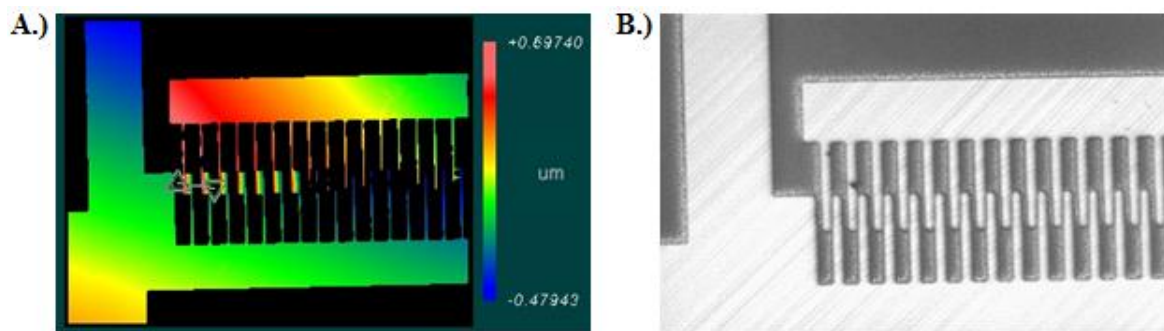


Figure 3-13: A.) The height map of comb 2 of the type 1 accelerometer actuated with 30 V ($900 V^2$). B.) The intensity plot showing the comb drive undergoing lateral displacement.

It was concluded that the lateral displacement of the floating proof mass reduces the performance of the accelerometer compared to what was envisaged during the design and modelling process.

3.5.1.3 Cause of lateral displacement

The main cause of lateral displacement for comb drive actuators is chiefly ‘pull in’ where the comb drive fingers from opposing combs become too close during electrical actuation. The fingers are electrically pulled towards one another laterally, where they may become fixed during and after actuation. This is a common problem for this type of actuator and has been discussed in the literature in detail (Legtenberg and et al. 1996; Elata and Leus 2005). When a voltage is applied across an actuator electrode capacitor causing deflection, the generated force will be opposed by the structural springs. Though as the rotor actuates it can become too close to the stator due to asymmetry of the fabricated structures and can experience pull-in. The pull-in phenomenon usually arises when the lateral distance between the stator and

the rotor is exceeded by one third of the distance, as a result of the electrostatic force becoming larger than the spring restoring force (Legtenberg and et al. 1996). This causes the comb fingers to pull together and stick rendering the actuator inoperable.

The issue of lateral displacement for the accelerometer types may have been due to the asymmetry of the fabricated structures. It was shown by the initial characterisation detailed in section 3.4 that the structures were showing out-of-plane deflection twisting prior to actuation. The type 1 accelerometer displayed the largest amount of static deflection compared to types 2+3 with a maximum deflection gradient of $7.0 \text{ E-03 } \mu\text{m}/\text{V}^2$ and a theoretical modelled gradient of $(4.8 \text{ E-03 } \mu\text{m}/\text{V}^2)$. The type 2+3 accelerometers measured a static deflection gradient of $6.0 \text{ E-04 } \mu\text{m}/\text{V}^2$ (modelled - 4.0 E-04) and $8.0 \text{ E-05 } \mu\text{m}/\text{V}^2$ (modelled - 5.0 E-05) respectively.

The maximum mean static deflection measured was the largest for the type 1 accelerometer with $2.98 \mu\text{m} (\pm 0.4)$ at 30 V compared to types 2+3 with $1.76 \mu\text{m} (\pm 0.5)$ and $0.29 \mu\text{m} (\pm 0.06)$ respectively. This value measured for the type 1 was lower than that was envisaged at the voltage applied though it was prone to electrical shorting which was observed alongside a deflection plateau. This indicates that the lateral displacement of the proof mass was affecting the performance. A deflection plateau was not observed for type 2+3 which indicates that the spring width plays a role as expected. The smaller spring restoring force of type 1 would have allowed lateral displacement to occur more easily for an asymmetric structure which was shown by the empirical data. Ideally, as generated by the modelled data the proof mass should deflect by $14.2 \mu\text{m}$ when 55 V is applied to the combs. The types 2+3 showed very similar performance between the empirical and modelled deflection value with voltage applied.

Future work would involve redesigning the structures so that lateral displacement does not easily occur. Perhaps if type 1 was fabricated to have a larger spring restoring force laterally with smaller comb drive finger spacing to give a larger electrostatic force that may allow larger deflections to be performed without the problem of lateral displacement.

3.6 Modal analysis of accelerometer types

A modal analysis was performed between the accelerometer types, with in-plane and out-of plane deflection measured. This allowed the mode shapes to be observed and compared to that produced by the ANSYS FEA discussed in chapter 2. The analysis was performed to observe the dynamic response of the accelerometers during sinusoidal motion. The measured resonances were compared with what was modelled by the FEA analysis prior to fabrication.

3.6.1 In-plane analysis

The accelerometer devices were placed and electrically connected onto a DIP and further mounted firmly onto a piezoelectric shaker (PZT), as previously shown in Figure 3-3. The accelerometers were firstly examined from the in-plane orientation to determine the natural resonant frequency. The comb 2 of each type was electrically driven with a source voltage of 5 V_{p-p} that was produced by the HP signal analyser. The electrostatic actuation produced structural excitation of the accelerometer that allowed the amplitude and frequency to be measured with the LDV assembly which was coupled to the signal analyser. The signal analyser was utilised in conjunction with the LDV and Zygo profiler to perform the measurements. A laser spot from the LDV was placed onto the calibration tip of the accelerometers to measure the natural resonant frequency by a non-contact method. The calibration planes were used to measure the static resonances to ensure that the signal from the calibration was that of the proof mass

3.6.1.1 Accelerometer type comparison

The empirical modal measurements of all accelerometer types was performed to determine the natural resonant frequencies. The graph in Figure 3-14 was produced by the modal analysis of the type 1 accelerometer which shows a resonant frequency peak at 0.99 KHz. The measured frequencies for type 1 were all approx. situated in the 1 KHz region, which is the value that this type was designed and modelled to be using the FEA analysis.

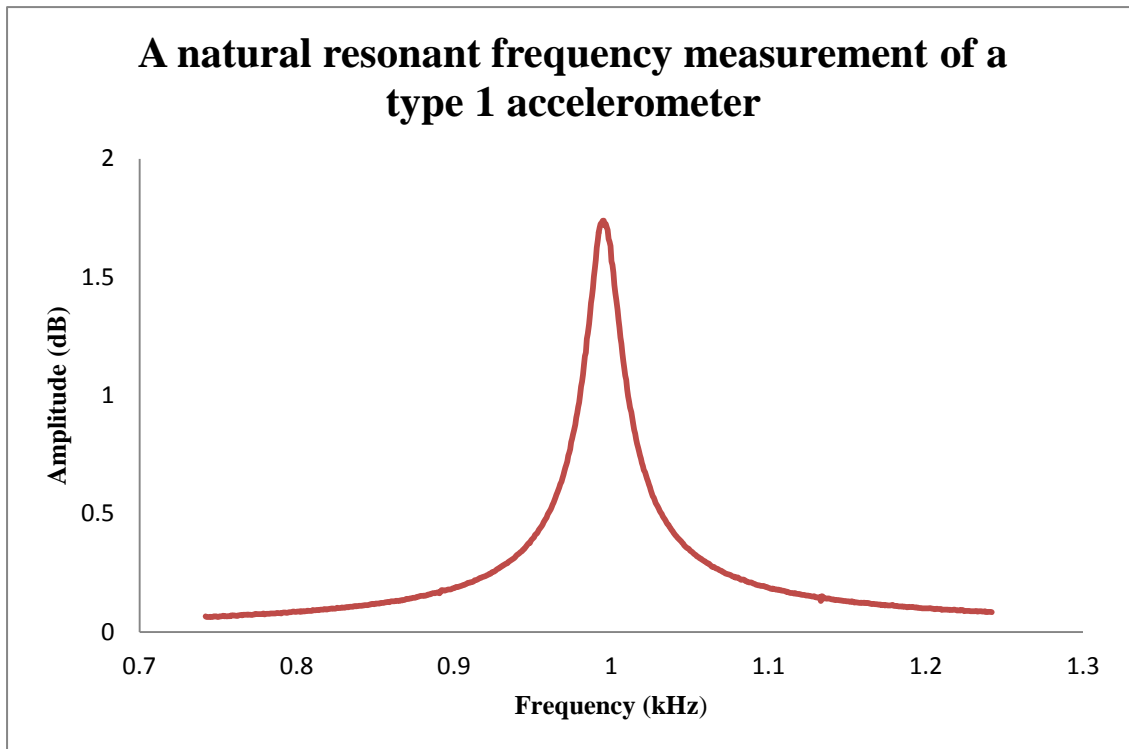


Figure 3-14: A graph showing the in-plane resonant frequency of a type 1 accelerometer.

As expected the type 2+3 were measured to have very similar natural resonant frequencies, this was expected due to having a common spring restoring force. The type 2 accelerometer was measured to have a mean frequency of 3.35 KHz and the type 3 at 3.41 KHz as displayed in Table 3-4 which shows a comparison of all types.

Type (n=3)	Mean average natural frequency (KHz)	Quality factor
1	1.02 (± 0.07)	30
2	3.35 (± 0.04)	83
3	3.41 (± 0.08)	111

Table 3-4: A comparison of the in-plane mean modal frequencies measured for all accelerometer types.

The difference of the Q factor values that were obtained for the accelerometer types could be explained by viscous damping caused by air between the comb teeth and thermoelastic friction caused by the spring dimensions.

3.6.2 Out-of-plane analysis of type 1 accelerometer

The LDV apparatus was employed to measure the resonant frequencies and magnitude of a type 1 accelerometer at specific data point locations on the surface in the out-of-plane orientation. The accelerometer was resonated by a PZT shaker driven at 5 Vp-p. A LDV laser spot was positioned to take separate measurements from points 1-12 and Z as shown in Figure 3-15. This was performed to determine the actual structural displacement for each mode shape, the data collected was integrated into Star Lab modal analysis software to visualise the mode shape by producing an animation of the structural motion.

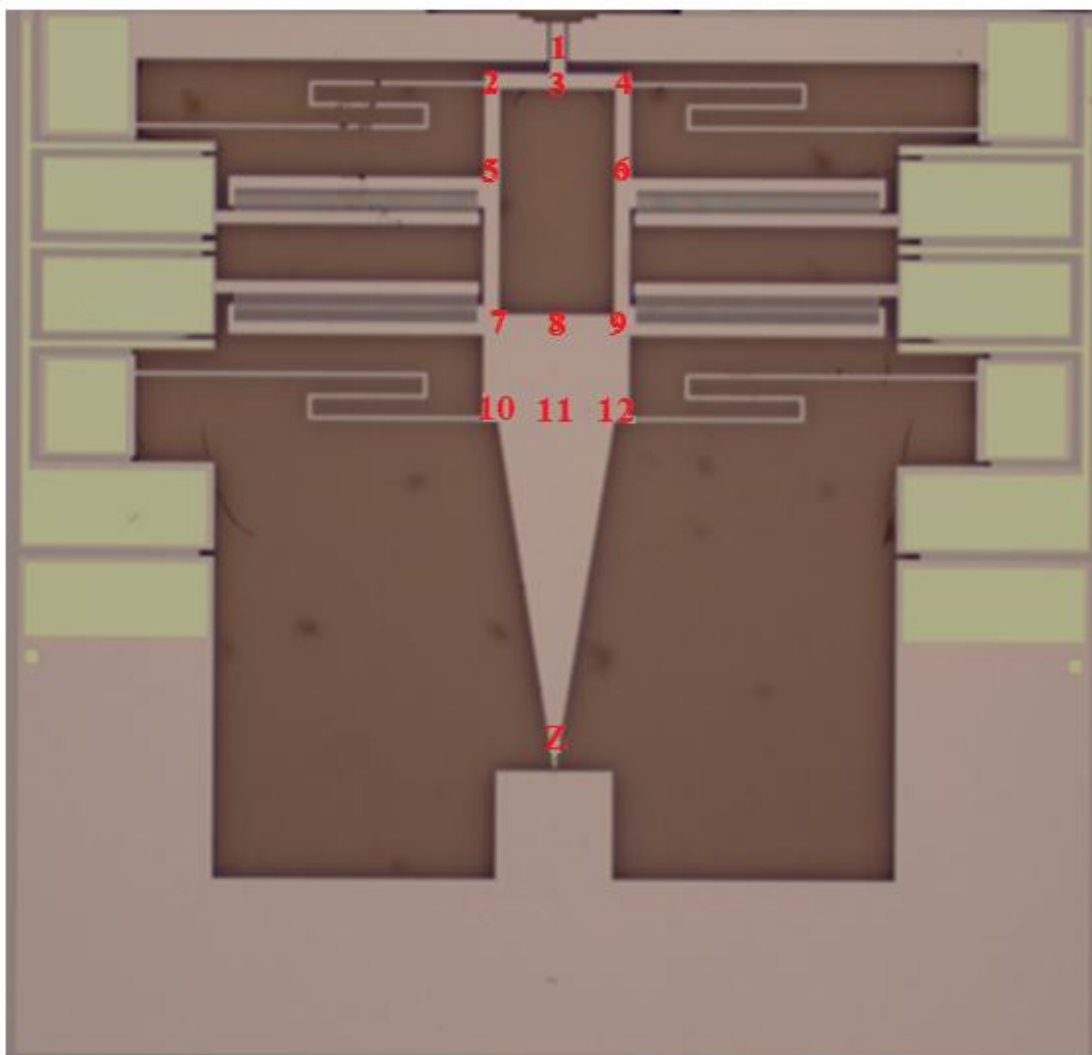


Figure 3-15: The positions where the laser spot was focused for the out-of-plane modal frequency analysis.

The investigation allowed six mode shape frequencies to be measured with the LDV assembly at the designated locations of the accelerometer in the out-of-plane orientation. The data in Table 3-5 below shows the frequencies of the six mode shapes measured, ranging from 2.44 KHz to 60.05 KHz.

Mode	Frequency (KHz)
1	2.44
2	3.06
3	18.07
4	20.79
5	27.13
6	60.05

Table 3-5: The mode frequencies for measured out of plane deflection for the type 1 accelerometers.

The frequencies of mode 1 and 2 being in agreement with the out-of-plane simulations that were generated in the FEA analysis discussed in chapter 2. The data that was collected using the HP signal analyser was recorded to allow the integration into the Star Lab software which is discussed in the next section.

3.7 Star lab software modelling

The post modal analysis 'Star Lab' software operating on a Windows 3.1 personal computer was employed to analyse the mode shapes of the type 1 accelerometer in the out-of-plane orientation. The data that was collected during the measurement process was converted into the .uff format and imported into the software. The data consisted of measurements performed at the specific data point locations and the particular frequencies measured. The geometry of the accelerometer was produced in the software by pin pointing the data point locations and connecting them to form the structure. The software allowed a visual animation to be produced that could be programmed to illustrate the specific motion of the different mode shapes recorded.

The first mode shape that was measured at 2.44 KHz at points 1-2 + Z for the accelerometer is illustrated in Figure 3-16. The animation of the mode shape at this frequency illustrates that the structure undergoes out-of-plane deflection maximally at the calibration tip and sensing gap region, giving the impression of the proof mass tipping forward.

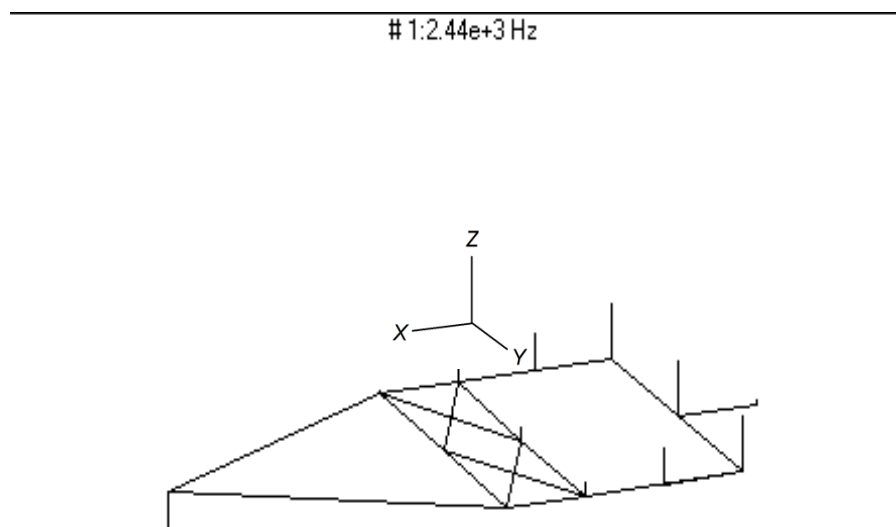


Figure 3-16: An illustration of mode shape 1 of Star lab vector animation at 2.44 KHz.

A comparison the mode shapes produced by the FEA analysis are compared with empirical data obtained in Table 3-6. It should be noted that the empirical mode shapes animated using Star lab software were for out-of-plane deflection only.

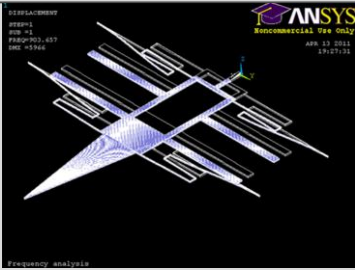
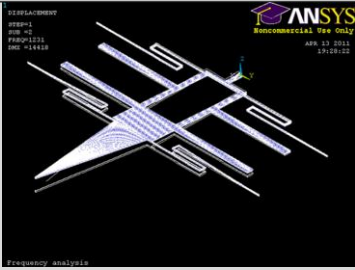
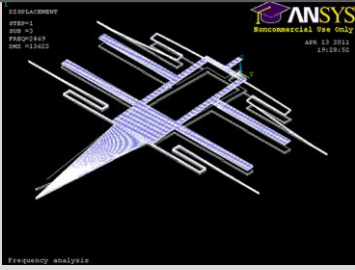

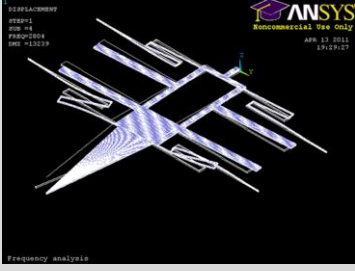
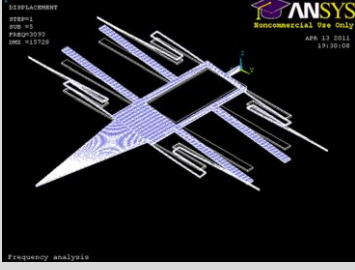
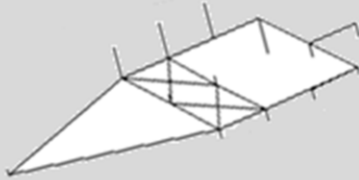
Mode	FEA frequency (KHz)	FEA model	Empirically measured
1	0.9		n/a (matched in-plane, see section 3.6.1)
2	1.2		Not detected by Piezo-actuation.
3	2.4		
4	2.8		n/a
5	3.0		

Table 3-6: The mode shapes of FEA modelled and an actual modeshape of a type 1 accelerometer.

3.7.1 Comparison of the mode shapes with FEA

This section discusses the comparison of the mode shape animations that were generated for the type 1 accelerometer in the out-of-plane orientation using FEA and animated from real measurements using Star Lab software. The information in Table 3-6 presents the frequencies of the modes generated by the FEA analysis compared to the matching empirical data. The mode 3 at 2.4 KHz shows a comparison between both the star Lab and FEA animation. In both images it is shown that the structures deflect out-of-plane, where the deflection of the calibration tip and sensing gap are of the largest amplitude. The consequences during actual operation may be the increase of the sensing gap distance which may compromise the DNA strain gauge. The mode 5 animations are similar and are in close agreement with each other between the analyses. The animation of both analyses shows the structure deflect out-of-plane and flipping sideward where the deflection of the calibration tip and sensing gap remain relatively unaffected, this may not compromise the spanned DNA.

The data in Table 3-7 shows a comparison of the in-plane frequency and the two matching out-of-plane mode frequencies that were measured. It was concluded that both the out-of-plane frequencies were in close agreement by less than 1 % between the analyses.

Matching Mode	Measured Frequency (KHz)	FEA Frequency (KHz)	Percentage Difference (%)
1	1.02	0.903	11.5
2	2.44	2.46	0.81
3	3.06	3.09	0.97

Table 3-7: A table comparing the two matching modes between the measured data and the FEA results.

3.8 Summary and Conclusions

The accelerometer types that were designed, modelled and fabricated were characterised in this chapter. The experimental data regarding the performance of static deflection between the accelerometer types were in close agreement of what was modelled prior to fabrication; however the type 1 maximum deflection was lower than that was envisaged in the design stage. Though the deflection gradients of the modelled and empirical values were in close agreement between all types which suggested the performance of type 1 was limited by the comb drive pull-in that occurred during electrostatic actuation. As expected the type 1 accelerometer showed the greatest overall performance for the application required for the application of DNA placement and stretching to realise a biological accelerometer. The in-plane natural resonant frequency between the accelerometer types was proved to be affected by the spring restoring force with the spring width, the type being at 1 KHz which was desired and in close agreement with the FEA. The out-of-plane analysis performed, being the FEA and the empirical measurements of the type 1 accelerometer mode shapes showed to be in close agreement with one another for 3 modes.

4 Chapter 4 The Chemical Immobilisation and Metallisation of Deoxyribonucleic acid

This chapter explores the ability to perform specific placement of λ -DNA onto gold substrates and chemical metallisation of the molecule to alter the electrical properties. The first section focuses on the chemical immobilisation protocols that were developed to anchor λ -DNA onto gold substrates for the purpose of specifically placing the molecule on the accelerometer sensing tips. The second section focuses on controlling the metallisation process of λ -DNA using zinc ions. The metallisation process was monitored using UV-Vis and fluorescent spectroscopy. The expectation being that the chemistries developed for the immobilisation and metallisation of λ -DNA were to be employed to construct a metallised DNA strain gauge placed within the accelerometer sensing gap

4.1 Introduction

The protocols for performing the two main objectives are discussed further in this chapter that is separated into two sections;

4.1.1 Biomolecular immobilisation and recognition

The effectiveness of employing alkanethiol chemistry to immobilise ssDNA oligonucleotides on gold substrates and the subsequent hybridisation of target DNA was determined. This was performed to develop protocols robust enough to allow the specific placement of λ -DNA in the sensing gap of the biological accelerometer. The protocols performed were monitored using surface plasmon resonance (SPR) to measure the interaction of the biomolecules.

There were many protocols that were considered to chemically immobilise λ -DNA on the gold sensing tips for positioning. As highlighted by the schematics in Figure 4-1 there was initially three options. Option A was to immobilise each complementary probe individual on each opposing sensing tip and hybridise DNA to each by base pairing. Option B was to pre-hybridise each complementary probe to the λ -DNA *in-vivo* prior to placement in the sensing gap, allowing the entire molecule to become bound by the thiol groups at the termini. Option C was to pre-hybridise one complementary probe to one end of the λ -DNA and then to immobilise the other end to surface bound probe. The λ -DNA could then be stretched across the sensing gap so that the non-surface bound end could attach by the thiol bond to the opposing sensing tip to make a DNA bridge as shown in the schematic.

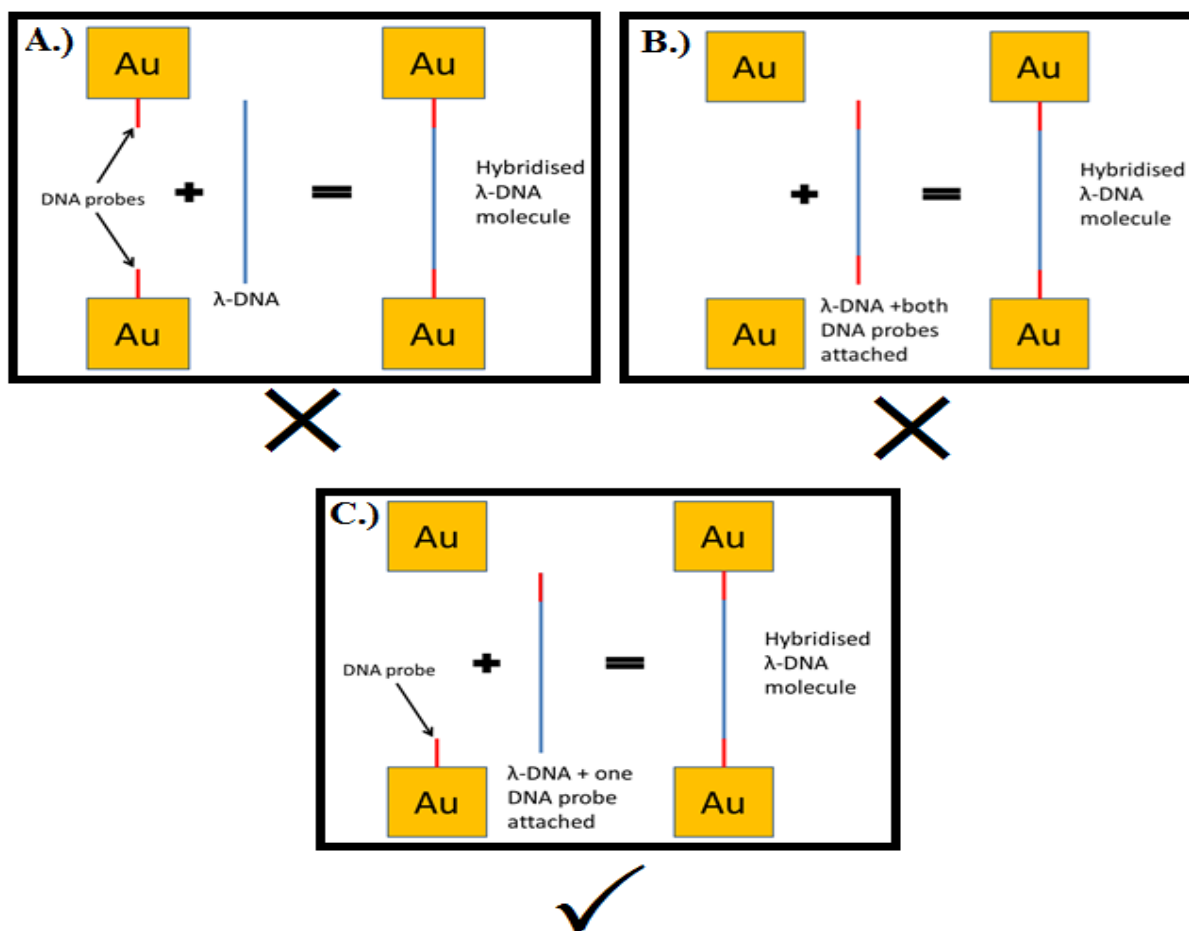


Figure 4-1: A compilation of schematics showing the possible routes of chemical immobilisation

The protocol that was chosen to be the most effective for this research was option C as it was not possible to specifically immobilise individual probes on the sensing tip using the dipping method on the accelerometers. The dipping method that is described further in chapter 5 was employed to place the sensing tips in the deposition solution whilst protecting the actuating features and gold electrical bond pads of the accelerometer. Option B was disregarded as it was deemed too problematic to position the DNA across the sensing gap that was chemically anchored to both sensing tips.

4.1.2 The chemical formation of M-DNA from pristine DNA templates

The chemical metallisation of λ-DNA was performed using a zinc compound as a source of zinc ions that will associate with the molecule to form M-DNA. The degree of metallisation was measured using both UV-Vis and fluorescent spectrometry to monitor the change of the DNA absorbance peak maxima and the fluorescent property of YOYO-1 labelled DNA with metal ion concentration respectively.

4.2 DNA biomolecular recognition

The chemical immobilisation of ssDNA oligonucleotides onto gold substrates and the further association of λ -DNA was monitored using an SPR Biacore biosensing system. The commonly used Biacore system is employed to monitor ligand-analyte interactions on a planar surface in real time that collects accurate information on the association concentration and kinetics. Generally biosensors use electrical, thermal or optical signals to determine ligand-analyte association on a capture layer.

4.2.1 Capture based biomolecular recognition events

In capture based sensing, a recognition interface will consist of highly specific capture molecules immobilised onto the surface of a substrate, as discussed in chapter 1 for DNA hybridisation. The capture molecules (ligands) may be immobilised onto the substrate using physical entrapment, microencapsulation, or physical chemisorption like thiols. The capture layer may allow the target molecule (analyte) to be captured specifically through a biorecognition event such as Watson and Crick base pairing or antibody-antigen association. The image in Figure 4-2 shows a capture layer with antigen specific antibody receptors chemically anchored to the surface that allows an association event to occur while a sensing signal will be produced that is converted by a transducing element into a proportional readable signal. Depending on the application different transducing methods can be used such as the change of the; pH, electrical properties, temperature and natural resonance. Commercial instruments that are used in laboratories around the world to monitor ligand-analyte associations are generally based on electrical impedance spectroscopy (EIS), the resonant properties of an oscillator like quartz crystal microbalance (QCM) and the SPR Biacore system that relies on an optical signal.

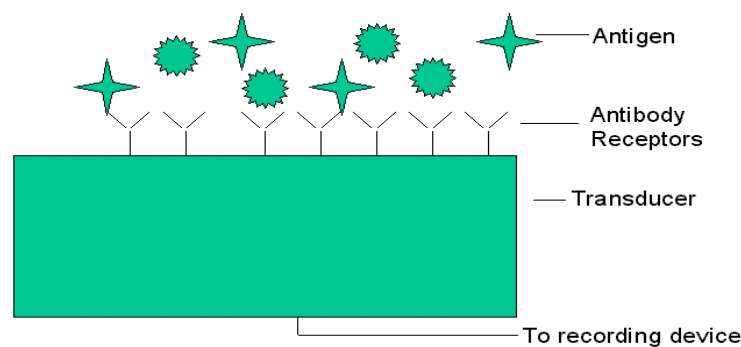


Figure 4-2: An immunosensor capture layer with antigen receptors immobilised at the surface allowing capture of specific antigen taken from (Kumar 2000).

4.2.2 Surface Plasmon Resonance Biacore System

The surface plasmon resonance Biacore system is an example of an affinity optical biosensor which consists of an optical transducer and a biomolecular recognition element (BRE). The transducer consists of a thin metal film that detects surface plasmon-polaritons (SPP), the most commonly used metal being gold. The biomolecular association of the analyte to the capture ligand on the thin metal film causes a change of the refractive index of polarised light which results in the change of the propagation constant of the SPP (Liedberg, Nylander et al. 1983). The value of the SPP propagation constant is determined by measuring change in intensity of reflected light at multiple wavelengths (Otto 1968). Measuring the change of the SPP propagation constant allows the amount of analyte associated on the capture layer to be calculated. The calculation is performed using a PC software package that displays graphical information regarding the change of response units (RU). The variation of RU is directly proportional to the molecular mass present on the metal surface.

If the SPR instrument includes intensity modulation, the SPP is excited by shining a beam of monochromatic light with a fixed angle of incidence under the metal film; where the change of the propagation constant is measured by the change of intensity reflected light at multiple wavelengths. A prism coupler is used to excite the plasmons by attenuated total reflection (ATR) and the change of SPP can be measured to detect analytes on the capture layer. A flow channel is used to pass the solute over the capture layer at a specified flow rate to initiate biomolecular interaction. The image in Figure 4-3 displays an illustration of the components an SPR detection system, showing the physical components and graphical information displayed in the sensorgram highlighting the amount of association. The sensorgram displays the change of RU with time at a given flow rate, when molecules are deposited on the metal surface the sensorgram will show an increase of RU.

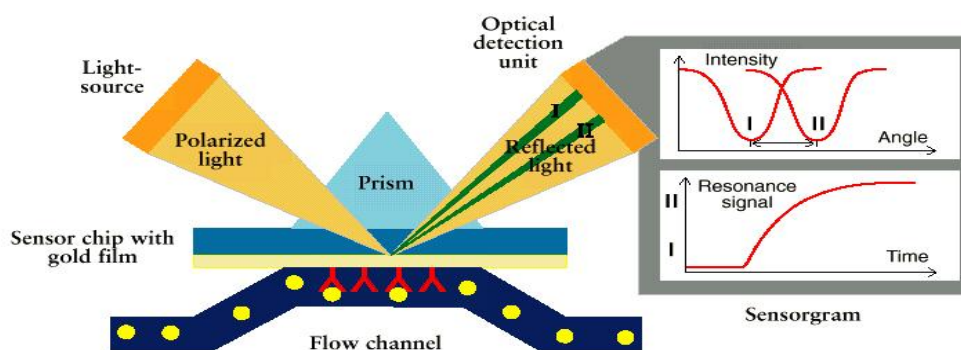


Figure 4-3: A Biacore biosensor system illustrating the flow channel and optical detection. Picture from Biacore online catalogue.

The Biacore system is used in laboratories worldwide to monitor ligand analyte interactions. An example of a use being the generation of a selective capture layer on the surface on a metal film such as gold. The analyte solution that is to associate with the capture layer is injected into a microfluidic flow cell that is run over the surface for a certain period of time at a specific flow rate. The change of RU with time is observed with time during the injection as analyte is associated giving an increase of RU. Once the capture layer is saturated the change of RU will begin to plateau as observed in the sensorgram in Figure 4-4. When the injection ends running buffer is returned to the sensor surface, effectively removing analyte from the system with the exception of tightly bound material. The process of regeneration can be employed to remove all analyte from the sensor surface to form a layer similar previous to analyte association, hence returning to the same RU value as illustrated in the sensorgram in Figure 4-4.

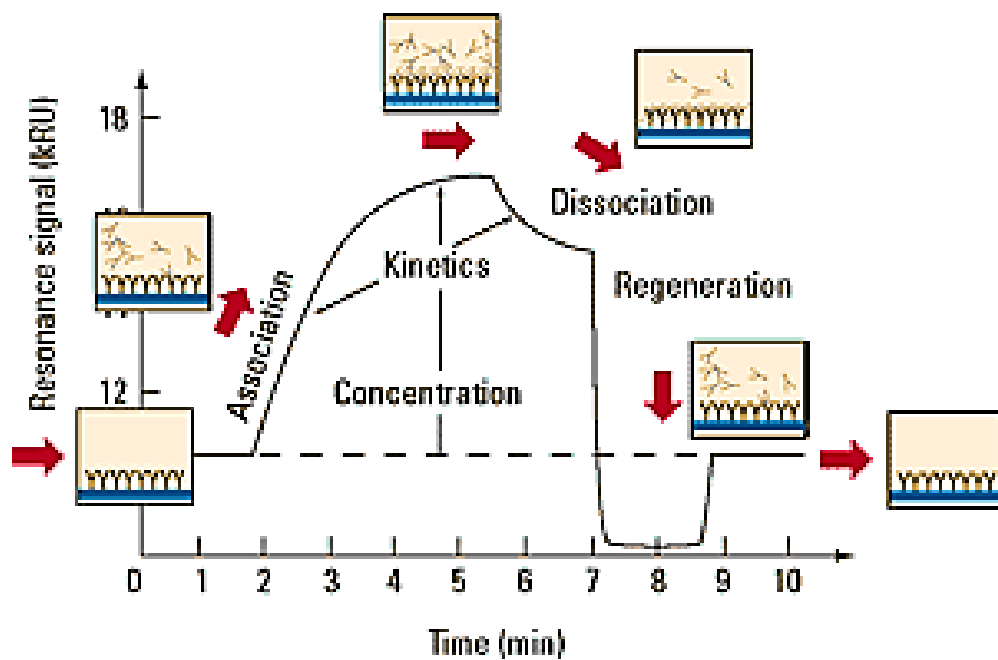


Figure 4-4: An example of a sensorgram that shows selective association, dissociation and regeneration.

The concentration of analyte solution will be initially determined before injection into the Biacore system by spectrophotometric analysis which is discussed in the next section.

4.3 Ultraviolet-Visible light and fluorescent spectroscopy

This section discusses Ultraviolet-Visible (UV-Vis) light spectroscopy, though this is a basic technique it is discussed to inform readers of varying expertise as this is a multidisciplinary project. UV light spectroscopy is a technique commonly performed to determine the concentration of analyte in a solution in a quantifiable manner. The concentration can be calculated by measuring the optical absorption properties at a known wavelength by employing the 'Beer Lambert law' if the extinction coefficient value is known for the analyte. The technique is commonly used to determine the concentration of Proteins, RNA or DNA in a liquid suspension as the wavelengths of the absorption peak maxima are well characterised.

4.3.1 The Beer Lambert law and the Optical density of DNA

The Beer Lambert law is the relationship between the absorbance of light through a sample containing the molecules and the concentration within the pathlength. The optical absorption co-efficient of the material, α , with the transmission of light, I , through the sample pathlength, l , will allow the calculation of the extinction coefficient, ϵ or the concentration, c . The image in Figure 4-5 shows a light beam shining through a cuvette with a known pathlength, I_0 being the light before absorption by the sample and I_1 after.

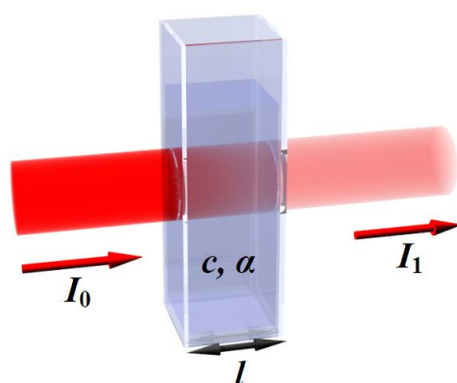


Figure 4-5: Light passing through a Cuvette containing a liquid sample.

A solution of pristine DNA in water has an absorbance peak maxima at 260 nm (A_{260}) where by observing the optical density at both 260 nm and 280 nm a measure of purity can be calculated. A relatively pure DNA sample will have a 260/280 nm peak maxima ratio of 1.8, where aromatic proteins absorb light at 280 nm, if present in the DNA sample the ratio will be below 1.8. Commonly the procedure is performed to determine the concentration of DNA in a cuvette with a known pathlength. An optical density value of 1 for a dsDNA solution in a

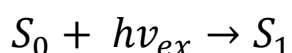
cuvette with a pathlength of 1 cm will have a concentration of 50 µg/ml. A fluorophore that is associated with DNA will show emission maxima peaks also at a known wavelength.

4.3.2 The properties of fluorophores and the use for biological applications

Fluorescence is commonly used for biological applications where a fluorophore will be associated with a chosen biological molecule to allow real time observation of the sample utilising fluorescent microscopy. The use of fluorescence is commonly used by biologists for many applications, examples such as to view histological stains for molecular detection, to observe protein-protein and DNA-protein interactions and to view DNA in real time on a sensor surface. The DNA molecule can be modified with an abundance of commercially available fluorescent dyes that have ranging excitation and emission wavelengths. The phenomenon of fluorescence is caused due to the excitation of a fluorophore by an orbital electron which then reduces to its original ground state, causing the emission of a photon.

4.3.2.1 Fluorophore Excitation

The excitation of a fluorophore can be produced by an external light source at the specific excitation wavelength. The excitation of a fluorophore at the correct wavelength will cause the emission of light at the emission wavelength. The information in equation 4-1 describes the optical excitation and energy states involved for inducing fluorescence where S_0 is the fluorophore ground state, $h\nu$ is the photon energy, h is the Plancks constant, ν is the frequency of light and S_1 being the excited state.



[4-1]

As can be interpreted, the natural ground state of a fluorophore absorbs energy from light at the preferred wavelength, allowing a higher energy state. The illustration in Figure 4-6 illustrates the excitation and emission from the change of energy of the fluorophore from S_0 back to S_1 that is described in equation 4-2.

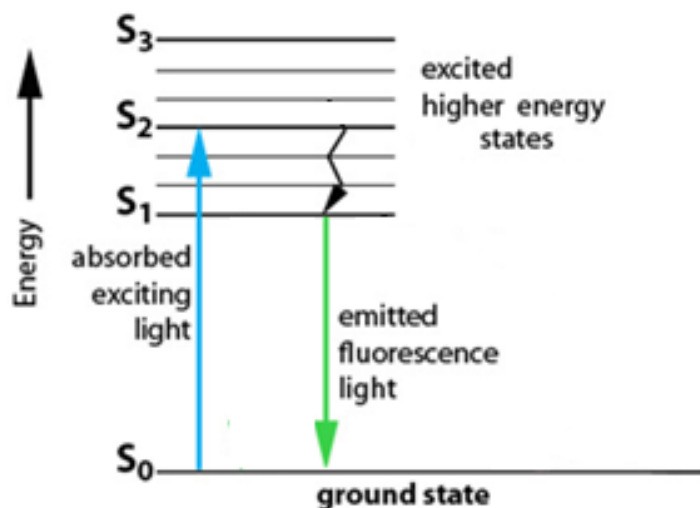
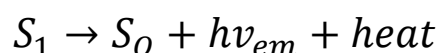


Figure 4-6: The change of energy of a fluorophore and the subsequent fluorescent emission when returning to the ground state.

4.3.2.2 Fluorophore Emission

The emission of light at the emission wavelength by optical excitation is described in equation 4-2, where the excited fluorophore S_1 , returns to the ground state by competing pathways such as the dissipation of heat (*heat*) and the emission of a photon. The loss of energy of the photon creates the fluorescent emission ($h\nu_{em}$) of light that has lower energy with a longer wavelength than the excitation wavelength.



[4-2]

The wavelength difference of the peak maxima for the excitation and emission of a fluorophore is termed the 'Stokes shift'. The excitation and emission spectrum of a fluorophore is shown in Figure 4-7 that indicates the Stokes shift between the two peaks. The characteristics between the spectrums of different fluorophores may have sharp peaks as they excite/emit over a narrow wavelength or have broad peaks over larger wavelengths.

The full width half maximum value (FWHM) of the peak is the spectral distance at 50 % of the optical intensity; this value can be used to describe the peak characteristic accurately.

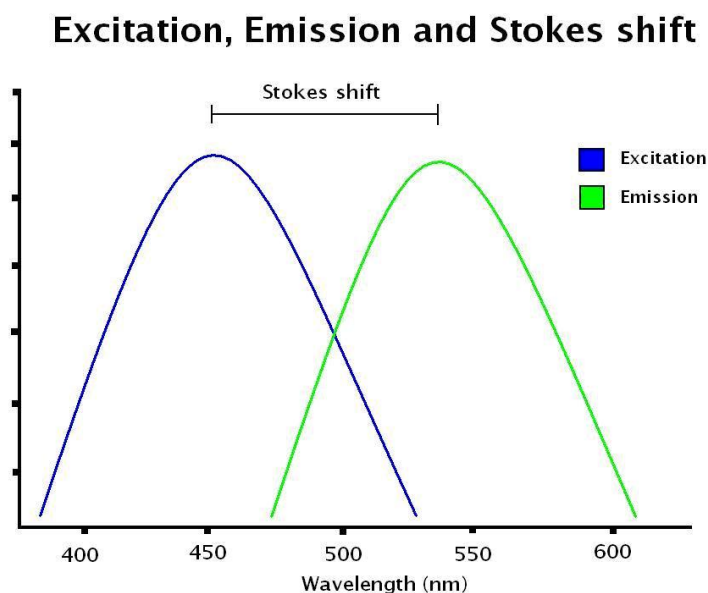


Figure 4-7: A graph displaying the excitation and emission spectrum peaks of a fluorophore highlighting the resulting Stokes shift.

4.3.2.3 Cyanine dyes and YOYO-1 iodide

Cyanine dyes typically have an emission maxima ranging from 500-750 nm with large extinction co-efficients. The co-efficient being an indication of how strongly the fluorophore absorbs light, where the cyanine dye YOYO-1 iodide (YOYO-1 herein) has a high association constant and is considered to be a premium grade DNA specific fluorescent dye. The dye chemical structure ($C_{49}H_{58}I_4N_6O_2$) being positively charged allows initial attachment to the polyanionic structure of the DNA molecule, once bound to the backbone the dye bis-intercalates into the grooves between the base pairs which was determined using NMR spectroscopy (Johansen and Jacobsen 1998). The chemical structure is displayed in Figure 4-8.

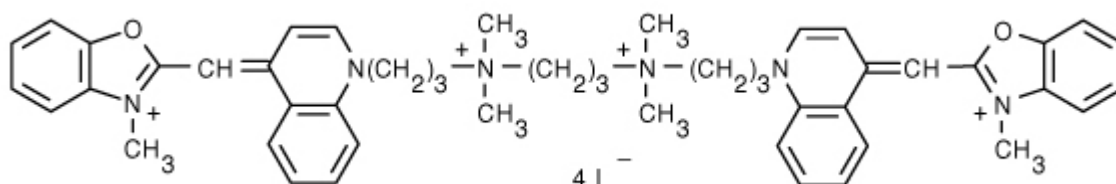


Figure 4-8: The chemical structure of the YOYO-1 iodide DNA specific dye.

The YOYO-1 dye exhibits excitation and emission in the FITC range with the peak maxima of excitation/emission at 491/509 nm and a molar extinction coefficient of $98\,000\text{ M}^{-1}\text{ cm}^{-1}$. The bis-intercalation of YOYO-1 into the backbone of dsDNA has been suggested to increase the contour length of the molecule by approx. 30 % (Günther, Mertig et al. 2010; Kim, Kim et al. 2011). The use of YOYO-1 has been reported to have been used for single molecule detection of biological molecules (Bennink, Schärer et al. 1999; van 't Hoff, Reuter et al. 2009; Günther, Mertig et al. 2010). It has been commonly employed for the preparation of DNA nanowires, as being specific to DNA with a large signal to noise ratio. This has allowed DNA nanowires to be imaged on a variety of surfaces using an epifluorescent microscope allowing the investigator to confirm that DNA has specifically spanned a set distance forming a nanowire.

4.4 Methods

4.4.1 Surface Plasmon Resonance and DNA Immobilisation Protocols

The DNA immobilisation protocols were assessed using SPR detection, the protocols are presented in this section

4.4.1.1 The preparation of λ -DNA

The stock lyophilised and methylated λ -DNA (Cat.no. D9768) was purchased from Sigma-Aldrich with an amount of 10 units. One A_{260} unit is equivalent to approximately 50 μg of DNA hence being 500 μg . The source of the λ -DNA being Escherichia coli W3110 of strain $\lambda\text{c1857 Sam 7}$ and the DNA molecular weight being 31.5×10^3 kDa (48,502 bp). The termini of linearised λ -DNA contains a 3' and a 5' end that have 12 base single stranded overhangs that are complementary to one another, this area is known as the cos or cohesive site. As discussed in chapter 1 this complementary region can be used to manipulate the λ -DNA molecule to allow it to be used as a generic material rather than genomic. The entire 10 units of the stock λ -DNA was mixed into 500 μl of autoclaved and vacuum filtered (0.22 μm) hybridisation buffer (10 mM Tris-HCl, 100 mM NaCl, 1 mM Ethylenediaminetetraacetic acid), where spectrophotometer analysis determined the concentration to be 1 $\mu\text{g}/\mu\text{l}$. The λ -DNA after being placed in the deposition solution underwent a dissociation protocol to ensure the molecules were linearised with cohesive ends that are available for hybridisation. This involved placing 50 μg (50 μl) λ -DNA from the stock solution into a 1.5ml eppendorf tube which was placed into a water bath with a constant temperature of 65 $^{\circ}\text{C}$ for 15 minutes. The DNA solution was further diluted in the exact hybridisation buffer to a concentration that was required, for the Biacore analysis being 100 $\text{ng}/\mu\text{l}$.

4.4.1.2 Preparation thiolated DNA Oligonucleotides complementary to λ -DNA

The two oligonucleotide probes that were complementary to the linearised cohesive ends of λ -DNA were synthesised by MWG Munich, Germany. The two oligonucleotides were termed probe A and probe B herein for ease of identification. The single stranded base sequence of 'probe A' was 5' **PO4-AGGTCGCCGCCCTTTT(CH₂)₃-SH** 3' and 'probe B' being 5' **PO4-GGGCGGCGACCTTTTT(CH₂)₃-SH** 3'. As can be deduced the oligonucleotide probes were both phosphorylated and thiolated at the 5' and 3' termini respectively. The specifications of the oligonucleotides are listed in Table 4.2.

Probe	Stock Amount (Concentration in 1ml)	T _m °C	GC content	Molecular Weight	Modification
A	78 μmole (78 pmol/μl)	54.3	62.5	4,977 g/mol	3'thiol modifier C3 5' P04
B	90 μmole (90 pmol/μl)	54.3	62.5	5,057 g/mol	3'thiol modifier C3 5' P04

Table 4.2: The specifications of the oligonucleotide probes used for the hybridisation protocols.

The oligonucleotide probes were purchased in lyophilised form. The oligonucleotide probe A was suspended into 1 ml of autoclaved and vacuum filtered 1 M phosphate buffer pH 7.4 and probe B within 1 ml of hybridisation buffer giving the concentrations displayed in Table 4.2.

4.4.1.3 Biacore DNA SAM immobilisation validation methods

A Biacore 3000 system was employed to confirm the chemisorption of the thiolated probes to the gold surface and the subsequent hybridisation of λ-DNA. The Biacore instrument had firstly passed the manufacturers recommended system check to ensure that it was working optimally. A running buffer of autoclaved and vacuum filtered 1 M phosphate buffer pH 7.4 was used and a standard Biacore commercial gold sensor chip was inserted into the optical detection unit.

The 5 μl/min flow rate of the 1 M phosphate pH 7.4 running buffer was run for 5 minutes before the addition of probe to allow a steady baseline reading, then a 1 μM probe A solution was injected for 30 minutes. To remove non-specific/loosely bound material an additional step was performed to ensure covalently bound material was only present. An injection of sodium dodecyl sulphate (SDS) was undertaken; SDS being a detergent which is used to disrupt non covalent bonds. A 0.01 % SDS solution was injected over the gold sensor surface for 10 minutes twice for a single. The removal of non-specifically bound probe could not be observed in real time until once back in the running buffer as the SDS solution has greatly different refractive index to the running buffer. After the completion of the two injection steps of the SDS solution the running buffer flowed over the sensor chip once more allowing the true change of RU to be observed. After the oligonucleotide probe immobilisation was

complete a β -mercaptoethanol (MCE) ‘backfilling’ step was performed, a 1 mM MCE solution was injected over the sensor surface for 30 minutes.

4.4.2 The λ -DNA hybridisation protocols

Once the oligonucleotide probe A and MCE had been chemically immobilised onto the gold surface as a capture layer, the hybridisation steps were performed to allow the specific interaction of λ -DNA. A 150 μ l volume of λ -DNA in hybridisation buffer with a concentration of 100 ng/ μ l was injected over the gold sensor surface for 30 minutes. Once the injection had taken place the running buffer was once again run through the flow cell allowing the observation of the change of RU. An investigation was performed to ensure that λ -DNA was associating to the surface by complementary hybridisation probe A and not by non-specific interaction. The terminal sticky ends of the λ -DNA were modified to investigate this matter.

4.4.2.1 Complementary DNA Control

A control step was performed to confirm that the DNA molecules became bound to the surface by sequence specific hybridisation and not by any other scenario. A 1 μ M solution of non-complementary ssDNA (known as DNA-Z herein) in hybridisation buffer with the sequence 5’ **TACATAGAGATGGGAATCCAT** 3’ was injected over the sensor surface for 10 minutes. Thereafter for a comparison, a 1 μ M complementary λ -DNA solution was flowed over the sensor surface for 30 minutes while the RU change was recorded on a single sensorgram for both injections.

4.4.2.2 The λ -DNA pre-hybridised to probe B method

The λ -DNA molecule was pre-hybridised with the oligonucleotide probe B (λ -DNA-B herein) *in vitro* prior to the Biacore hybridisation analysis. Theoretically this will reduce the possibility of the λ -DNA molecule undergoing circularisation due to hybridisation of the complementary regions. This was performed in this study for two reasons; first to see if the efficiency of hybridisation increased and secondly for the application of specific placement onto the gold sensing tips of the accelerometer. This method was developed to allow DNA positioning between the sensing gap or to be performed with greater ease because the thiolated probe B is initially associated to the λ -DNA molecule. This allows the hybridisation of λ -DNA-B to probe A on one sensing tip and then to be stretched to the opposing sensing tip and to become attached by the free thiol bond rather than by a secondary hybridisation event. This removes the process of immobilising the oligonucleotide probes separately on the

opposing sensing tips and also eliminates the possibility of cross contamination of the probes that may happen during the sensitive dipping immobilisation process.

A threefold excess of oligonucleotide probe B in hybridisation buffer was added to 50 μ l stock λ -DNA solution was placed in eppendorf tube and placed in a water bath at 37 °C for two hours, the solution was left to cool overnight. This was to allow the hybridisation of probe B with the λ -DNA to form a single molecule with only one available termini for hybridisation, being complementary to probe A. Once this procedure was completed the λ -DNA was purified from the reaction mixture by using size exclusion chromatography (SEC). The application of SEC allows the separation of molecules by their size, ideal for separating large size DNA molecules from short oligonucleotides in a solution. A Bio-Rad Micro Bio-Spin P-30 size exclusion column was employed in this study using the manufacturer's guidelines. The DNA containing solution was pipetted onto the top of the column gel support and centrifuged for 4 minutes at 1,300 r.p.m to separate the λ -DNA from the excess probe B contained in the solution. After the spinning was finished the expelled solution was collected as it will contain the large size λ -DNA where the free probe B molecules will be retained in the gel column. The next step was to perform a ligation to covalently couple the oligonucleotide to the λ -DNA template.

The enzyme used for the ligation being T4 DNA ligase that works optimally in ligation buffer (250 mM Tris-HCl, 50 mM MgCl₂, 5 mM ATP, 5 mM DTT). Generally, the ligase enzyme is described and sold by Weiss unit concentration where 0.01 units is stated to ligate 95 % of 1 μ g of λ -DNA Hind III fragments (8 fragments) at 16 °C in 20 minutes. In this study 10 Weiss units of T4 DNA ligase (Purchased from Invitrogen, Cat. No. 15224-041) were used to ligate 50 μ g λ -DNA, being an excess amount to ensure a ligation with high efficiency. To perform a ligation with 50 μ l probe B hybridised λ -DNA (1 μ g/ μ l), 2 μ l of ligase (5 units/ μ l) and 5.2 μ l of x10 ligation buffer was added to the solution in an eppendorf tube and mixed (57.2 μ l final volume). The ligation was performed at room temperature overnight to ensure that the λ -DNA-B molecule would be associated by a permanent covalent bond. The DNA molecules were separated from the ligase buffer solution using SEC into hybridisation buffer and then heated to 80 °C for 15 minutes to deactivate any ligase that may be present in the solution. The solution was then further diluted to a working concentration of 100 ng/ μ l for the Biacore hybridisation analysis.

4.4.3 The closed ligated λ -DNA method

A circular λ -DNA was formed by self-hybridisation and permanent ligation to act as a negative control that should not associate specifically with the capture layer, denoted λ -DNA-C herein. A 50 μ l (1 μ g/ μ l) amount of stock solution of λ -DNA in hybridisation buffer was placed into an eppendorf tube and placed in a water bath overnight where the temperature was maintained at 37 °C. Once the hybridisation was complete the DNA solution underwent SEC into ligation buffer. The ligation was performed the same as in the previous section at room temperature overnight. Once the ligation was completed, SEC was employed again to remove the DNA from the enzyme solution and to place in hybridisation buffer by the buffer exchange process.

4.4.4 The DNA ligation validation method

An experiment was performed to prove that λ -DNA could be ligated on the surface once it was hybridised. This was performed to make a more robust DNA molecule for the future application of stretching in the accelerometer sensing gap. The probe A layer and λ -DNA hybridisation was performed on the surface using the methods discussed previously. Once the λ -DNA was hybridised on the surface of a Biacore sensor chip, a 200 μ l solution of 10 Weiss units of T4 DNA Ligase in ligation buffer was eluted onto the surface for 16 hours in a humid environment. After the ligation was complete the chip was placed into the Biacore instrument a 1 M phosphate running buffer with a 5 μ l/min flow rate was flowed. An injection of a pH 13 buffer solution (0.2 M KCl and 0.2 M NaOH) was undertaken for 30 minutes over the sensor surface. The addition of a high pH buffer solution was performed to determine if the ligation was effective as the pH should remove non-ligated DNA by dissociation of the hydrogen bonds of the hybridised complementary molecules (λ -DNA and probe A). When the injection was complete the change of RU on the sensorgram was observed to determine if DNA material was removed. As a comparison a pH 13 buffer solution injection was performed on a surface containing non-ligated DNA and the change of RU was observed.

4.4.5 DNA Metallisation protocols

The DNA metallisation protocols performed were monitored using UV-Vis spectroscopy and fluorimetry that are described in this section. A Tecan infinite M200 instrument that contains a fluorimeter and UV-Vis spectrometer was employed to measure the A_{260} peak maxima of M-DNA and the properties of the metallised and non-metallised YOYO-1 labelled DNA fluorescent emission.

4.4.5.1 UV-Vis spectroscopy of M-DNA protocols

The determination of the formation of M-DNA was monitored by observing the A_{260} peak shift of DNA. First Calf thymus DNA (CT DNA) was employed in an initial study to find the optimum protocols for the metallisation of DNA and then secondly performed with λ -DNA once the protocols were finalised. The reason for using CT DNA being that it is cheaply available in large quantities and of a large size like λ -DNA, reducing the costs that would be involved if λ -DNA was to be initially used find the optimum conditions.

The CT DNA was purchased from Sigma Aldrich (Cat. No. D4522) in a lyophilised form which was suspended in a 100 mM Trizma buffer (Tris. herein) pH 8.5 to a stock concentration of 1 $\mu\text{g}/\mu\text{l}$. A 50 ml solution of 20 mM in Tris buffer stock concentration of metallisation solution was made to be used to be diluted to the working concentration in Tris buffer. A stock metallisation solution was made in 100 mM Tris and zinc Perchlorate ($(\text{ZnClO}_4)_2$) to be used for the metallisation of the DNA using zinc ions. The zinc stock solution was used to make 5 ml of each working concentration desired (1-5 mM) that were further adjusted to have a pH of 8.5. Immediately once that the metallisation solutions were made they were placed in an eppendorf tube with CT DNA to give a final concentration of 140 $\text{ng}/\mu\text{l}$ in 300 μl and mixed thoroughly. The solutions were left at room temperature overnight to perform the metallisation. Once the metallisation protocol was performed the samples underwent SEC into a 100 mM Tris pH 8.5 solution and were ready for UV-Vis spectroscopy analysis. This procedure was performed for the preparation of $(\text{ZnClO}_4)_2$ M-DNA.

As a control pristine and EDTA modified DNA were prepared and the A_{260} peak maxima observed. The pristine control being stock DNA that was diluted to the working concentration of 100 $\text{ng}/\mu\text{l}$ and the optical absorbance properties observed. The EDTA control was used to validate that the change of peak maxima was caused by the association of zinc ions with the

DNA. The EDTA compound being a chelating agent that allows it to sequester metal ions in a solution, hence the M-DNA was treated with EDTA to convert it back to the pristine form. Once the M-DNA protocol was for this instance the M-DNA was placed into 100 mM Tris, 10 mM EDTA pH 8.5 by SEC.

A Greiner UV-Star 96 well plate purchased from Sigma Aldrich (Cat. No. M3812) that was suitable for DNA analysis and UV clear meaning that there was no background interference in the UV range. An optical absorbance measurement was undertaken for the samples between the wavelengths of 240-320 nm. The metallisation protocols were performed exactly for the DNA variations used (CT DNA and λ -DNA).

4.4.5.2 Fluorescent spectroscopy and M-DNA protocols

The fluorescent properties of YOYO-1 labelled λ -DNA (YOYO-1/DNA) were monitored to study the change of the fluorescent properties with the degree of metallisation similarly to the UV-Vis spectroscopy study. The optimum metallisation procedure had already been investigated therefore the protocols were performed using only exclusively λ -DNA. The exact zinc metal ion solutions were used from the previous UV-Vis analysis, the only difference being that DNA was labelled with the fluorophore YOYO-1 beforehand and the emission peak observed.

A 50 μ l volume of λ -DNA (1 μ g/ μ l) from the stock solution was placed into an eppendorf tube. The λ -DNA was then labelled with the cyanine dye YOYO-1 using a 5:1 ratio (DNA:Dye) regarding the amount of DNA (μ g) that was present. Amount of YOYO-1 dye to be used was calculated using the following in equation 4-3.

$$YoYo \text{ amount to be used (5:1)} = \frac{\left(\frac{\text{Amount of DNA}}{\text{MW of DNA}} \times \text{MW OF YOYO} - 1 \text{ dye}\right)}{5}$$

[4-3]

The calculated amount and volume of YOYO-1 solution (1.25 $\mu\text{g}/\mu\text{l}$) was then added to the λ -DNA solution in Tris buffer accordingly and left overnight at room temperature, the eppendorf tube was wrapped in foil so that natural light would not photobleach the dye. The labelled λ -DNA was separated from the excess dye by SEC using a Bio-Rad P-30 column and eluted into a Tris buffer pH 8.5 solution. The free non-associated dye was therefore removed leaving only YOYO-1/DNA in the 100 mM Tris buffer pH 8.5 solution.

The YOYO-1/DNA was placed in individual eppendorf tubes with the ranging concentrations of zinc metallisation solution to give a volume of 300 μl with a DNA concentration of 10 $\text{ng}/\mu\text{l}$; the solutions having a range of concentrations (1-5 mM). The solutions were left overnight to allow the zinc ions to associate with the DNA template. After the metallisation procedure was complete, the samples underwent SEC into Tris buffer pH 8.5.

The YOYO-1/DNA sample solutions were mixed thoroughly and 100 μl was pipetted into pre-determined wells of a 96 well 'Greiner Bio-One Cell Star plate' (Cat. No. 655073). This type of plate was deemed suitable for fluorescent analysis of YOYO-1/DNA. A fluorescent spectrophotometric scan was performed between the wavelengths of 450–650 nm and the emission observed.

4.5 Results and outcomes

This section discusses the results and outcomes from the DNA immobilisation and metallisation studies.

4.5.1 The formation of a DNA capture layer

Initially a DNA capture layer was formed on the gold Biacore chip surface to validate the protocols that were to be used to place DNA specifically on the sensing tips of the accelerometer by complementary hybridisation.

4.5.1.1 The immobilisation of DNA oligonucleotide probes on a gold layer

The sensorgram in Figure 4-9 shows the change of 'Response units' with the addition of 1 μM probe A for 30 minutes over the sensor surface. Immediately after the start of the injection of the probe there was a change of response units with time. The rate of association was initially fast which is indicated by the rate of change of response units with time, where the rate slows coming near to a plateau after 30 minutes. After the injection was completed there was a slight reduction in the change of response unit value; this can be attributed to the removal of non-specifically bound probe in the deposition solution near the sensor surface being removed, this is known as the bulk contribution.

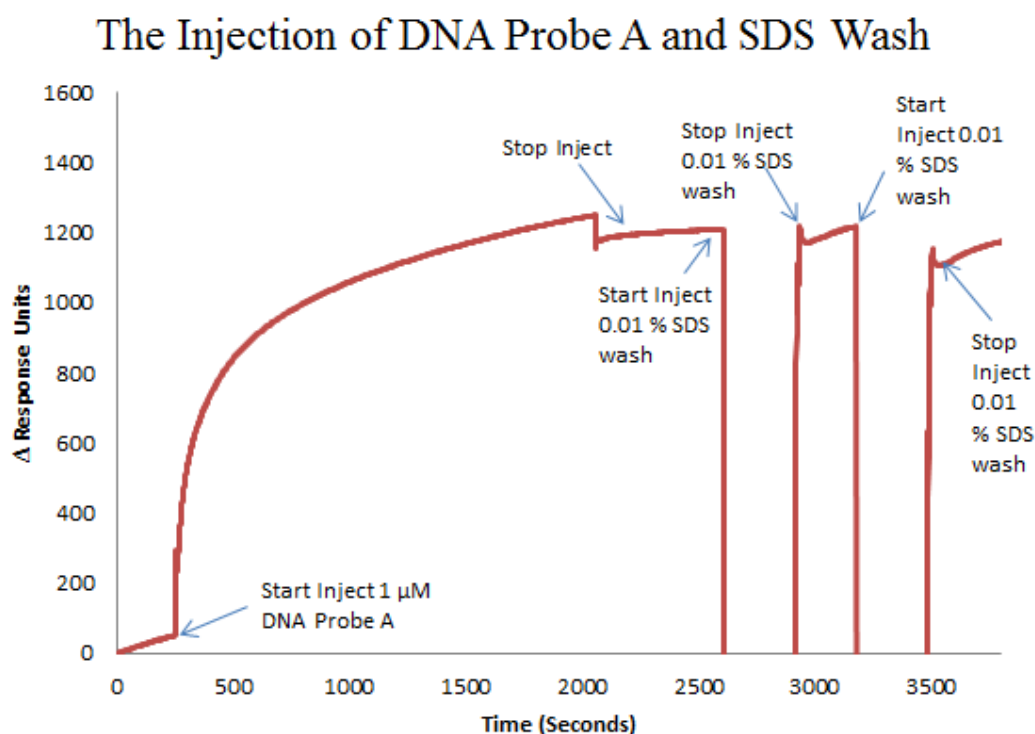


Figure 4-9: A representative sensorgram which displays the addition of probe A to the gold sensor and subsequent SDS wash steps.

At the start of the SDS wash injection, the response unit value drops off the scale to a negative value due to the difference of the refractive index. As shown in the sensorgram, after the second SDS wash there was a slight decrease of response units once back in running buffer. This may be explained by the removal of weakly bound probe molecules that can be weakly attached to gold, rather than being chemisorbed to the surface by the thiol bond. An RU change of 1203 (± 53) was observed for the immobilisation of probe A for all samples ($n=3$).

4.5.1.2 The mercaptoethanol backfilling procedure

The mercaptoethanol backfilling procedure was performed onto gold sensors chip that had previously been functionalised with oligonucleotide probe A. This protocol has been previously used in the literature to block the gold surface once a specific layer has been immobilised (Herne and Tarlov 1997; Levicky, Herne et al. 1998; Steel, Levicky et al. 2000; Keegan, Wright et al. 2005). As seen in Figure 4-10 the 30 minutes injection showed that initially the response units increased due to the chemisorption of MCE to the gold surface

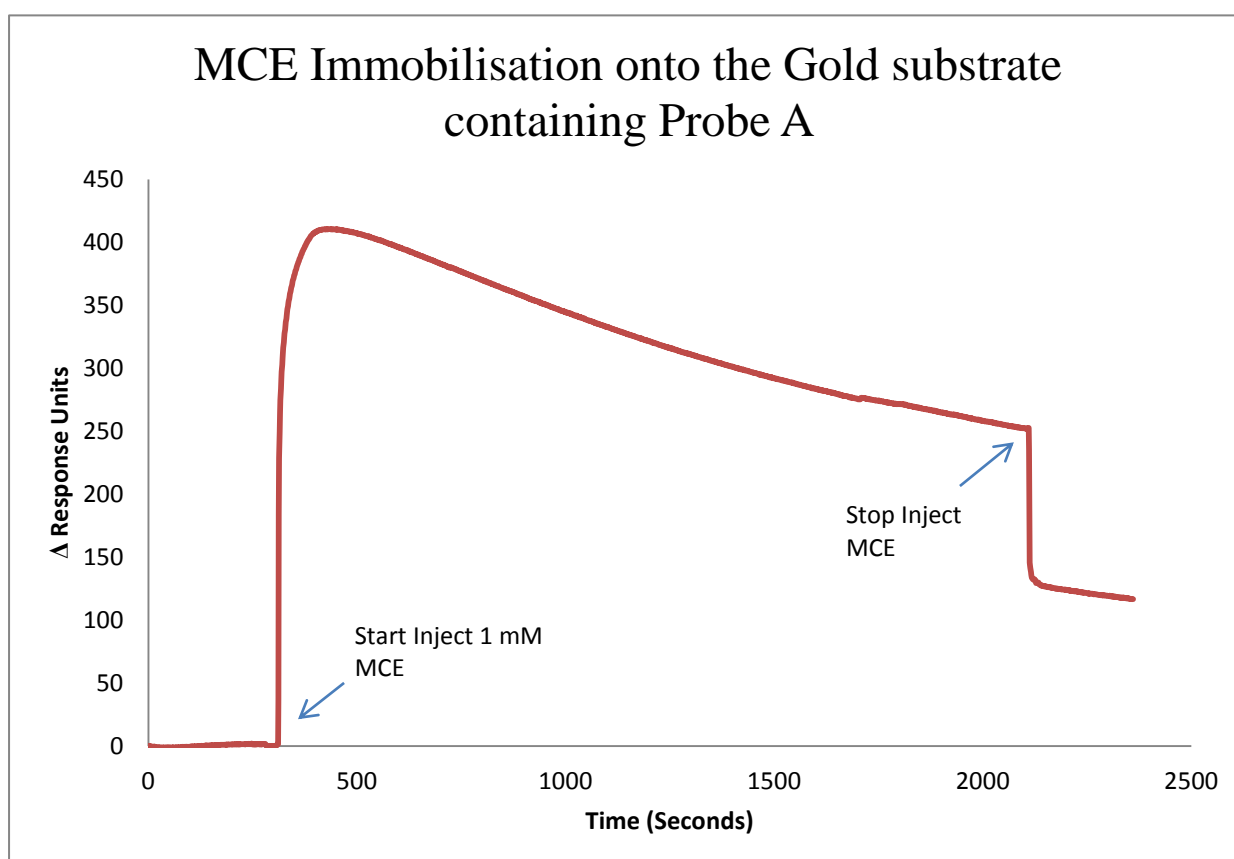


Figure 4-10: A representative sensorgram displaying the addition of 1 mM mercaptoethanol to the probe A self-assembled monolayer.

with time. Once the MCE molecules had saturated the surface, the change of response units started to decrease, indicating that mass was being removed. The change could possibly be due to the removal of weakly bound larger DNA probe molecules due to the strong chemisorption of MCE molecules. The response shown and the values obtained were observed for all trials of the experiment performed. The addition of MCE does not drop the Δ RU below that of what it was pre-injection, giving an increase of 130 RU (\pm 20) for all trials ($n=3$). Whatever the reason for the reduction of the RU value after saturation, it was not envisaged to pose any problems for the application of this project.

4.5.2 The hybridisation of non-modified Lambda DNA and control study

An analysis was performed to investigate the hybridisation of λ -DNA to the oligonucleotide probe A capture layer on the sensor surface, a sensorgram that was obtained is displayed in Figure 4-11. The sensorgram shows the 30 minutes injection and the increase of RU with time. Once the injection was complete and running buffer was flowing through the flow cell; an increase of approx. 1200 RU (\pm 24) was observed for all trials ($n=3$). This suggested that mass had been added to the surface which was likely to be due to complementary DNA hybridisation.

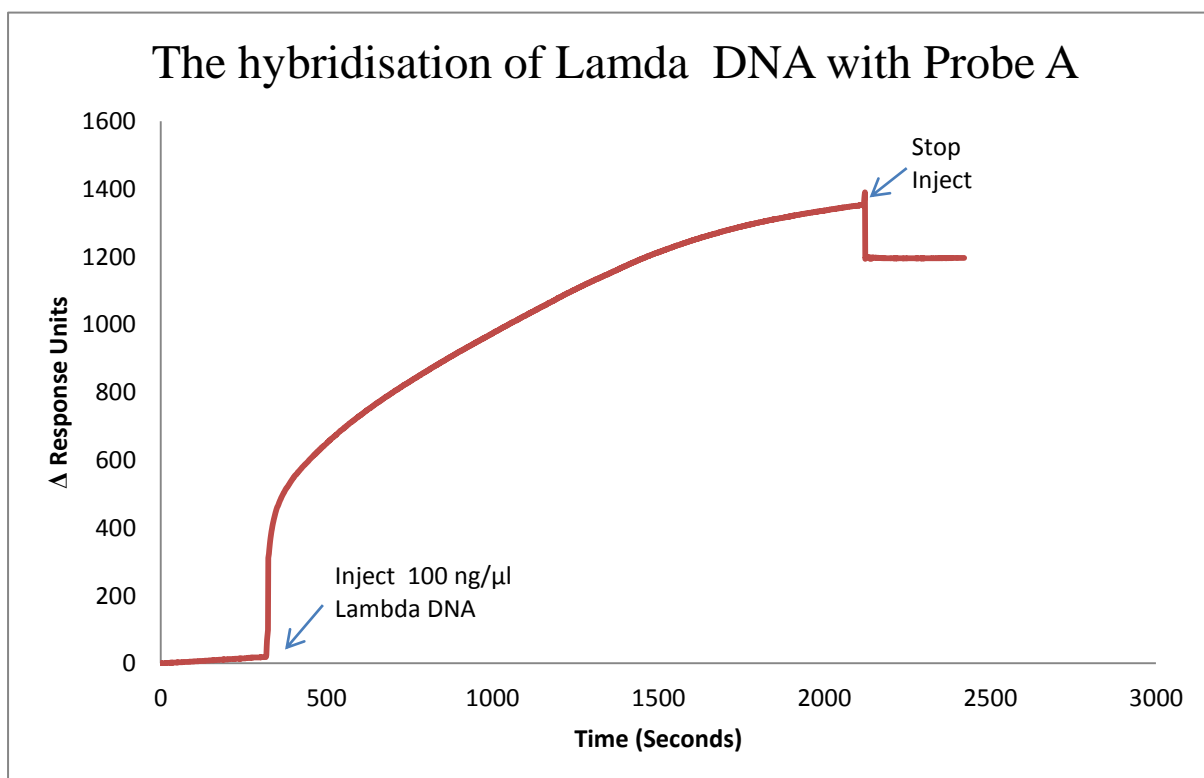


Figure 4-11: A sensorgram depicting the hybridisation of λ -DNA to probe A on the sensor surface.

The ability to hybridise λ -DNA specifically on the gold surface was the factor that determined the success of the protocols where it was not desired to obtain the maximum hybridisational efficiency. This was due to the fact that it was preferential to span only a modest amount of λ -DNA molecules in the sensing gap; therefore the optimisations of the probe and MCE chemisorption protocols were not a high priority.

The sensorgram shown in Figure 4-12 first illustrates a control step performed with the injection of the non-complementary DNA-Z and secondly the injection of complementary λ -DNA afterwards for a single sensorgram. The injection of DNA-Z to the sensor surface in all trials ($n=3$) showed an increase of approx. 75 RU (± 15), suggesting a small amount of mass had become bound to the surface. If a 1:1 hybridisation was to occur it is envisaged that an increase of RU with a value of 1100 would be measured therefore the minor increase allowed the assumption that the majority of the gold surface was blocked allowing only negligible non-specific interaction to occur.

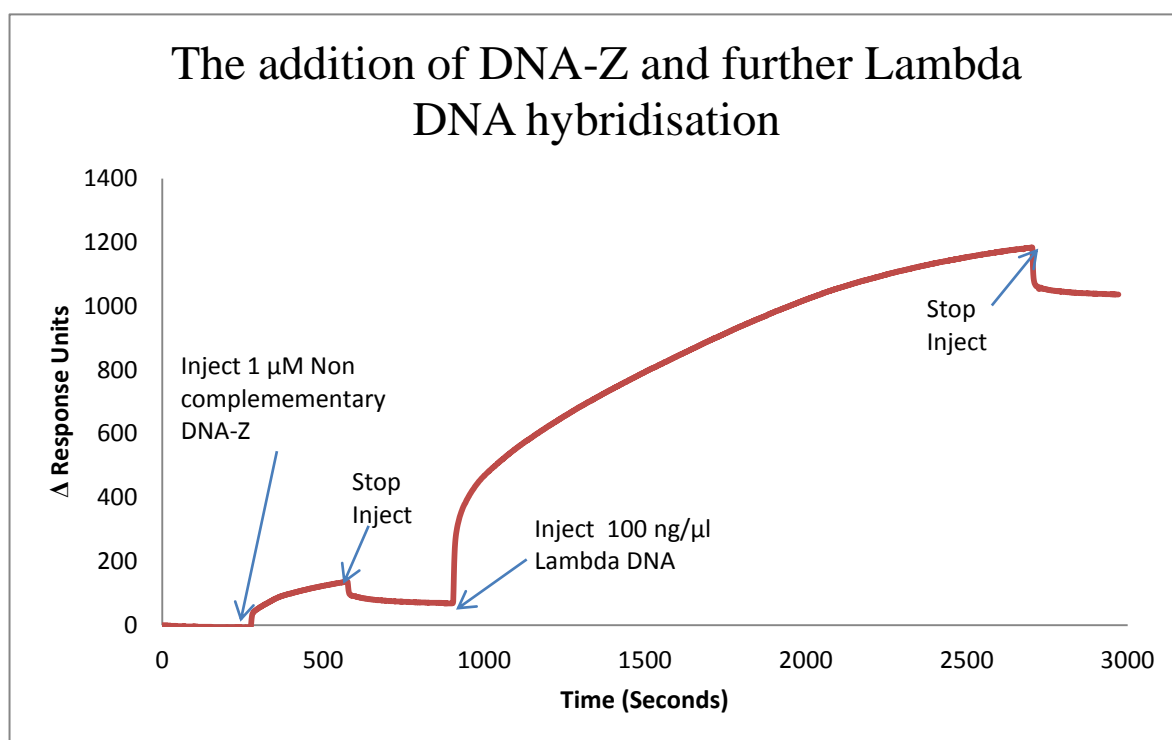


Figure 4-12: A representative sensorgram displaying the injection of a non-complementary probe and the further injection of λ -DNA to hybridise with probe A.

The injection of the complementary λ -DNA shows a tenfold increase of Δ RU to that of DNA-Z. This was due to the construction of a well ordered packed SAM using the oligonucleotide probe A and MCE backfilling protocols. Though the Δ RU value was slightly lower for that

when λ -DNA was injected over a fresh capture layer, as indicated in the previous sensorgram on page 105. This may indicate that the initial increase of Δ RU of DNA hybridisation to the surface could be initially due to minor non-specific interaction; this would have to be investigated further for a final conclusion to be drawn which is not the aim of this study.

4.5.3 The comparison of λ -DNA hybridisation protocols

A comparison between the hybridisation protocols was undertaken for λ -DNA, λ -DNA-B and λ -DNA-C where an outcome for single trial of all three λ -DNA types is displayed in the chart in Figure 4-13. Please refer to page 97 for the definitions of the λ -DNA types. It was observed that λ -DNA and λ -DNA-B displayed a comparable amount of association due to the similar increase of RU. The λ -DNA showing a change of 1195 RU (± 17) and λ -DNA-B a change of 1384 RU (± 27) that was performed for the trials (n=3). Though the λ -DNA-C injection showed a change of 94 RU (± 5) for all trials (n=3) which was similar to that of non-specific interaction that was discussed for Figure 4-12.

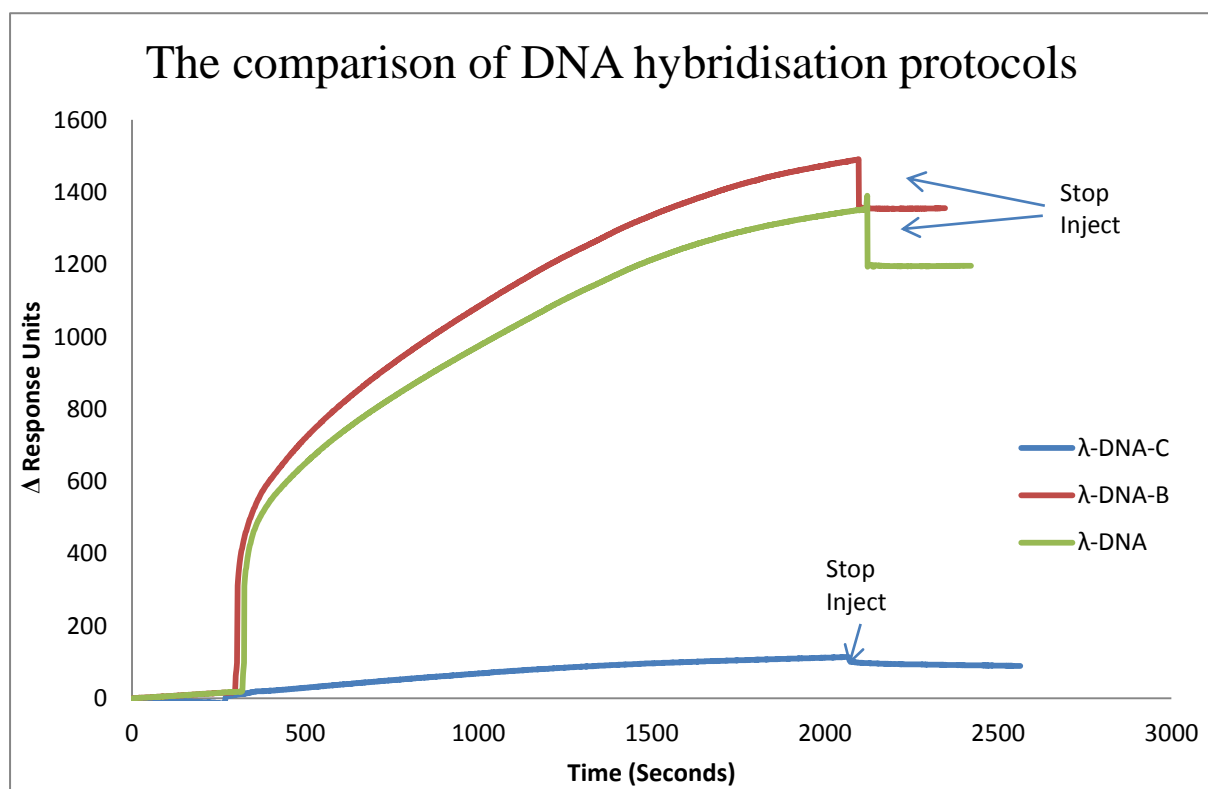


Figure 4-13: A representative chart showing a comparison between the DNA hybridisation protocols.

The explanation for the λ -DNA and λ -DNA-B protocols showing a comparable amount of association may be due to both types having a similar amount of free DNA termini in the injection solution being available for hybridisation. The variation between the increase of RU (approx. 190 RU) may be explained by the fact that λ -DNA has the ability to associate with itself under hybridisational conditions therefore reducing the hybridisational efficiency. The λ -DNA-B having one termini blocked by probe B cannot undergo the process of self-hybridisation increasing the rate of hybridisation to the capture layer. Therefore leading λ -DNA-B to have the largest increase of RU. The low value of Δ RU for the λ -DNA-C trials was vital as it proves that λ -DNA and λ -DNA-B are truly hybridising to the DNA probe capture layer. The λ -DNA-C having a value close to that of non-specific interaction with the surface. The value of Δ RU indicates the re-circularisation process performed was accomplished.

4.5.4 The ligation of Lambda DNA to the capture layer

An investigation was undertaken to validate that the ligation of λ -DNA hybridised at the capture layer surface was performed effectively. This ensured that a covalent bond was formed between the λ -DNA and probe A on the surface making it able to withstand harsher environments. The use of a pH 13 buffer was used as a control to determine if ligation had occurred, if ligation was not performed it was expected the high pH would remove the hybridised DNA from the capture layer due to the dissociation of the complementary hydrogen bonds. As shown in Figure 4-14 the hybridised λ -DNA was removed by the addition of the pH 13 buffer with an Δ RU of -1650 (\pm 78) for all trials (n=3). Thought the value being 500 RU larger than what would be expected to be removed as the data previously showed that a λ -DNA hybridisation was approx. 1200 RU. This data proves that the hybridised λ -DNA can be removed by dissociation when placed in harsh pH environments.

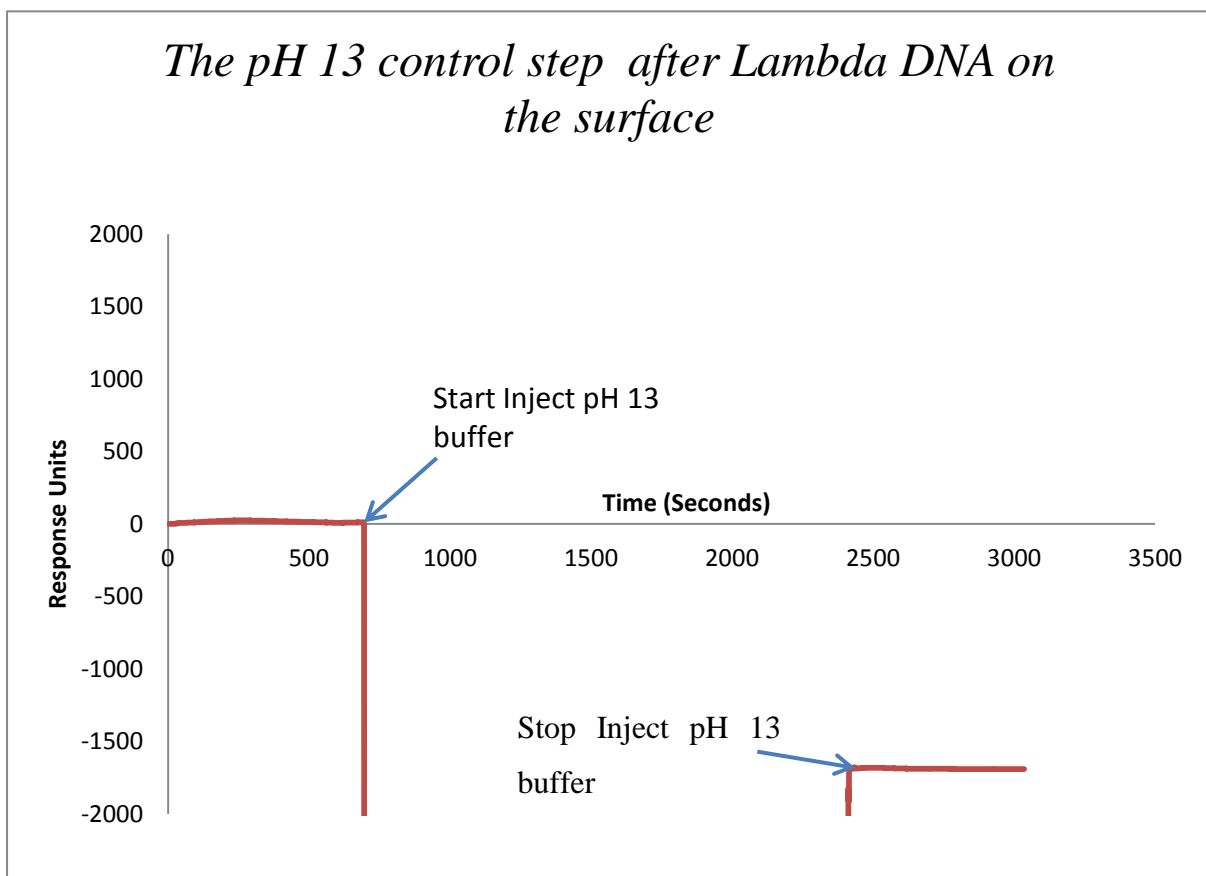


Figure 4-14: A representative sensorgram showing the removal of hybridised λ -DNA from the surface. The sensorgram is normalised to zero to convey the degree of Δ RU more clearly. The injection of the pH 13 buffer solution causes the line to go off the scale due to the large difference of the refractive index which returns once back in running buffer.

To validate that the ligation protocols were effective to make a more robust λ -DNA at the surface the high pH experiment was performed. As displayed in Figure 4-15 after the addition of the high pH buffer solution a Δ RU was measured to be $-470 (\pm 23)$ for all trials ($n=3$). This value was higher than expected which could be for two reasons; first because the high pH solution may have removed some non-specifically surface bound material like discussed for Figure 4-14 and secondly due to the ligation efficiency. Though the majority of λ -DNA was not removed proving that a ligation had occurred on the surface. This will enable λ -DNA that is spanned across the sensing gap to be permanently positioned by a covalent bond for it to be stretched more robustly and more temperature tolerant.

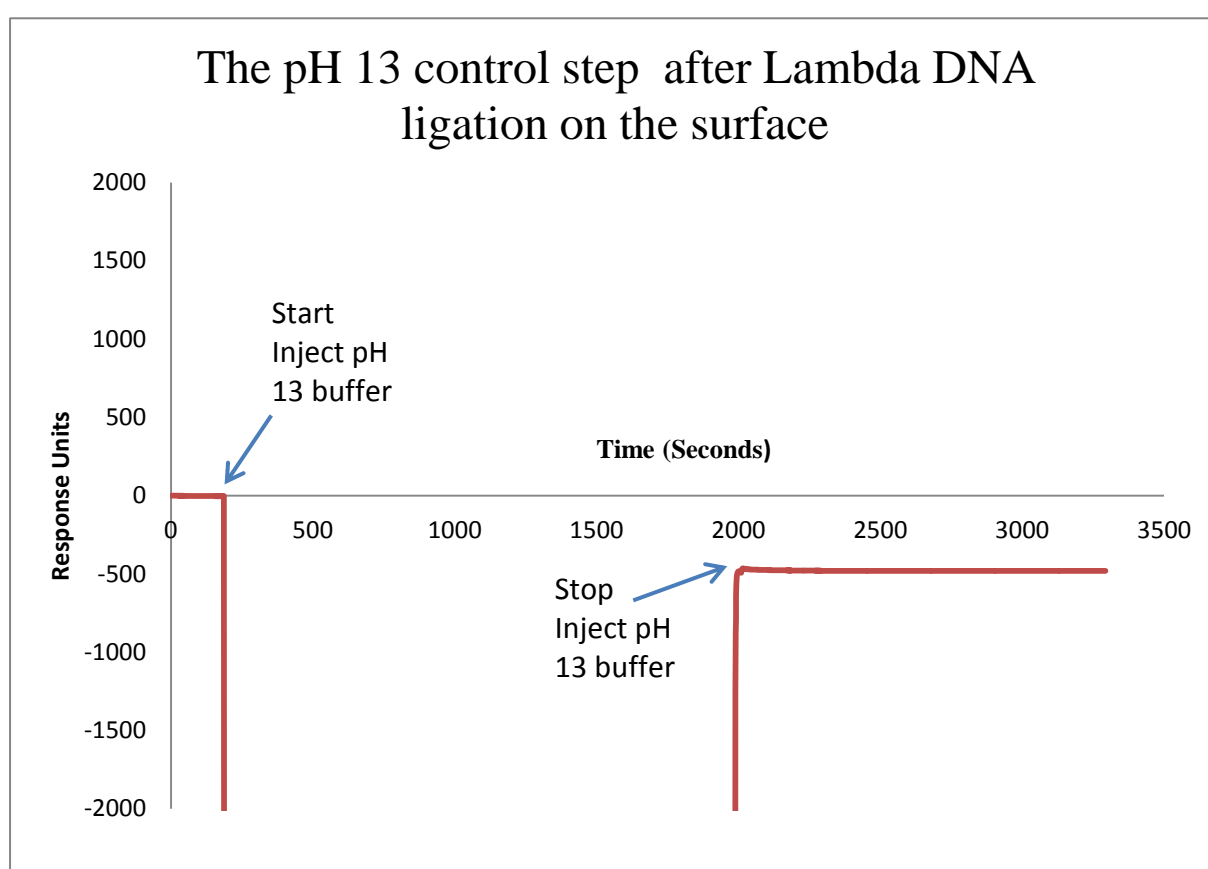


Figure 4-15: A representative sensorgram showing the injection of the pH 13 buffer solution ligated λ -DNA on the surface. The sensorgram is normalised to zero to convey the degree of Δ RU more clearly.

The immobilisation and hybridisation protocols were proved to be sufficient to be performed with the accelerometer for the application of the specific placement of λ -DNA in the sensing gap. The chemical placement of λ -DNA has been reported in the literature (Braun, Eichen et al. 1998) in a qualitative manner while this thesis reports evidence in a quantitative fashion

that is shown by the SPR data. The data displays that the hybridisation of λ -DNA measured an RU change smaller than what would be envisaged, though the experiments were clearly reproducible and highly specific. The low value of Δ RU compared to what was envisaged was ideal as for this project as it was wished to place a diminishing amount of DNA in the sensing gap. Although it was also necessary to investigate the protocols to metallise the DNA molecule to enhance the electrical properties which is discussed in the following section.

4.6 The production of M-DNA using Zinc ion Metallisation Protocols

The purpose of performing the protocols in this section was to investigate the metallisation DNA to produce M-DNA. As discussed in chapter 1 there has been a variety of DNA metallisation protocols reported in the literature. Though most of the protocols developed do not allow the DNA molecule to keep its natural structural properties which may have been the reason for using DNA in the first instance. The purpose of the research was to employ DNA as a biological strain gauge; therefore the elastic properties were needed to be retained.

The use of the divalent zinc ions to form M-DNA was investigated using the compound zinc Perchlorate ($Zn(ClO_4)_2$). The zinc cations have been reported to readily form a complex with the DNA template at alkaline pH by replacing the imino proton of a base pair (Aich, Labiuk et al. 1999). The formation of M-DNA can be monitored by UV-Vis spectroscopy where a redshift of the peak maxima compared to that of pristine DNA is observed. Redshift being the increase of wavelength due to shifting to a lower energy state. The redshift of the peak maxima A_{260} was monitored in this study to determine if M-DNA was produced. Additionally a fluorescence assay was produced using the fluorophore YOYO-1 to determine if metal ions were being associated with the DNA molecule and to determine if competition for the active sites is observed. Previous studies have used a fluorescence assay alongside M-DNA formation using the fluorophore ethidium bromide where the fluorescent properties were shown to be reduced with increasing metal ion concentration. This is explained in two articles to be due to the competition for the DNA active sites (Wettig, Wood et al. 2003; Omerzu, Mihailovicacute et al. 2007).

4.6.1 The formation of M-DNA validated by UV-VIS Spectroscopy

The absorbance peak maxima properties of DNA in divalent zinc ion solution at pH 8.5 was monitored using UV-Vis spectroscopy by performing a spectrum scan between the wavelength range 240 - 320 nm. First, the protocol was refined using Calf thymus DNA for ease of use and the reduction of cost of using large volumes. Secondly the metallisation chemistry was applied with λ -DNA once the protocol was refined. The use of an EDTA scavenger control was performed, the EDTA molecule can sequester metal ions from the DNA template. The treatment of metallised DNA with EDTA will revert the molecule back to its pristine form. This ensured that the peak shift observed was due to metal ion association to the DNA template and not another contributing factor.

4.6.2 Zinc Perchlorate & CT DNA

UV-Vis spectrum scans were performed on CT DNA with varying $\text{Zn}(\text{ClO}_4)_2$ concentration to investigate the peak shift produced by the metal ion association (Aich, Labiuk et al. 1999; Omerzu, Mihailovicacute et al. 2007). The $\text{Zn}(\text{ClO}_4)_2$ has been used previously in the literature and it has been described to have fewer problems associated with precipitates that may occur.

The chart in Figure 4-16 shows a UV-Vis spectrum of CT DNA metallised using $\text{Zn}(\text{ClO}_4)_2$ alongside a pristine and EDTA control. As observed in the chart, a peak shift of 5 nm was measured by metallising the DNA using 5 mM $\text{Zn}(\text{ClO}_4)_2$. The pristine DNA and EDTA control spectrum show the same characteristics of peak maxima suggesting that the peak shift observed was created by zinc association. The peak shift of 5 nm (± 0) was observed for all trials undertaken (n=3) when using a 5 mM concentration (the resolution of the instrument being 1 nm).

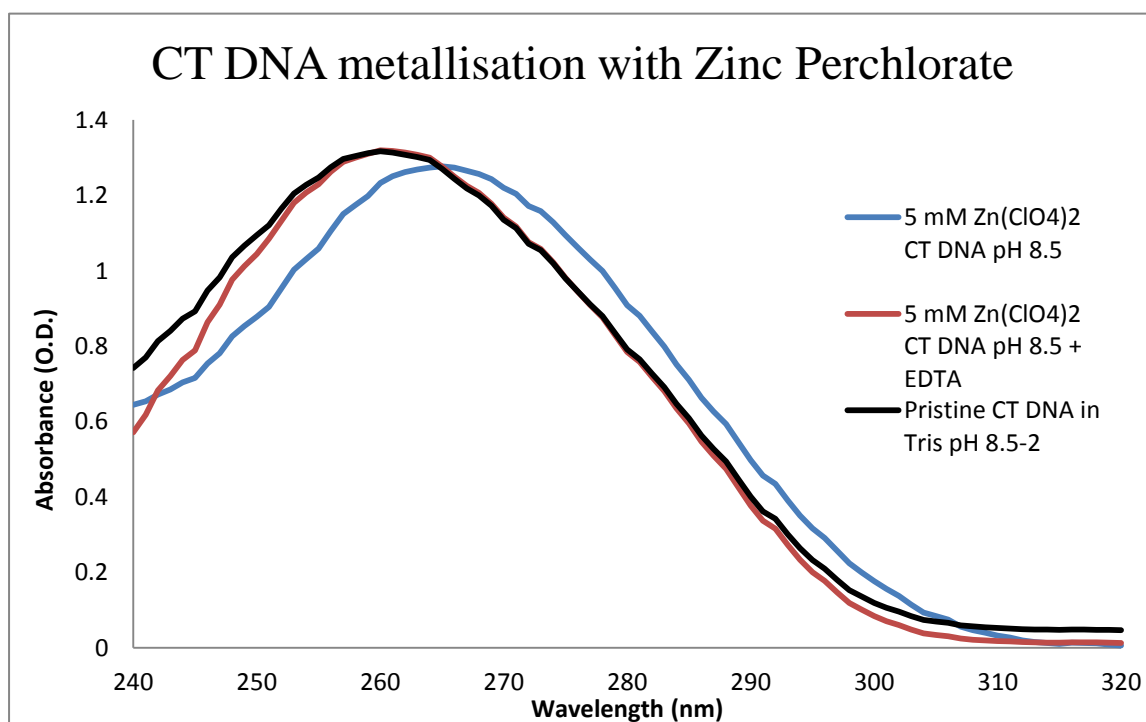


Figure 4-16: A representative chart showing Calf Thymus DNA treated with 5 mM zinc perchlorate.

A study was performed to find the saturation point of CT DNA with zinc ions using the zinc perchlorate compound. The chart in Figure 4-17 shows the peak shift value with the increasing $Zn(ClO_4)_2$ concentration.

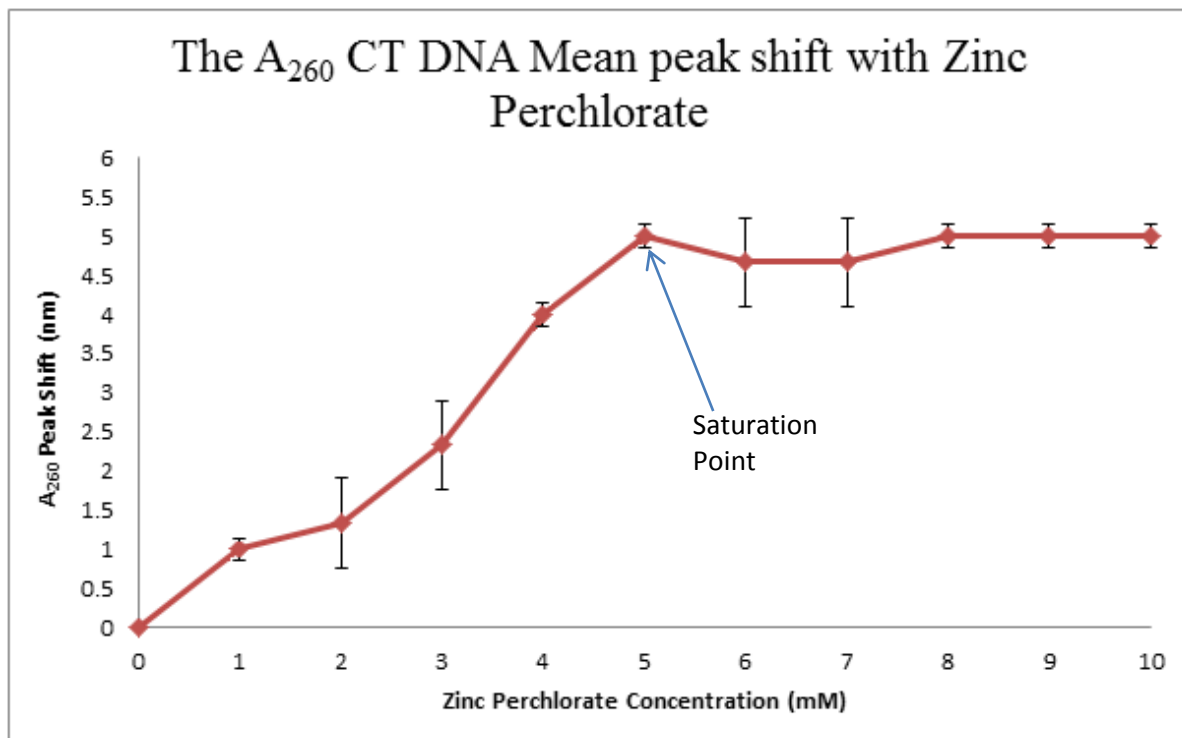


Figure 4-17: A chart showing the A_{260} peak shift of CT DNA with varying $Zn(ClO_4)_2$ concentration.

A peak shift plateau was observed with a maximum value 5 nm that began at 5 mM. This suggests that the association of zinc ions with the DNA template had reached a saturation point as there was no remaining free sites, producing a fully metallised DNA molecule.

4.6.3 The metallisation of λ -DNA

The metallisation protocols using both zinc compounds were performed on λ -DNA once a suitable method had been developed. It was undertaken to confirm that the chemistry involved for the metallisation with CT DNA was as efficient with λ -DNA for the application of placement in the sensing gap of the accelerometer. A suitable range of concentrations of the zinc source was used to investigate the A_{260} peak shift.

The chart in Figure 4-18 displays the measured peak shift of λ -DNA with increasing zinc perchlorate concentration. It shows that the peak shift increases with concentration as observed using CT DNA. A slight peak shift plateau was observed at 3-4 mM with a value of 4 nm before proceeding to approx. 5 nm with increasing concentration.

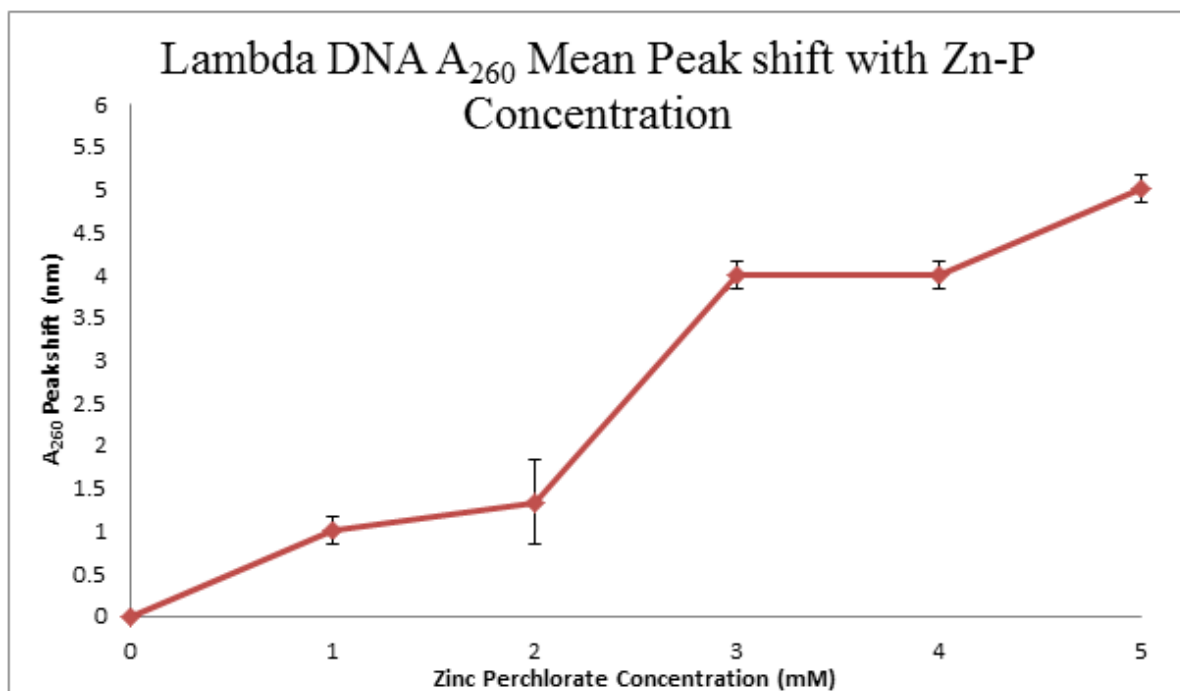


Figure 4-18: A₂₆₀ Peak shift of λ - DNA with zinc Perchlorate concentration.

The observed peak shift of λ -DNA with metal ion concentration was in agreement with that of CT DNA indicating that the type of DNA does not change the degree of metallisation. The metallisation of the CT and λ -DNA was confirmed to have taken place by monitoring the peak shift that was caused by the association of divalent metal ion zinc. This study is in agreement with what has been discussed previously in the literature, where metallised DNA has been compared to that of an EDTA control experiment. This suggests that the DNA metallisation protocols in this study were successful by observing the optical absorbance properties. As a complementary investigation a fluorescence assay was used to determine if metallisation had taken place on the DNA template for secondary validation.

4.6.4 The metallisation of λ -DNA observed by a YOYO-1 fluorescence assay

A fluorescence assay was undertaken to investigate the change of the emission properties of the YOYO-1 fluorophore associated to λ -DNA when metallised by the protocols discussed. In the literature it has been reported that the metallisation of DNA has reduced the emission properties of ethidium bromide with increasing metal ion concentration (Wettig, Wood et al. 2003; Omerzu, Mihailovicacute et al. 2007).

The fluorescent based assay was used to complement the UV-Vis A_{260} peak shift investigation, observing the YOYO-1/DNA fluorescent emission with metal ion association. For initial fluorophore labelling protocols λ -DNA was labelled with a 5:1 ratio (DNA: Dye) with the fluorophore YOYO-1. A YOYO-1/DNA solution with a concentration of 10 ng/ μ l underwent UV-Vis and fluorescent spectroscopy. The optical density and the relative fluorescence units (RFU) of the excitation and emission respectively were measured using the Tecan M-200 fluorimeter. The image displayed in Figure 4-19 shows a chart of the excitation and emission peak maxima of the fluorophore when associated with λ -DNA. The emission peak maxima being centred at 509 nm which was monitored with metal ion concentration.

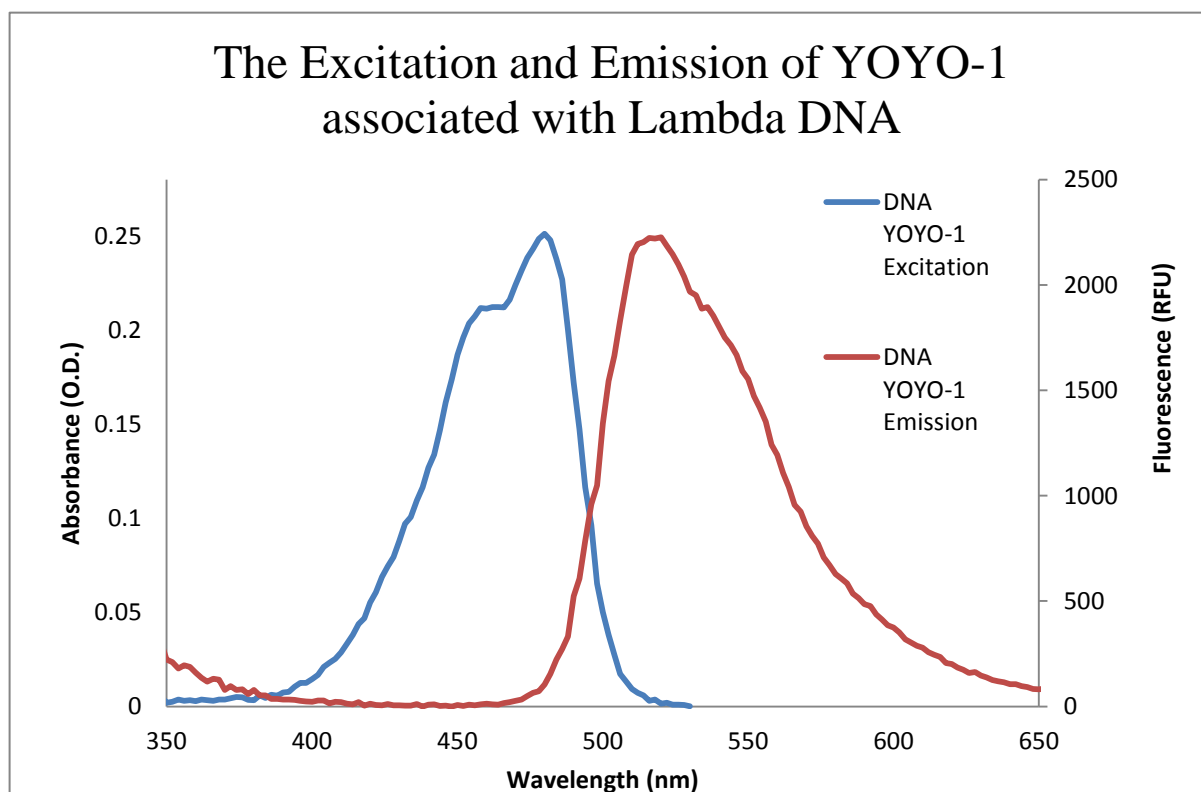


Figure 4-19: The YOYO-1 fluorophore excitation and emission maxima peaks when associated with Lambda DNA.

4.6.4.1 The fluorescent emission observation of YOYO-1/DNA metallised with $Zn(ClO_4)_2$

The peak RFU values were also investigated for the metallisation of YOYO-1/DNA with $Zn(ClO_4)_2$. The data that is shown in Figure 4-20 displays the peak RFU values obtained. As portrayed a decrease of fluorescent emission was observed with increasing metal ion concentration.

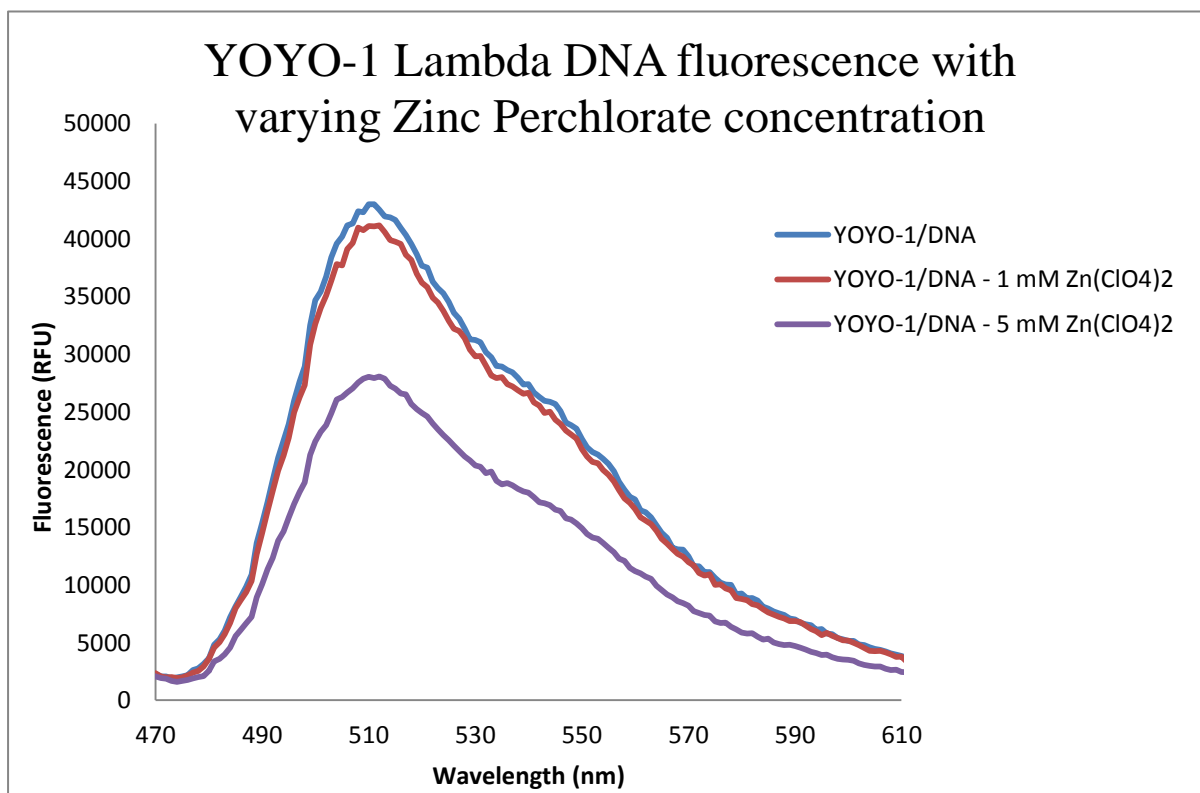


Figure 4-20: A comparison between the YOYO-1 emission maxima peaks between varying $Zn(ClO_4)_2$ concentration.

The change of fluorescent intensity of YOYO-1/DNA was shown to have similar properties when metallised by the zinc compound. The addition of zinc ions was shown in both instances to cause a decrease in the fluorescent intensity of the DNA bound YOYO-1 fluorophore. This may occur due to a competition event between the fluorophore and the zinc ion to associate with the DNA template.

4.6.5 Zinc Perchlorate Saturation analysis

To determine if an endpoint to the level metallisation and RFU reduction could be found an investigation was performed using a range of $\text{Zn}(\text{ClO}_4)_2$ concentrations. This allowed the saturation point that was previously measured and discussed from Figure 4-17 to be compared by monitoring the extent of peak RFU reduction with metal ion concentration. The chart in Figure 4-21 presents the measured intensity's with increasing $\text{Zn}(\text{ClO}_4)_2$ concentration.

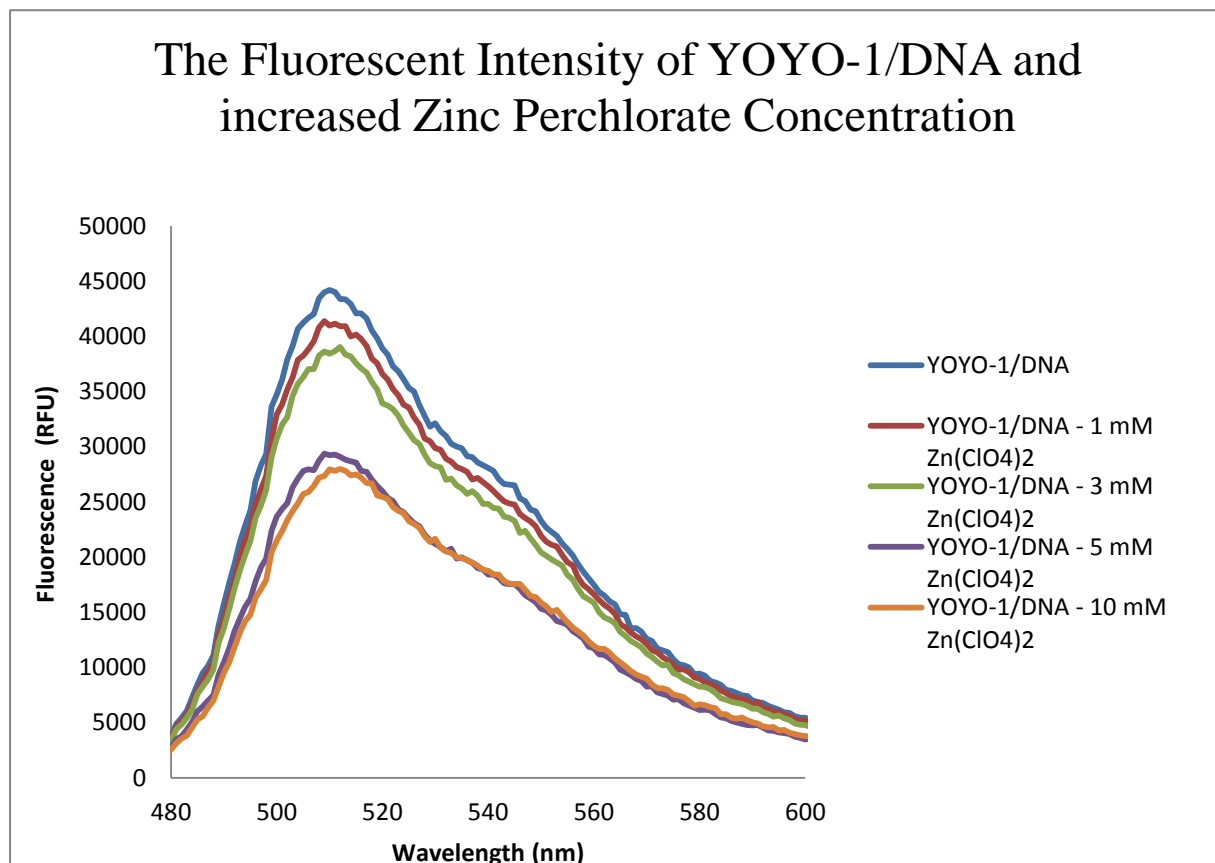


Figure 4-21: The fluorescent intensity of YOYO-1/DNA treated with ranging zinc Perchlorate concentration.

The peak RFU values of 5 and 10 mM are shown to be similar indicating that the amount of fluorescent attenuation may have reached a plateau where all the zinc association sites are occupied which can no longer take effect on the fluorescent properties. The chart in Figure 4-21 highlights the level of fluorescent attenuation with $\text{Zn}(\text{ClO}_4)_2$ concentration which allows the saturation point to be displayed more clearly. The saturation point observed at 5 mM is in agreement with the UV-Vis spectrophotometric investigation monitoring the DNA A_{260} peak shift. This study has allowed the zinc ion and DNA saturation concentration to be identified.

The data in Table 4.3 displays the mean average RFU values obtained for the study, the maximum decrease of intensity being 63 % of that of YOYO-1/DNA. A previous study reported a 100 % quenching of ethidium bromide fluorescence using much lower zinc concentrations (Wettig, Wood et al. 2003; Omerzu, Mihailovicacute et al. 2007) at the saturation point. This may indicate that the DNA was metallised whilst retaining a large degree of the fluorescent properties. The YOYO-1 molecule has been suggested to be able to associate to the DNA template at various sites. Hence this study suggests that a metallised and fluorescent molecule may have been formed to make a novel fluorescent M-DNA whilst retaining the spring like properties. This will allow the placement of metallised DNA than can be visualised fluorescently for a bioelectronic application and in this study for the placement in the sensing gap of the accelerometer.

Zn(ClO₄)₂ Concentration (mM)	Mean Fluorescent Value (RFU)	Percentage of Pristine DNA/YOYO-1 RFU value
0 (YOYO-1/DNA)	44129 (±501)	100 %
1	41358 (±497)	93.7%
3	38404 (±268)	87.0%
5	28548 (±639)	64.6%
10	27842 (±203)	63.0%

Table 4.3: The fluorescent values of YOYO-1/DNA and Zn(ClO₄)₂ concentration.

4.7 Discussion

The immobilisation and DNA metallisation protocols were shown to be effective and repeatable, therefore allowing the chemistries to be applied for the application of a DNA accelerometer. The immobilisation and hybridisation procedures for the placement of λ -DNA onto gold substrates were proved to be effective using the Biacore system, this allowed the DNA immobilisation protocols to be performed on the gold sensing tips of accelerometers.

The metallisation protocols investigated allowed the DNA molecule to be metallised to produce M-DNA that may allow the electrical properties to be improved from that of pristine λ -DNA. This will allow the future application of greater sensitivity of DNA acting as a sensing element in an accelerometer configuration. The next step of the DNA positioning and placement for the sensing application is detailed in chapter 5.

5 Chapter 5 The positioning of YOYO-1/DNA on accelerometer substrates

This chapter discusses the placement of DNA molecules onto accelerometer substrates using the SAM thiol chemistry previously refined with a variety of positioning techniques. This chapter discusses the chemical immobilisation procedures that were performed to chemically anchor fluorescently labelled λ -DNA (YOYO-1/DNA) in the sensing gap. The previously investigated immobilisation chemistry discussed in chapter 4 was used to precisely position DNA by molecular combing/hydrodynamic positioning (Bensimon, Simon et al. 1995; Smith, Cui et al. 1996; Yokota, Johnson et al. 1997; Braun, Eichen et al. 1998; Rakitin, Aich et al. 2001) and electrophoretic positioning (Washizu, Washizu et al. 1990; Zimmermann and Cox 1994; Washizu, Kurosawa et al. 1995; Namasivayam, Larson et al. 2002; Germishuizen, auml et al. 2003). The aim being the placement of λ -DNA spanned across the sensing gap which is covalently attached to both opposing gold sensing tips. This was undertaken to demonstrate a proof of concept that a DNA biological accelerometer can be realised.

5.1 Introduction

The investigation of positioning λ -DNA into the sensing gap was performed by a variety of methods;

1. Molecular combing
2. Electrical positioning
 - i. DC electrophoretic positioning
 - ii. AC dielectrophoretic positioning

This chapter discusses the methods and apparatus that were employed to allow the immobilisation and positioning of DNA in the sensing gap. The immobilisation and positioning scheme that is highlighted in Figure 5-1 shows DNA spanned across the sensing gap by thiol linkage to the gold. The molecular combing method was performed to investigate the validity to position DNA. This was initially performed by combing YOYO-1/DNA free in solution on a glass microscope slide without any immobilisation chemistry. Once the method was developed it was further performed with specifically immobilised λ -DNA with probe A pre-hybridised *in-vitro* (YOYO-1/DNA+B) in the sensing gap. Due to the nature of this method the entire die was immersed in solution to make a receding meniscus, therefore the immobilisation protocols developed were not discriminate of which sensing tip the capture layer was formed for the immobilisation and subsequent positioning of DNA.

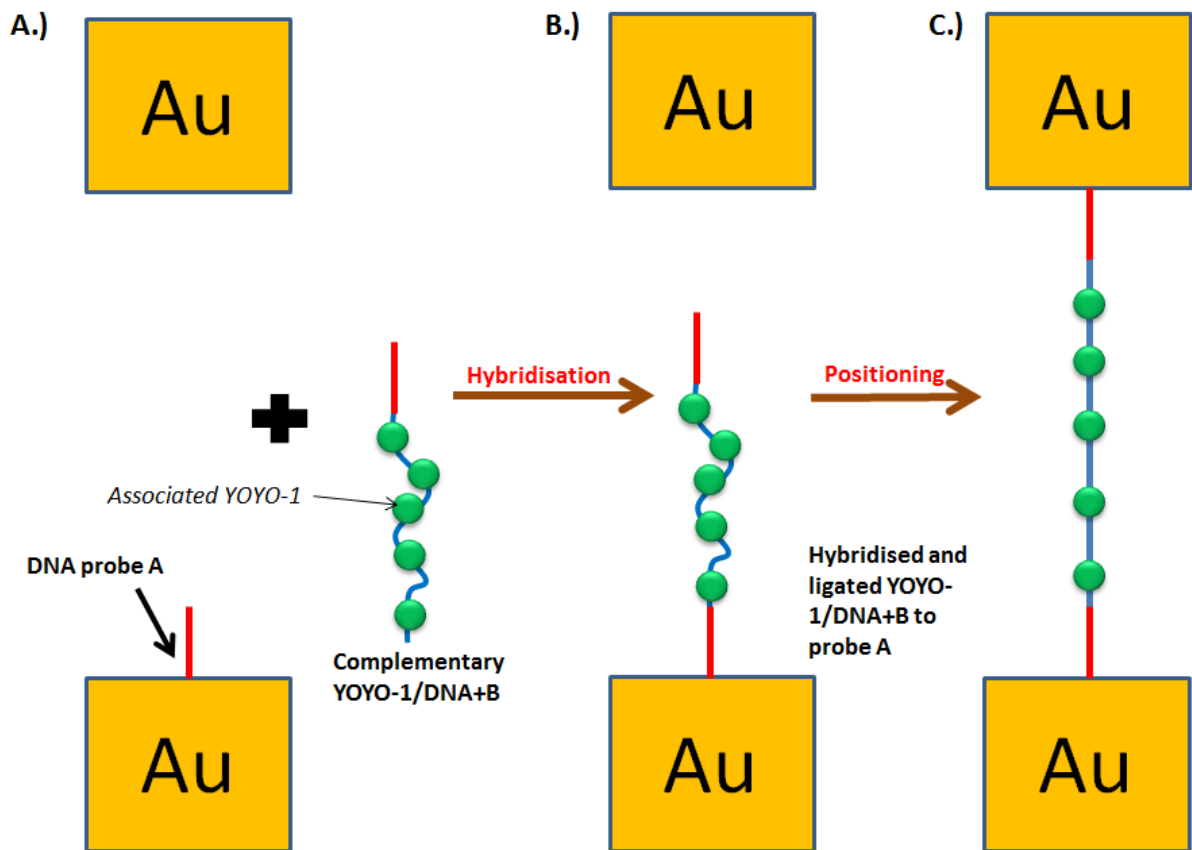


Figure 5-1: The immobilisation and positioning scheme to position DNA in the sensing gap.

A.) The DNA probe A is immobilised onto the gold surface by thiol linkage. B.) The complementary YOYO-/DNA+B molecule is hybridised and ligated to probe A on the gold surface (MCE backfilling not shown). C.) The DNA is migrated to the opposing sensing tip by positioning methods and anchored by thiol linkage.

The electrical positioning methods undertaken were a greater challenge as the accelerometer was electrically connected by wirebonding and great care had to be taken not to immerse the electrical bond pads and actuating features. The probe immobilisation and the subsequent hybridisation of YOYO-1/DNA+B was performed by dipping the die in the deposition solution using a dipping station that was assembled for this purpose. This allowed immobilisation to be performed without immersing the critical features. The dipping station allowed the immobilisation individually on the 1st sensing tip of the accelerometer without immersing the opposing tip. Once the YOYO-1/DNA+B was hybridised and ligated on the 1st sensing tip an electrical potential was used to migrate the molecule to the opposing sensing tip. A range of equipment was employed to allow the precise dipping and for the electrical positioning that was imaged in real time using fluorescent microscopy. The schematics in Figure 5-2 highlight the dipping process that was undertaken within a 10 µm limit.

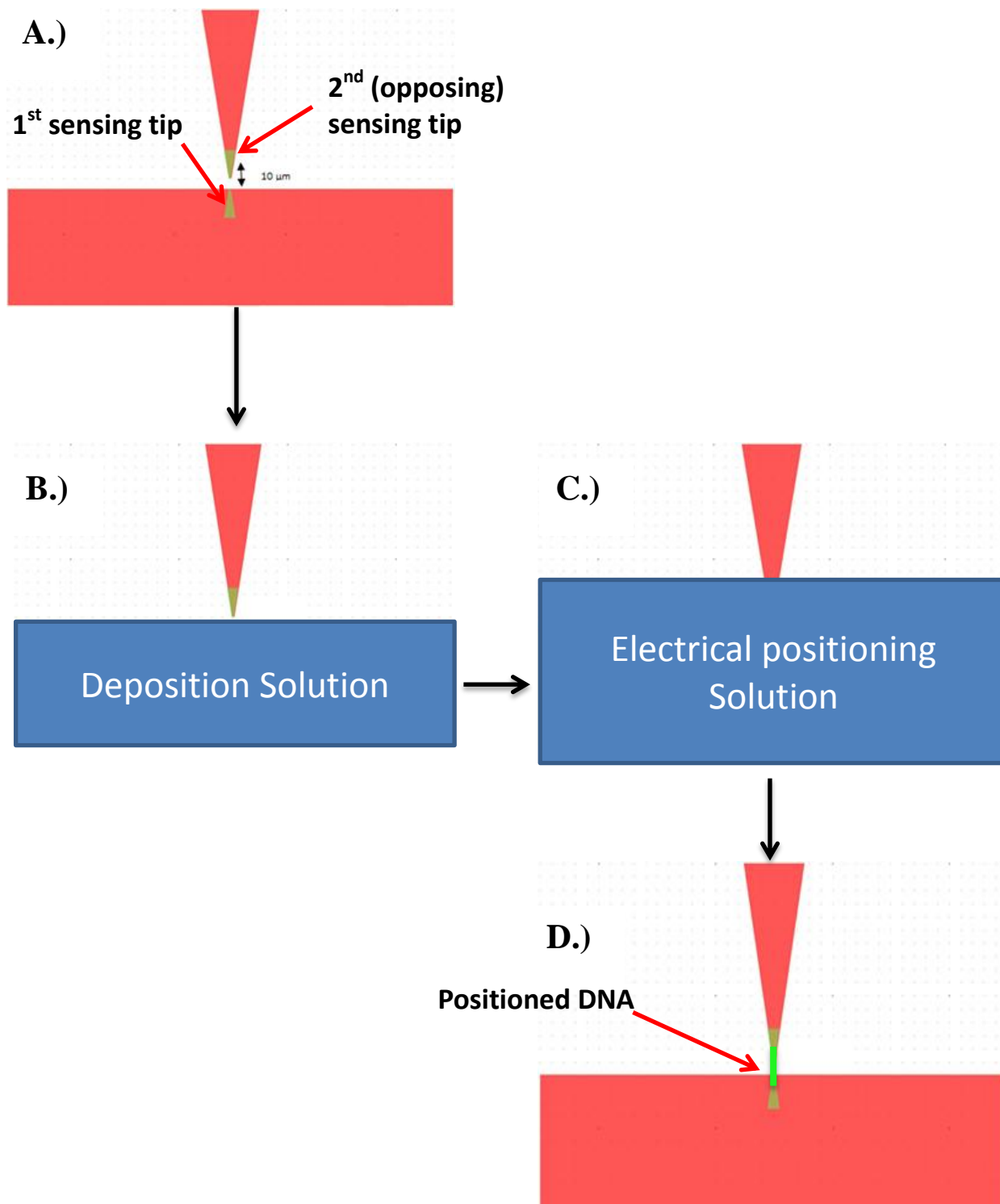


Figure 5-2: Schematics showing the procedure to place DNA in the accelerometer sensing gap by the dipping procedure with electrical positioning. A.) The 10 μm sensing gap of an accelerometer, the inset reminds the reader of the immobilisation scheme. B.) The 1st sensing tip immersed in deposition solution by dipping to allow immobilisation of YOYO-1/DNA+B. C.) Both sensing tips placed in the positioning solution to perform electrical positioning to migrate DNA to the opposing sensing tip. D.) The DNA positioned in the sensing gap.

5.2 Methods

This section details the methods that were performed to investigate DNA immobilisation and positioning in the sensing gap.

5.2.1 The molecular combing positioning techniques

This method section describes the molecular combing method to position DNA in the sensing gap. This protocol was performed as an initial experiment to conclude if molecular combing was a viable option for DNA positioning. The molecular combing method performed in this project was not discriminate of which sensing tip was immobilised with DNA due to the whole die being immersed in solution for the immobilisation and hybridisation.

5.2.1.1 The molecular combing of YOYO-1/DNA on glass substrates

First, an investigation was performed to stretch and align YOYO-1 labelled λ -DNA (YOYO-1/DNA) on a glass microscope slide using the molecular combing technique. The molecular combing technique was performed by using a 1 μ l droplet of YOYO-1/DNA (10 ng/ μ l) that was pipetted onto a glass slide, over which a glass coverslip was placed. The placement of the coverslip was undertaken to spread out the droplet over the slide which was then pulled up slowly from one side to produce a receding meniscus. Therefore stretching and aligning the DNA contained in the solution in a single uniform direction. The combed YOYO-1/DNA was imaged using the Nikon eclipse 80i epifluorescent microscope with an x100 optical magnification objective lens.

5.2.1.2 The placement of YOYO-1/DNA in the sensing gap by DNA chemical immobilisation and molecular combing

The substrate was firstly cleaned using piranha solution (70 % H_2SO_4 , 30 % H_2O_2) to remove any organic contamination that may be present. A 200 μ l solution of 1 μ M oligonucleotide probe A in 1 M phosphate buffer pH 7.4 was pipetted onto the surface for 30 minutes. After the 30 minutes, the surface was rinsed and 200 μ l of 1 mM MCE solution was pipetted onto the surface for 30 minutes to perform chemical backfilling on the gold surface. Once again after 30 minutes the surface was rinsed thoroughly, thereafter a 100 ng/ μ l YOYO-1/DNA+B solution in hybridisation buffer was eluted onto the surface for 30 minutes. As detailed in chapter 4 the oligonucleotide probe B was hybridised and ligated to the YOYO-1/DNA molecule *in-vitro* prior to immobilisation. Once the hybridisation was complete the YOYO-1/DNA+B was ligated using 200 μ l of 10 Weiss units of T4 DNA Ligase in ligation buffer for 16 hours, an excess amount was used to ensure a ligation with high efficiency. Once the

immobilisation steps had been performed sufficient rinsing was undertaken to remove non-specific DNA that may be present. Furthermore the molecular combing procedure was performed to stretch the DNA molecules in the sensing gap. The surface was wetted with a 2 μ l drop of DI water and a microscope coverslip was slowly placed over the surface in a uniform direction by hand and removed slowly in a similar fashion discussed in section 5.2.1.1.

5.2.2 The electrical positioning and dipping techniques

This section discusses the electrical positioning techniques and protocols that were employed alongside the selective dipping to immobilise selectively to the 1st sensing tip of a packaged accelerometer device.

5.2.2.1 The packaging of accelerometers for the placement of YOYO-/DNA in the sensing gap by electrical positioning techniques

The accelerometer dies that were used in this study were packaged to DIP before dipping and electrical positioning could take place. The accelerometers were fixed onto an 24 pin DIP by epoxy glue, one of the accelerometers on the die (the highest quality that was determined by optical observation) was electrically connected to the DIP packaging by wire bonding. The DIP had one end physically removed to allow the die to overhang from the edge as can be observed in Figure 5-3. This was performed to allow the ease of dipping of the sensing gap without the entire die or DIP becoming immersed in solution that may short the electrical contacts. The packaged accelerometer was then placed into a DIP chip socket to allow an ease of electrical connections to be made to the device that allowed the electrical positioning protocols to be performed. The dipping station was developed to perform the dipping whilst being imaged in real time by the user as discussed in section 5.2.2.2.

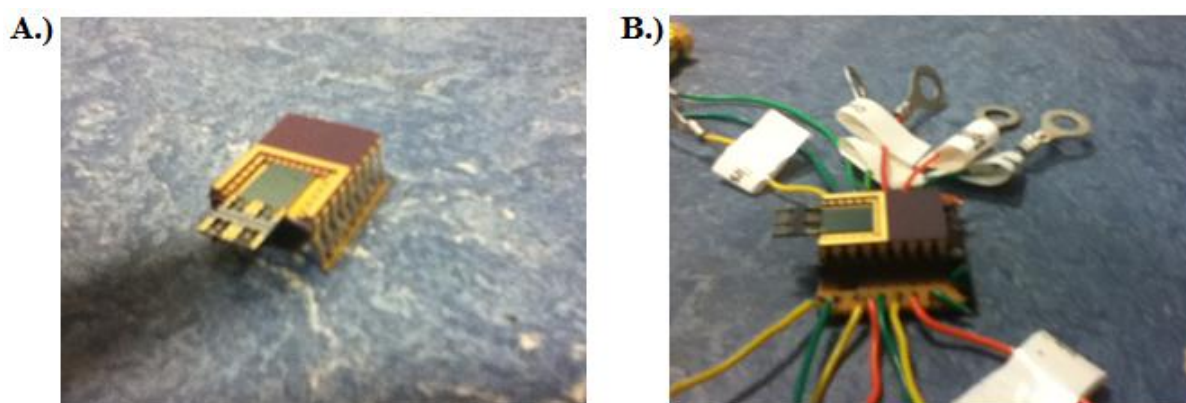


Figure 5-3: A.) A wire bonded and packaged accelerometer device in the dipping geometry.
B.) The packaged accelerometer inserted onto a chip socket.

5.2.2.2 The operation of the dipping station

The dipping station that was developed to allow the discrimination of dipping the individual sensing tips of the accelerometer in deposition solution. The dipping station apparatus is illustrated in Figure 5-4 which consisted of a 3 axis motorised translation stage (physics instruments), a camera and a monitor. The packaged accelerometer was first placed in a pre-determined position above the glassware containing the deposition solution using the motorised stage. The stage was coupled to a computer to allow dynamic operation as needed for the dipping. The staging was used to slowly dip the accelerometer sensing tip in the deposition solution that was observed on a monitor coupled to camera which was focused on the sensing gap. The camera was additionally fixed to a non-motorised translational stage which allowed the movement of the camera to allow focusing (not shown in the illustration). The use of an anti-vibration table was used to assemble the dipping station to reduce the possibility of any surrounding vibrations possibility damaging the accelerometer and to maintain focus with the camera and microscope objective.

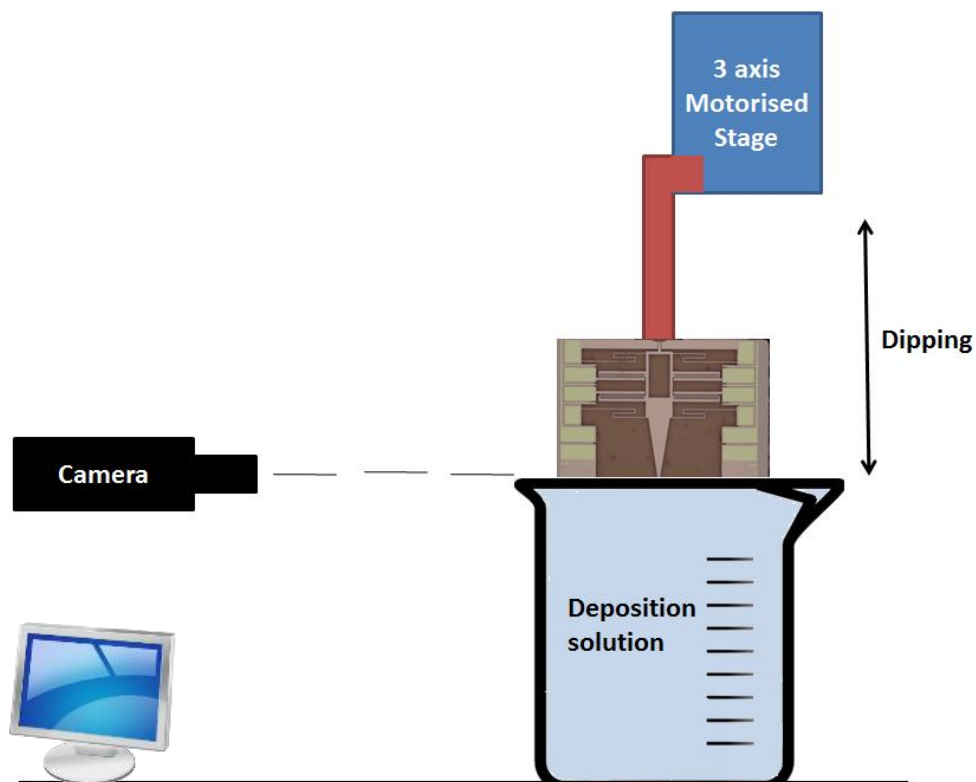


Figure 5-4: The dipping station configuration to allow the careful immersion of the sensing gap in deposition solution. The accelerometer was dipped into the glassware containing the deposition solution whilst being observed using the camera that was coupled to a monitor. The illustration is not to scale.

5.2.2.3 The selective dipping and chemical immobilisation on packaged accelerometers

A 300 µl solution of 1 µM oligonucleotide probe A in 1 M phosphate buffer pH 7.4 was placed in a glassware container, the staging was moved downwards until the accelerometer became dipped and the solution meniscus could be seen covering the 1st sensing tip. The tip remained immersed in the solution for 30 minutes after which the same was repeated to perform the backfilling procedure using 1 mM MCE for 30 minutes, the hybridisation of YOYO-1/DNA+B for 30 minutes and the ligation for 16 hours (10 Weiss units T4 DNA ligase). The time between the different immobilisation chemistries was kept to a minimum (\approx 30 seconds) when changing solutions. This was to remove the possibility of the material on the sensing tip becoming dried out which may reduce the performance of the DNA capture layer.

After the chemistries had taken place, the entire accelerometer sensing gap was immersed in DI water for the electrical positioning methods to take place. The camera was removed from the stage and the accelerometer was viewed using the microscope with a high magnification optical objective, this is further discussed in section 5.2.2.4.

5.2.2.4 The real time imaging of the electrical positioning method

To image the accelerometer during DNA electrical positioning using a microscope, a novel objective adaptor was fabricated to perform imaging at a 90° angle. The 90° objective adaptor was designed using Autodesk Inventor design software which was fabricated from steel by the engineering department at Newcastle University. The objective adaptor allowed the imaging of the accelerometer device at a 90° angle using the Nikon eclipse 80i epi-fluorescent microscope. The reason for the microscope being used alternatively to the camera was so that the fluorescent emission of the fluorescently labelled DNA could not be observed undertaken with the camera. The setup allowed the simultaneous fluorescent imaging and immersion of the accelerometer sensing gap in DI water whilst applying an electrical potential for DNA positioning. A Nikon x100 magnification objective lens with a super long working distance (SLWD) was employed to screw into the adaptor to allow imaging of the sensing gap without the need to be very close to the sample. The adaptor consisted of a mirror and a steel tube that could connect to an objective, as illustrated in Figure 5-6. The adaptor screwed directly into the microscope objective while the light generated from the bulb was routed by the mirror through the objective lens to the sample which was reflected back to the microscope for imaging.

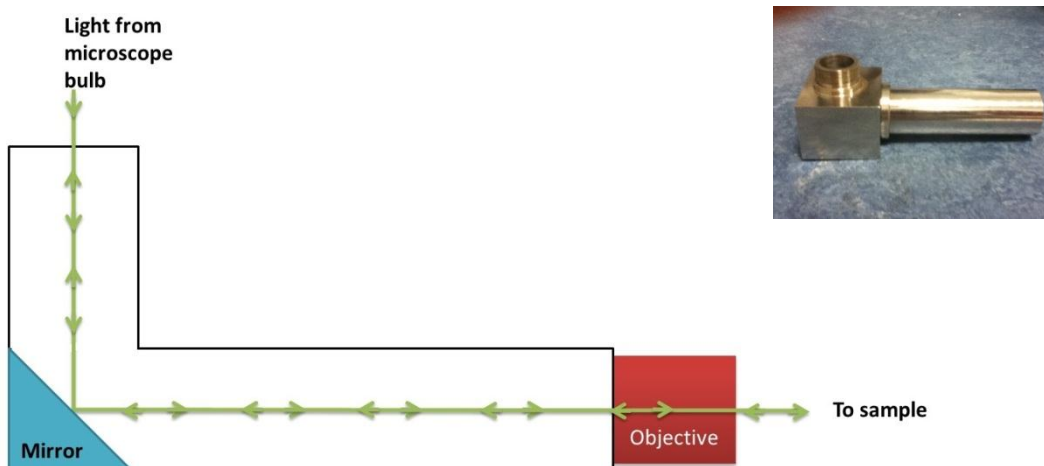


Figure 5-6: A schematic of the 90° objective adaptor with internal mirror to allow imaging when coupled to the microscope. Top inset: An image of the actual fabricated 90° objective adaptor.

The careful immersion of the accelerometer sensing gap in DI water for electrical positioning was performed by the staging. The stage also allowed the movement of accelerometer to allow fine focusing as the 90° objective adaptor was static on the microscope that did not allow focusing. The microscope computer software (Nikon BR elements) allowed images and videos to be captured from the microscope and stored digitally for further analysis. Once the focusing and fine adjustments were complete, the electrical positioning took place. The illustration in Figure 5-5 shows the apparatus in operation.

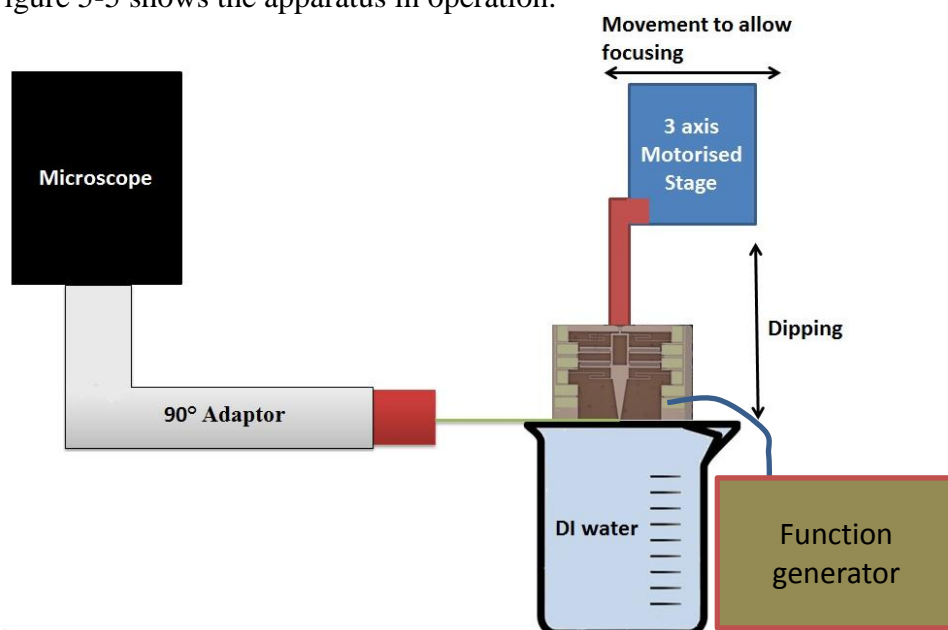


Figure 5-5: The 90° objective adaptor attached to the microscope to allow imaging of the accelerometer being dipped DI water for electrical positioning. The motorised stage allowed the dipping and focusing to be performed.

The image in Figure 5-7 shows a real world image of the apparatus used for the electrical positioning. The SLWD objective can be observed at a 90° angle focusing on the packaged accelerometer DIP. The wires attached to the chip socket can be observed that were used to electrically connect the accelerometer to the function generator and oscilloscope.

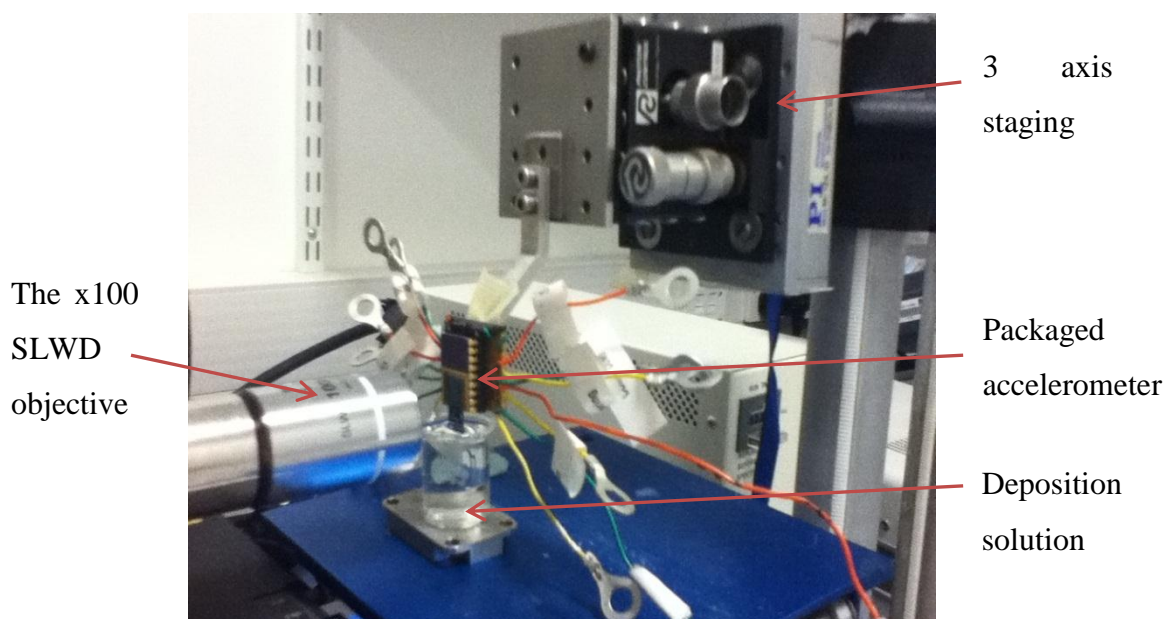


Figure 5-7: The packaged accelerometer immersed in solution contained in the glassware that was observed using the microscope. Note- the DIP chip socket is not electrically connected to the function generator for DNA electrical positioning in this image.

5.2.2.5 The electrical positioning of DNA in the sensing gap

Once the chemistries had been performed to place λ -DNA on the sensing tip of an accelerometer electrical positioning was undertaken. An electrical potential was applied between the sensing gap of the accelerometer to polarise the DNA placed on the 1st sensing tip to stretch it to the opposing sensing tip to be chemisorbed by the thiol situated on the pre-hybridised oligonucleotide probe B at the terminus of YOYO-1/DNA+B. An electrical potential was applied between the sensing gap using a 'Blackstar Jupiter 2000' signal generator. The signal generator was coupled to an 'Agilent DS03102A' oscilloscope to ensure that the electrical potential produced was correct for the application required.

5.2.2.5.1 DC electrical positioning

The initial electrical positioning studies were performed using DC electrophoretic stretching. A DC potential was applied between the sensing gap that was very slowly increased until it was observed that DNA migrated to the opposing sensing tip. A maximum voltage of 9 volts was applied so that damage to the accelerometer did not occur. The voltage applied was monitored on the coupled oscilloscope

5.2.2.5.2 AC Dielectric positioning

The method of dielectrophoretic stretching was undertaken to allow an electrical potential of 24 V_{p-p} at 1.6 MHz to be applied between the sensing gap to investigate DNA positioning. The potential was applied for 5 seconds and viewed in real time using video microscopy.

5.3 Results and outcomes

This section discusses the outcomes obtained from the positioning of fluorescently labelled λ -DNA that was observed using the apparatus described in the methods section.

5.3.1 The molecular coming of YOYO-1/DNA on a glass surface

The YOYO-1/DNA molecules were imaged in various locations on the glass slide as shown in Figure 5-8. As can be seen in the digitally zoomed image, green fluorescent objects were observed. The objects being characteristic to what has been reported to be YOYO-1/DNA bundles. The bundles were measured to be approx. 10 μm in length and are similar to what has been reported previously in the literature (Bensimon, Simon et al. 1995; Bennink, Schärer et al. 1999). The imaging of the YOYO-1/DNA in this initial study confirmed that the imaging of the fluorescent DNA bundles could be achieved using the apparatus available. The next step was to use the technique to position the DNA across the sensing gap to construct a DNA nanowire.

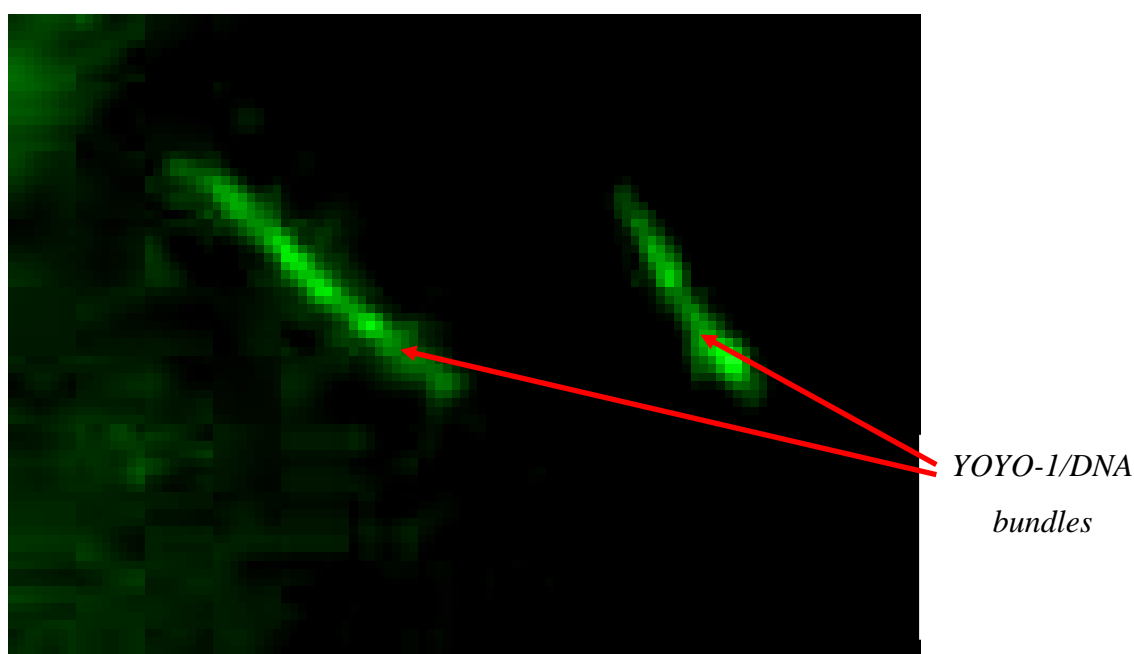


Figure 5-8: An image showing YOYO-1 stained λ -DNA combed on a glass slide, picture taken with an x100 objective lens.

5.3.2 The placement of YOYO-1/DNA in the sensing gap

The placement of YOYO-1/DNA+B in the sensing gap by molecular combing was performed using the method described. As can be seen in Figure 5-9 which is a multichannel brightfield/FITC image, YOYO-1 labelled DNA characteristic fluorescence was observed. The image indicates that a DNA bridge was constructed within the sensing gap. The area indicated by the arrow shows the nanowire spanned between both sensing tips. A meagre amount of fluorescence was observed on the gold sensing tips; this could be due to the gold quenching the emission of the fluorophore. The quenching of fluorophores by metals is due to non-radiative energy transfer from the fluorophore to the metal, it has also been suggested to be distance dependent as described in the literature (Hellen and Axelrod 1987; Schneider, Decher et al. 2006). The DNA bridge appears to be consistent to images that have been reported in the literature and similar to what was observed by the molecular combing technique performed in the previous section. However molecular combing was not suitable for the construction of a working biological accelerometer as the actuating features and electrical connections became damaged employing this method.

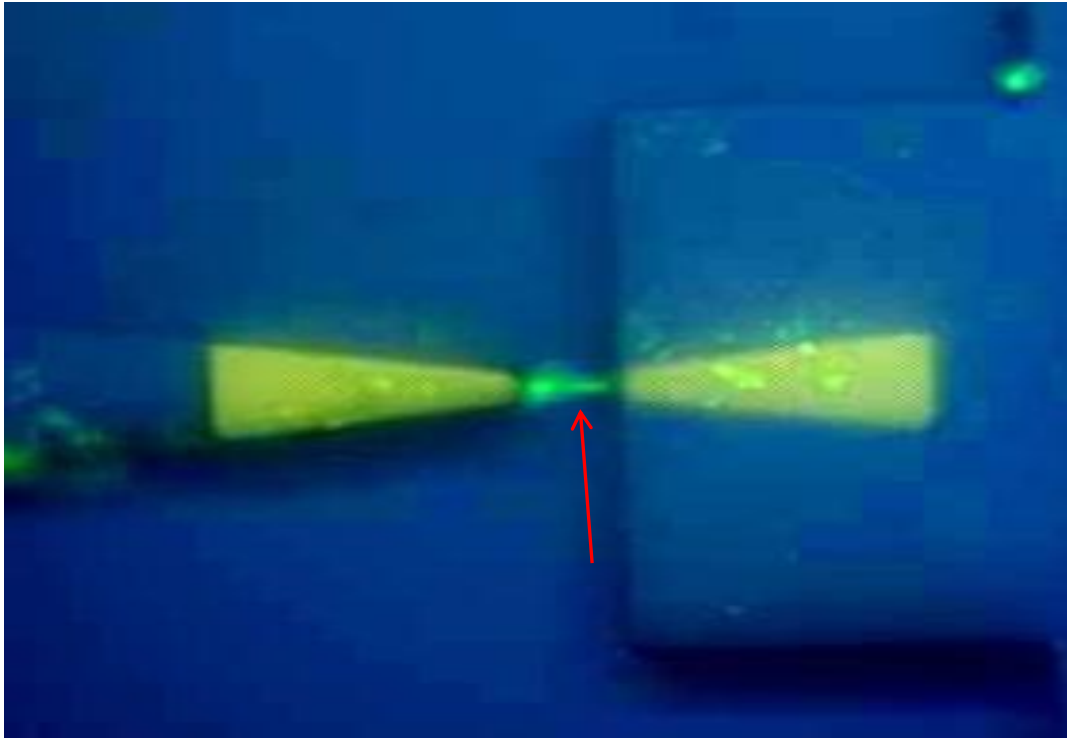


Figure 5-9: A combined light microscope image and FITC fluorescent image using a taken with an x50 objective lens. The arrow indicates the fluorescent DNA bridge spanned across the sensing gap.

5.3.3 The DC electrophoretic positioning of YOYO-1/DNA

The DC electrophoretic stretching of YOYO-1/DNA was undertaken to polarise the negatively charged DNA backbone towards the positively charged opposing sensing tip. The image in Figure 5-10 shows a fluorescently labelled DNA bridge spanned across the sensing gap of the accelerometer. The image is a multichannel image showing a fluorescent image alongside the brightfield image over-lapped. As can be seen the right sensing tip is somewhat damaged from the electrical positioning protocol. The damage may have occurred from the voltage applied to the sensing gap.

The electrolysis of water may have damaged the sensing tip (anode) by the production of oxygen on the gold surface at a high rate where heat generated on the gold surface caused damage, giving the black appearance. Therefore the voltage was delicately increased from 0 volts to approx. 9 volts where the DNA favoured the conditions to form a bridge. Although this protocol allowed DNA to be spanned across the sensing gap it was noted that it may be potentially too damaging to the gold layer of the sensing tips, this could potentially compromise the future application of sensing. Therefore the method of positioning DNA using dielectrophoretic positioning was also investigated.

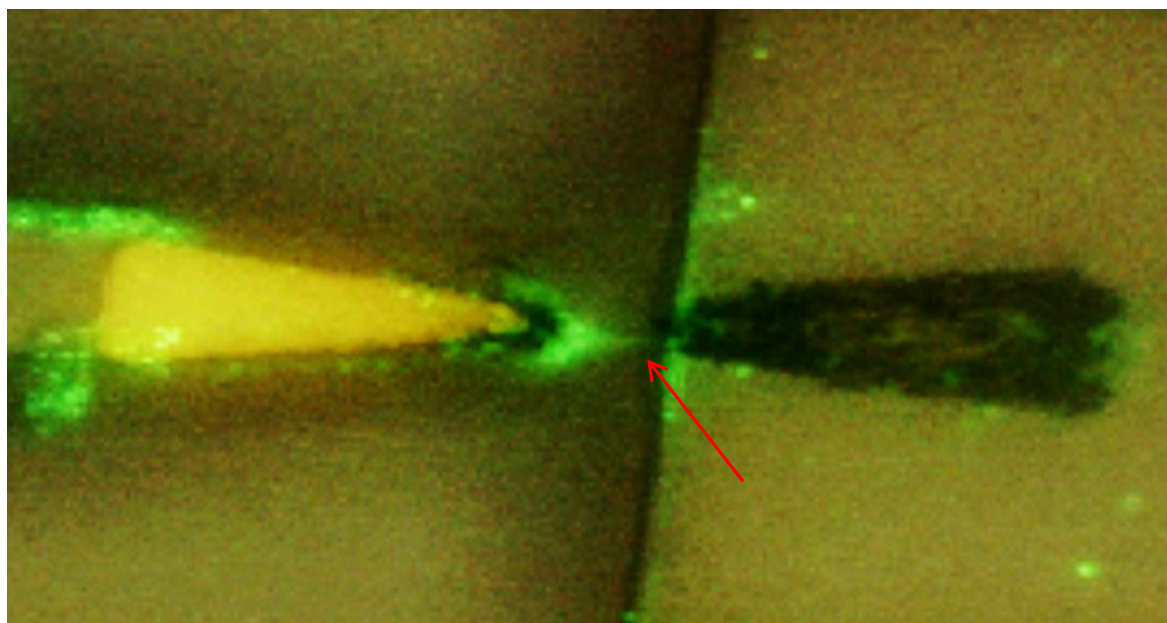


Figure 5-10: A combined light microscope image and a fluorescent image using a FITC filter taken with an x100 objective and further digitally zoomed to obtain the image. The arrow indicates the DNA bridge spanned between the sensing gap.

5.3.4 The dielectrophoretic positioning of YOYO-1/DNA

The positioning of chemically immobilised YOYO-1/DNA between the sensing gap was investigated. The high frequency electrical field was applied to polarise the surface bound YOYO-1/DNA+B on the 1st sensing tip to the opposing tip. The image compilation below in Figure 5-11 shows an image breakdown of a video recording that was produced of the electrical potential being applied between the sensing tips.

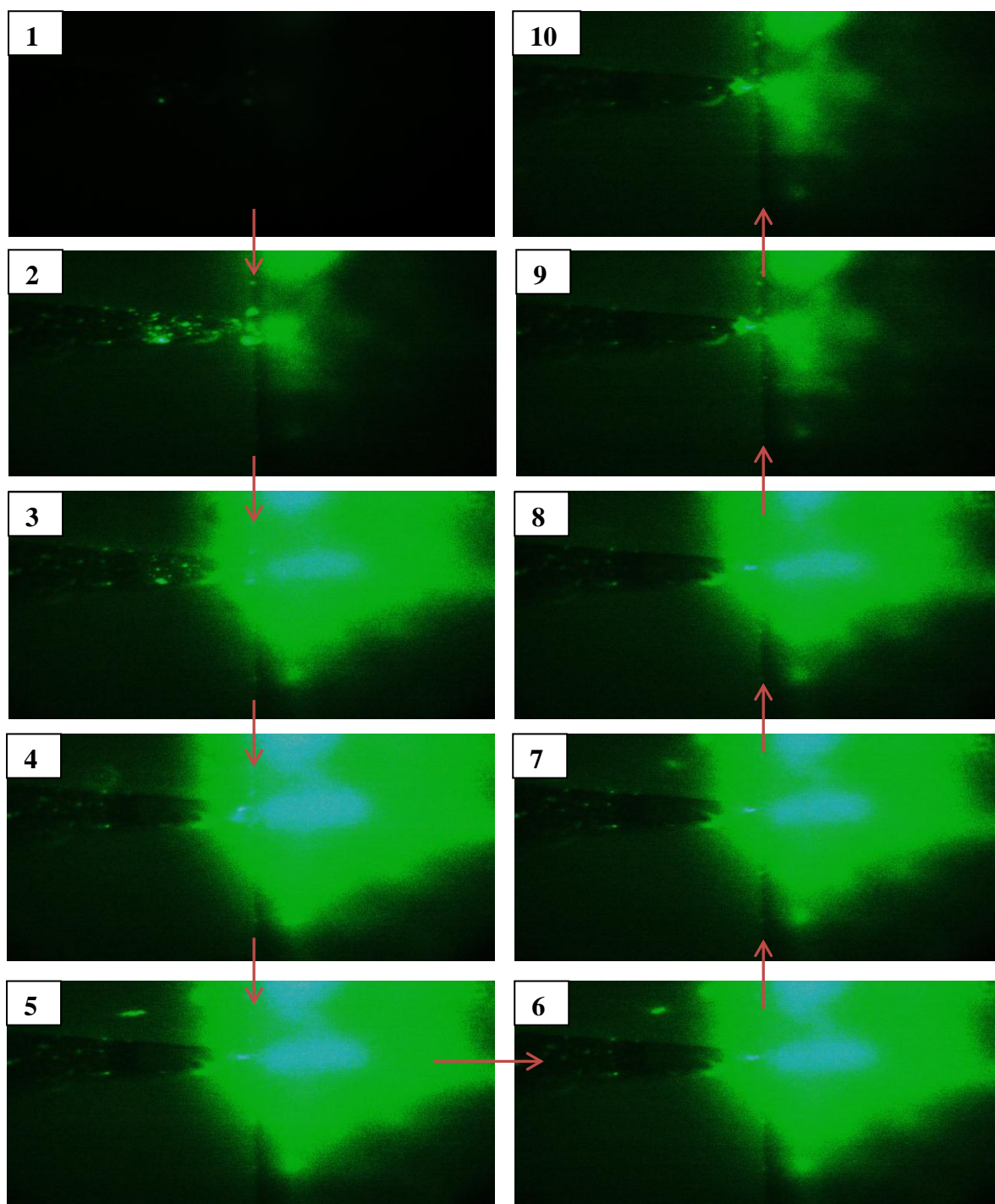


Figure 5-11: An image compilation showing the dielectrophoretic positioning of YOYO-1/DNA in the sensing gap.

As can be observed in Figure 5-11 once the electrical potential was applied, the 1st sensing tip began to glow bright green which can be observed clearly in the 3rd image of the compilation. This may indicate that the YOYO-1/DNA immobilised on the tip may have become polarised and elongated from the surface. The elongation allowing the molecule to become further situated from the gold surface that can quench the fluorescent emission. Therefore once elongated and stretched from the gold sensing tip the emission becomes visible. As seen in the 4th image of the compilation, a green fluorescence can be seen departing from the 1st sensing tip into the sensing gap. A DNA bridge characteristic object was seen to be formed between the sensing gap which is apparent in the 5th image of the compilation. The DNA bridge being characteristic to what has been demonstrated in the literature (Braun, Eichen et al. 1998; Bustamante, Smith et al. 2000) and from personal experience of imaging YOYO-1/DNA. The bridge seems to stay in position during the potential being applied and afterwards when the potential was switched off that is first shown in the 9th image. The 10th image shows the sensing gap after the potential was applied and the bridge was still observed. The images displayed in Figure 5-12 show larger images of the sensing gap before and after the potential was applied for clarity, the bridge can be clearly seen spanning the gap. This method of positioning DNA didn't produce the amount of damage to the sensing tip that was observed when using DC electrophoretic positioning.

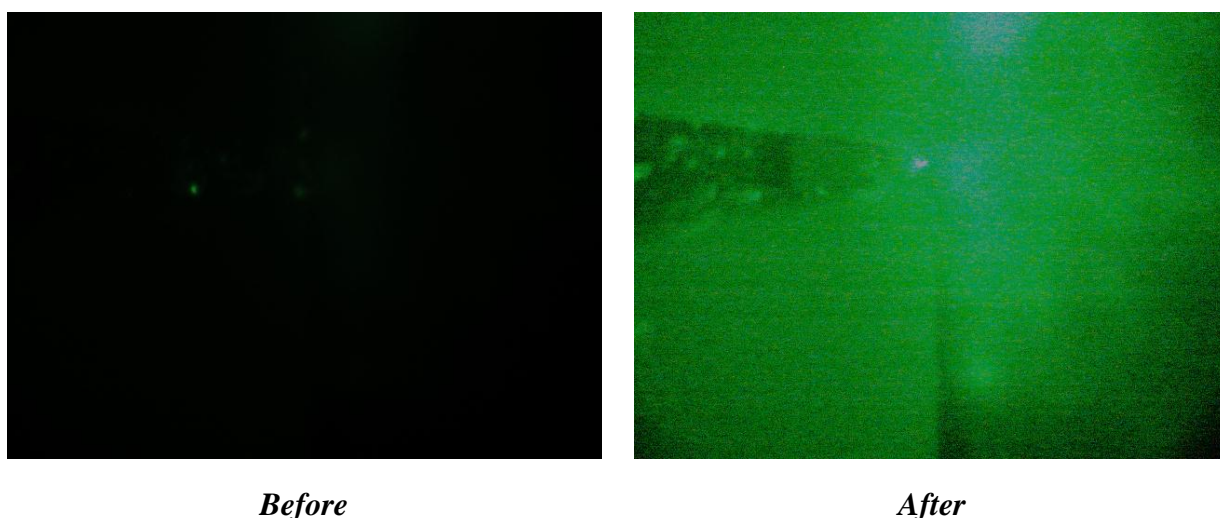


Figure 5-12: The still images obtained from the video microscopy of the accelerometer sensing gap before and after the electrical potential was applied. The DNA was shown to be migrated from the 1st sensing tip to the opposing sensing tip. The 'after' image brightness has been adjusted for the ease of printing.

5.4 Conclusion

The positioning and imaging of YOYO-1/DNA was achieved using the optical microscope which was initially performed by molecular combing the DNA on a glass substrate. Thereafter, the molecular combing technique was employed to position chemically immobilised DNA between the sensing gap successfully. The novel approach of individually dipping the 1st sensing tip within a 10 μm limit was performed with the dipping station apparatus effectively. This allowed the immobilisation of the sensing tip whilst allowing the opposing tip to remain clean and non-functionalised. The methods of DNA immobilisation and electrophoretic positioning have been validated for use in an accelerometer the sensing gap. The use of dielectrophoretic was shown to be the favoured method as it reduces the possibility of damage to the sensing tips associated with DC electrophoretic positioning. Therefore, DNA was shown to be able to be placed in the sensing gap of an accelerometer to prove the proof of concept to fabricate a biological accelerometer using the methods developed.

6 Chapter 6 Summary and Conclusions

6.1 Summary

This thesis describes the development of bioelectronics for inertial sensing applications that discusses the design, fabrication, characterisation and biological functionalisation of a biological accelerometer.

6.2 Discussion

The purpose of undertaking the research was to certify the proof of concept to develop a biological MEMS accelerometer for inertial sensing applications. The aspiration being to develop a microscale accelerometer that is highly sensitive and has an increased dynamic range compared to what is currently commercially available. At the moment commercially available accelerometers allow sensing within a limited range as discussed in chapter 1.

Working towards biological accelerometer to become realised, the following were achieved;

1. The design and fabrication of a silicon microscale accelerometer, designed to allow chemical functionalisation to construct a DNA bridge to act as a strain gauge.
2. Validating that the chemical placement of λ -DNA on gold substrates is feasible using the Biacore instrument.
3. The metallisation of λ -DNA using zinc ions was achieved without the need to conformally dope the molecule and dramatically increasing the width, hence retaining the worm like chain properties.
4. The selective chemical immobilisation of λ -DNA within the sensing gap region of the accelerometer by dipping in deposition solution without immersing the actuating features and bond pads that would affect device operation if it was to occur.
5. The positioning of DNA in the sensing gap spanned between two opposing tips therefore constructing a biological strain gauge.

The accelerometer were designed with gold sensing tips to allow the selective covalent chemical immobilisation of DNA in the sensing gap where the electrostatic comb drives were designed to be used as a feedback mechanism to increase or decrease the sensing gap to reset the DNA molecule in the start position during acceleration. The comb drive actuators of the 3 types were characterised using static deflection measurements to determine which showed the

largest deflection to vary the sensing gap distance. As expected the type 1 accelerometer exhibited the largest mean average static deflection with a 2.9 μm distance that was significantly greater than that of type 3; this was due to the feature dimensions being significantly different between the types. The comb drive finger spacing and the spring width both were concluded to play a role in the degree of static deflection which was determined by comparing the performance between the types. However the deflection measured for all types was deemed not large enough to construct a working prototype biological accelerometer; hence the study was carried out to prove a proof of concept for a future investigation.

The natural resonant frequencies and mode shapes that were determined from the FEA prior to fabrication were confirmed post-fabrication with experimental results. The resonant frequencies that were calculated from the simulation and the real experimental results were in close agreement. The FEA and the experimentally measured data of the type 1 mode 1 frequency being 2.44 KHz and 2.46 KHz respectively, therefore a 0.81 % difference between the two methods was encountered.

The production of a chemical SAM capture layer was initially assembled on the Biacore SPR gold surface was confirmed by monitoring the change of RU. The hybridisation of the complementary λ -DNA was confirmed also by the change of RU that proved that the protocols could be employed for the accelerometer application. The efficiency of the hybridisation was not a major concern; therefore the protocols were not optimised to gain a maximum hybridisational efficiency. The difference of the RU change between the hybridisation protocols of the pre-treatment of λ -DNA established that sequence specific hybridisation was occurring and that modification of the DNA termini could be controlled. Hence, it was proved that λ -DNA could be pre-treated with oligonucleotide probe B which showed to hybridise to the complementary SAM with a greater efficiency.

It was found that the maximum peak shift observed using UV-Vis spectrophotometric analysis was 5 nm which allowed the saturation concentration to be found at 5 mM employing zinc perchlorate as the source of zinc ions. It was suggested that at this concentration the DNA molecule becomes fully loaded with zinc ions causing the maximum A_{260} peak shift. The fluorescence assay undertaken also confirmed that DNA becomes fully saturated at this concentration by observing the fluorescent attenuation of YOYO-1/DNA.

The study showed a simple and robust method to produce M-DNA to develop a proof of concept for the application of making a metallised DNA strain gauge within an accelerometer.

The use of electrical positioning the DNA was deemed the most suitable for this application, as it is a non-contact method unlike molecular combing which may damage the floating structures by force or due to them being immersed in solution. The application of the electrical positioning techniques of applying a potential between the sensing gap to bridge DNA was successful; the dielectrophoretic method was favoured as it reduced the possibility of damage to the gold sensing tips that can occur with DC positioning. The dielectrophoretic method was shown to elongate λ -DNA+B from one sensing tip to the opposing tip in real time effectively to construct a DNA nanowire placed in the sensing gap. This proved a proof of concept that DNA could be positioned in the sensing gap for use as a mechanical strain gauge. The assembly of a fully functional biological accelerometer that measures the change of the electrical properties of DNA with stretching could not be undertaken due to the poor actuating performance of the accelerometers types. A design improvement will need to be performed if a further fabrication was to be undertaken to construct a fully functional biological accelerometer.

6.2.1 A design improvement

A design improvement to the silicon accelerometers fabricated would have potential benefits to assemble a DNA strain gauge based accelerometer. The drawback to the current accelerometers being that they showed a low value of deflection when the comb drives were actuated for the type 1 which made it impossible to stretch the DNA for this application in the 10 μm sensing gap. As discussed in chapter 3 this was due to the comb drive fingers undergoing lateral displacement during electrical actuation which was detrimental to displacement. To overcome this problem it may be beneficial to make some subtle adjustments to the design of the type 1 accelerometer.

The comb overlapping finger diameter of the type 1 accelerometer that was modelled to be of the required standard could be redesigned with springs that are more rigid laterally to reduce pull-in though still soft in the actuation plane to allow the required deflection. This may allow the deflection that was modelled using ANSYS to be realised without a plateau of static deflection allowing a value of 14 μm to be realised at 55 V.

The alternative option would be to fabricate the structures exactly in this study with a smaller sensing gap. This will allow the use of smaller chain DNA molecules such as plasmids to be used as a DNA strain gauge. The 10 μm sensing gap was fabricated to reduce fabrication tolerances though it limited the form of DNA to longer lengths, λ -DNA being the most useful for this application. Hence, the redesigning of the accelerometer features for a future study may prove fruitful.

7 References

- Abthagir, P. S. and R. Saraswathi (2001). "Junction properties of metal/polypyrrole Schottky barriers." Journal of Applied Polymer Science **81**(9): 2127-2135.
- Aich, P., S. L. Labiuk, et al. (1999). "M-DNA: a complex between divalent metal ions and DNA which behaves as a molecular wire." Journal of Molecular Biology **294**(2): 477-485.
- Ajit, K. M., S. Adina, et al. (2006). "Gold surface with sub-nm roughness realized by evaporation on a molecular adhesion monolayer." Applied Physics Letters **88**(15): 151917.
- Alivisatos, A. P., K. P. Johnsson, et al. (1996). "Organization of 'nanocrystal molecules' using DNA." Nature **382**(6592): 609-611.
- Allemand, J. F., D. Bensimon, et al. (1997). "pH-dependent specific binding and combing of DNA." Biophys. J. **73**(4): 2064-2070.
- Apple. (2010). "The future is in the details." 2010, from <http://www.apple.com/iphone/design/>.
- Bain, C. D., Troughton, E.B., Tao, Y.T., Evall, J., Whitesides, G.M., Nuzzo, R.G. (1989). "Formation of Monolayer Films by the Spontaneous Assembly of Organic Thiols from Solution onto Gold'." Journal of the American Chemistry Society **111**: 321-335.
- Bennink, M. L., O. D. Schärer, et al. (1999). "Single-molecule manipulation of double-stranded DNA using optical tweezers: Interaction studies of DNA with RecA and YOYO-1." Cytometry **36**(3): 200-208.
- Bensimon, A., A. Simon, et al. (1994). "Alignment and sensitive detection of DNA by a moving interface." Science **265**(5181): 2096-2098.

- Bensimon, D., A. J. Simon, et al. (1995). "Stretching DNA with a Receding Meniscus: Experiments and Models." Physical Review Letters **74**(23): 4754.
- Bouchiat, C., M. D. Wang, et al. (1999). "Estimating the Persistence Length of a Worm-Like Chain Molecule from Force-Extension Measurements." Biophysical journal **76**(1): 409-413.
- Braun, E., Y. Eichen, et al. (1998). "DNA-templated assembly and electrode attachment of a conducting silver wire." Nature **391**(6669): 775-778.
- Britannica, E. (2009). "Scanning Electron Microscopy." Retrieved 2011, from <http://www.britannica.com/EBchecked/topic/526571/scanning-electron-microscope-SEM>.
- Bustamante, C., S. B. Smith, et al. (2000). "Single-molecule studies of DNA mechanics." Current Opinion in Structural Biology **10**(3): 279-285.
- Butt, H. J., Selfert, K., Bamberg, E. (1993). "Imaging Molecular Defects in Alkanethiol Monolayers with an Atomic Force Microscope." J. Phys. Chem. **97**: 7316-7320.
- Chrisey, L. A., G. U. Lee, et al. (1996). "Covalent attachment of synthetic DNA to self-assembled monolayer films." Nucl. Acids Res. **24**(15): 3031-3039.
- Dahm, R. (2005). "Friedrich Miescher and the discovery of DNA." Developmental Biology **278**(2): 274-288.
- de Pablo, P. J., F. Moreno-Herrero, et al. (2000). "Absence of dc-Conductivity in lambda - DNA." Physical Review Letters **85**(23): 4992.
- Deck, L. and P. de Groot (1994). "High-speed noncontact profiler based on scanning white-light interferometry." Appl. Opt. **33**(31): 7334-7338.

- DeRose, J. A., T. Thundat, et al. (1991). "Gold grown epitaxially on mica: conditions for large area flat faces." Surface Science **256**(1-2): 102-108.
- Dong, H., Y. Jia, et al. (2005). "A novel out-of-plane MEMS tunneling accelerometer." Sensors and Actuators A: Physical **120**(2): 360-364.
- Dong, L., T. Hollis, et al. (2007). "Synthesis, Manipulation and Conductivity of Supramolecular Polymer Nanowires." Chemistry – A European Journal **13**(3): 822-828.
- Elata, D. and V. Leus (2005). "How slender can comb-drive fingers be?" Journal of Micromechanics and Microengineering **15**(5): 1055.
- Elwenspoek, M. (1996). "The form of etch rate minima in wet chemical anisotropic etching of silicon." Journal of Micromechanics and Microengineering **6**(4): 405.
- Farell, J. A., Barth, M. (1999). The global Positioning System & Inertial Navigation, McGraw-Hill Companies, Inc.
- Fredriksson, H., D. Chakarov, et al. (2009). "Patterning of highly oriented pyrolytic graphite and glassy carbon surfaces by nanolithography and oxygen plasma etching." Carbon **47**(5): 1335-1342.
- Germishuizen, W. A., auml, et al. (2003). "Selective dielectrophoretic manipulation of surface-immobilized DNA molecules." Nanotechnology **14**: 896-902.
- Goldstein, J., Newbury, D.E., Joy, D.C., Lyman, C.E., Echlin, P., Lifshin, E., Sawyer, L., Michael, J.R. (2004). Scanning electron microscopy and x-ray microanalysis, 4th printing.
- Grant, A., P. Williams, et al. (2009). "GPS Jamming and the Impact on Maritime Navigation." The Journal of Navigation **62**(02): 173-187.

- Grewal, M. S. (2001). Global Positioning Systems, Inertial Navigation, and Integration
John Wiley & Sons, INC. Publication.
- Gu, Q., C. Cheng, et al. (2006). "DNA nanowire fabrication." Nanotechnology **17**(1): R14-
R25.
- Günther, K., M. Mertig, et al. (2010). "Mechanical and structural properties of YOYO-1
complexed DNA." Nucleic Acids Research **38**(19): 6526-6532.
- HacknMod.com. (2011). "Wiimote." from <http://hacknmod.com/hack/easily-connect-a-wiimote-to-your-pc/>.
- Halibel, N. a. (2008). Zero Time Space, WILEY - VCH Verlag GmbH & Co.
- Heisenberg, W. (1927). "Über den anschaulichen Inhalt der quantentheoretischen Kinematik
und Mechanik." Zeitschrift für Physik A Hadrons and Nuclei **43**(3): 172-198.
- Hellen, E. H. and D. Axelrod (1987). "Fluorescence emission at dielectric and metal-film
interfaces." J. Opt. Soc. Am. B **4**(3): 337-350.
- Hensinger, W. K., H. Haffner, et al. (2001). "Dynamical tunnelling of ultracold atoms."
Nature **412**(6842): 52-55.
- Herne, T. M. and M. J. Tarlov (1997). "Characterization of DNA Probes Immobilized on
Gold Surfaces." Journal of the American Chemical Society **119**(38): 8916-8920.
- Hershey, A. D. and M. Chase (1952). "Independent functions of viral proteins and Nucleic
acid in growth of bacteriophage." The Journal of General Physiology **36**(1): 39-56.
- Houlihan, R. and M. Kraft (2005). "Modelling squeeze film effects in a MEMS accelerometer
with a levitated proof mass." Journal of Micromechanics and Microengineering **15**(5):
893.

- Hyeon Cheol, K., S. Seonho, et al. (2005). Inertial-grade out-of-plane and in-plane differential resonant silicon accelerometers (DRXLs). Solid-State Sensors, Actuators and Microsystems, 2005. Digest of Technical Papers. TRANSDUCERS '05. The 13th International Conference on.
- J. K. N. Mbindyo., B. D. R., B. R. Martin., C. D. Keating., M. J. Natan., T. E. Mallouk (2001). "DNA-Directed Assembly of Gold Nanowires on Complementary Surfaces." Advanced Materials **13**(4): 249-254.
- Johansen, F. and J. P. Jacobsen (1998). "H-1 NMR studies of the bis-intercalation of a homodimeric oxazole yellow dye in DNA oligonucleotides." Journal of Biomolecular Structure & Dynamics **16**(2): 205-222.
- Keegan, N., N. G. Wright, et al. (2005). "Circular Dichroism Spectroscopy of Folding in a Protein Monolayer." Angewandte Chemie International Edition **44**(30): 4801-4804.
- Keren, K., R. S. Berman, et al. (2004). "Patterned DNA Metallization by Sequence-Specific Localization of a Reducing Agent." Nano Letters **4**(2): 323-326.
- Keren, K., M. Krueger, et al. (2002). "Sequence-Specific Molecular Lithography on Single DNA Molecules." Science **297**(5578): 72-75.
- Kim, Y., K. S. Kim, et al. (2011). "Nanochannel confinement: DNA stretch approaching full contour length." Lab on a Chip **11**(10): 1721-1729.
- King, A. D. (1997). Inertial navigation-past, present, and future. Airborne Navigation Systems Workshop (Digest No. 1997/169), IEE Colloquium on.
- Kovacs, G. T. A., N. I. Maluf, et al. (1998). "Bulk micromachining of silicon." Proceedings of the IEEE **86**(8): 1536-1551.

- Kumar, A. (2000). "Biosensors Based on Piezoelectric Crystal Detectors: Theory and Application." Retrieved 12th May, 2007, from <http://www.tms.org/pubs/journals/JOM/0010/Kumar/Kumar-0010.html>.
- Laermer, F. and A. Urban (2003). "Challenges, developments and applications of silicon deep reactive ion etching." Microelectronic Engineering **67-68**: 349-355.
- Laibinis, P. E., Whitesides, G M., Allara, D. L., Tao, Y. T., Parikh, A. N., Nuzzo, R. G. (1991). "Comparison of the Structures and Wetting Properties of Self-Assembled Monolayers of n-Alkanethiols on the Coinage Metal Surfaces, Cu, Ag, Au." Journal of the American Chemical Society **113**: 7152-7167.
- Lederberg, E. M. (1951). "Lysogenicity in E. coli K-12." Genetics **36**.
- Lederberg, E. M. and J. Lederberg (1953). "Genetic studies of lysogenicity in Escherichia coli." Genetics **38**(1): 51-64.
- Lee, I., G. H. Yoon, et al. (2005). "Development and analysis of the vertical capacitive accelerometer." Sensors and Actuators A: Physical **119**(1): 8-18.
- Legtenberg, R. and et al. (1996). "Comb-drive actuators for large displacements." Journal of Micromechanics and Microengineering **6**(3): 320.
- Legtenberg R, J. H., de Boer M and E. M (1995). J. Electrochem. Soc. **142**(6): 2020.
- Levene, P. A. (1919). "The structure of yeast nucleic acid. IV. Ammonia hydrolysis." Journal of Biological Chemistry **40**: 415-424
- Levicky, R., T. M. Herne, et al. (1998). "Using Self-Assembly To Control the Structure of DNA Monolayers on Gold: A Neutron Reflectivity Study." Journal of the American Chemical Society **120**(38): 9787-9792.

- Liedberg, B., C. Nylander, et al. (1983). "Surface plasmon resonance for gas detection and biosensing." Sensors and Actuators **4**: 299-304.
- Linkopings. (2007). "Self-Assembled Monolayers." Retrieved 12th June 2007, from <http://www.ifm.liu.se/applphys/ftir/sams.html>.
- Liqin Dong, T. H. S. F. Bernard A. C. Nicholas G. W. Benjamin R. H. A. H. (2007). "Synthesis, Manipulation and Conductivity of Supramolecular Polymer Nanowires." Chemistry - A European Journal **13**(3): 822-828.
- Lyubchenko, Y. L. and L. S. Shlyakhtenko (1997). "Visualization of supercoiled DNA with atomic force microscopy in situ." Proceedings of the National Academy of Sciences **94**(2): 496-501.
- Marko, J. F. and E. D. Siggia (1995). "Stretching DNA." Macromolecules **28**(26): 8759-8770.
- Marty, F., L. Rousseau, et al. (2005). "Advanced etching of silicon based on deep reactive ion etching for silicon high aspect ratio microstructures and three-dimensional micro- and nanostructures." Microelectronics Journal **36**(7): 673-677.
- Mastrangelo, C. H. and C. H. Hsu (1993). "Mechanical stability and adhesion of microstructures under capillary forces. I. Basic theory." Microelectromechanical Systems, Journal of **2**(1): 33-43.
- Maya, L., C. E. Vallet, et al. (1997). "Sputtered gold films for surface-enhanced Raman scattering." Journal of Vacuum Science & Technology A: Vacuum, Surfaces, and Films **15**(2): 238-242.
- Mbindyo, J. K. N., B. D. Reiss, et al. (2001). "DNA-Directed Assembly of Gold Nanowires on Complementary Surfaces." Advanced Materials **13**(4): 249-254.

- Mirkin, C. A., R. L. Letsinger, et al. (1996). "A DNA-based method for rationally assembling nanoparticles into macroscopic materials." Nature **382**(6592): 607-609.
- Namasivayam, V., R. G. Larson, et al. (2002). "Electrostretching DNA Molecules Using Polymer- Enhanced Media within Microfabricated Devices." Anal. Chem. **74**(14): 3378-3385.
- NCBI. (2007). "National Centre for Biotechnology Information." from <http://www.ncbi.nlm.nih.gov/>.
- Ning, Y., Y. Loke, et al. (1995). "Fabrication and characterization of high g-force, silicon piezoresistive accelerometers." Sensors and Actuators A: Physical **48**(1): 55-61.
- Nintendo. (2006). "The Wii accelerometer." 2010, from http://www.nintendowiinews.net/Blogs/News/hqs/blr_4292.aspx.
- Nuzzo, R. G., B. R. Zegarski, et al. (1987). Fundamental studies of the chemisorption of organosulfur compounds on Au(111). Implications for molecular self-assembly on gold surfaces, United States.
- Omerzu, A., D. Mihailovicacute, et al. (2007). "Optical spectra of wet and dry M -DNA." Physical Review B **75**(12): 121103.
- Peelen, D. and L. M. Smith (2004). "Immobilization of Amine-Modified Oligonucleotides on Aldehyde-Terminated Alkanethiol Monolayers on Gold." Langmuir **21**(1): 266-271.
- Perkins, T. T., S. R. Quake, et al. (1994). "Relaxation of a single DNA molecule observed by optical microscopy." Science **264**(5160): 822-826.
- Perkins, T. T., D. E. Smith, et al. (1995). "Stretching of a single tethered polymer in a uniform flow." Science **268**(5207): 83-87.

- Peterson, A. W., R. J. Heaton, et al. (2001). "The effect of surface probe density on DNA hybridization." Nucl. Acids Res. **29**(24): 5163-5168.
- Piscevic, D., W. Knoll, et al. (1995). "Surface plasmon microscopy of biotin-streptavidin binding reactions on UV-photopatterned alkanethiol self-assembled monolayers." Supramolecular Science **2**(2): 99-106.
- Pray, L. A. (2008). "Discovery of DNA Structure and Function: Watson and Crick." from <http://www.nature.com/scitable/topicpage/discovery-of-dna-structure-and-function-watson-397>.
- Rakitin, A., P. Aich, et al. (2001). "Metallic Conduction through Engineered DNA: DNA Nanoelectronic Building Blocks." Physical Review Letters **86**(16): 3670.
- Richter, J. (2001). "Construction of highly conductive nanowires on a DNA template." Appl. Phys. Lett. **78**(4): 536.
- Richter, J., M. Mertig, et al. (2001). "Construction of highly conductive nanowires on a DNA template." Applied Physics Letters **78**(4): 536-538.
- Richter, J., M. Mertig, et al. (2002). "Low-temperature resistance of DNA-templated nanowires." Applied Physics A: Materials Science & Processing **74**(6): 725-728.
- Richter, J., Monch, I. Schakert, H.K. (2001). "Construction of highly conductive nanowires on a DNA template." Applied Physics Letters **78**(4): 536-538.
- Richter, J., R. Seidel, et al. (2000). "Nanoscale Palladium Metallization of DNA." Advanced Materials **12**(7): 507-510.
- Roylance, L. M. and J. B. Angell (1979). "A batch-fabricated silicon accelerometer." Electron Devices, IEEE Transactions on **26**(12): 1911-1917.

- Schneider, G., G. Decher, et al. (2006). "Distance-Dependent Fluorescence Quenching on Gold Nanoparticles Ensheathed with Layer-by-Layer Assembled Polyelectrolytes." Nano Letters **6**(3): 530-536.
- Slic2. (2005). "Ligase Animation." Retrieved 22 June 2007, from <http://www.slic2.wsu.edu:82/hurlbert/micro101/pages/Chap10.html>.
- Smith, S. B., Y. Cui, et al. (1996). "Overstretching B-DNA: The Elastic Response of Individual Double-Stranded and Single-Stranded DNA Molecules." Science **271**(5250): 795-799.
- Spengen, W. M. v. and et al. (2002). "A physical model to predict stiction in MEMS." Journal of Micromechanics and Microengineering **12**(5): 702.
- Standaert, T. E. F. M., M. Schaepkens, et al. (1998). High density fluorocarbon etching of silicon in an inductively coupled plasma: Mechanism of etching through a thick steady state fluorocarbon layer, AVS.
- Steel, A. B., R. L. Levicky, et al. (2000). "Immobilization of Nucleic Acids at Solid Surfaces: Effect of Oligonucleotide Length on Layer Assembly." Biophys. J. **79**(2): 975-981.
- Steel, A. B., R. L. Levicky, et al. (2000). "Immobilization of Nucleic Acids at Solid Surfaces: Effect of Oligonucleotide Length on Layer Assembly." Biophysical journal **79**(2): 975-981.
- Storm, A. J., J. van Noort, et al. (2001). "Insulating behavior for DNA molecules between nanoelectrodes at the 100 nm length scale." Applied Physics Letters **79**(23): 3881-3883.
- Sun, W., L. Wu, et al. (2009). Dynamic Analysis of the Accelerometer's Shell Based on ANSYS. Measuring Technology and Mechatronics Automation, 2009. ICMTMA '09. International Conference on.

Titterton, D. H. (2004). Strapdown Inertial Navigation Technology, Institution of Electrical Engineers.

Ulman, A. (1996). "Formation and Structure of Self-Assembled Monolayers." Chem. Rev. **96**(4): 1533-1554.

van 't Hoff, M., M. Reuter, et al. (2009). "Screening by imaging: scaling up single-DNA-molecule analysis with a novel parabolic VA-TIRF reflector and noise-reduction techniques." Physical Chemistry Chemical Physics **11**(35): 7713-7720.

Van, C. N. and et al. (2000). "The influence of thickness and preparation temperature of doped polypyrrole films on the electrical and chemical sensing properties of polypyrrole/gold Schottky barrier diodes." Journal of Physics D: Applied Physics **33**(18): 2230.

Vogt, K. W., P. A. Kohl, et al. (1994). "Characterization of thin titanium oxide adhesion layers on gold: resistivity, morphology, and composition." Surface Science **301**(1-3): 203-213.

Vologodskii, A. (1994). "DNA Extension under the Action of an External Force." Macromolecules **27**(20): 5623-5625.

Washizu, M., O. Kurosawa, et al. (1995). "Applications of electrostatic stretch-and-positioning of DNA." Industry Applications, IEEE Transactions on **31**(3): 447-456.

Washizu, M., M. Washizu, et al. (1990). "Electrostatic manipulation of DNA in microfabricated structures." Industry Applications, IEEE Transactions on **26**(6): 1165-1172.

Washizu, M., M. Washizu, et al. (1990). "Electrostatic manipulation of DNA in microfabricated structures

- Electrostatic manipulation of DNA in microfabricated structures." Industry Applications, IEEE Transactions on **26**(6): 1165-1172.
- Washizu, M., M. Washizu, et al. (1995). "Applications of electrostatic stretch-and-positioning of DNA." Industry Applications, IEEE Transactions on **31**(3): 447-456.
- Washizu, M., M. Washizu, et al. (1995). "Applications of electrostatic stretch-and-positioning of DNA
Applications of electrostatic stretch-and-positioning of DNA." Industry Applications, IEEE Transactions on **31**(3): 447-456.
- Watson JD, C. F. (1953). "Molecular structure of nucleic acids; a structure for deoxyribose nucleic acid." Nature **171**(4356): 737-738.
- Weiss, B., A. Jacquemin-Sablon, et al. (1968). "Enzymatic Breakage and Joining of Deoxyribonucleic Acid. VI. FURTHER PURIFICATION AND PROPERTIES OF POLYNUCLEOTIDE LIGASE FROM ESCHERICHIA COLI INFECTED WITH BACTERIOPHAGE T4." J. Biol. Chem. **243**(17): 4543-4555.
- Wettig, S. D., C.-Z. Li, et al. (2003). "M-DNA: a Self-Assembling Molecular Wire for Nanoelectronics and Biosensing." Analytical Sciences **19**(1): 23-26.
- Wettig, S. D., D. O. Wood, et al. (2003). "Thermodynamic investigation of M-DNA: a novel metal ion-DNA complex." Journal of Inorganic Biochemistry **94**(1-2): 94-99.
- Williams, K. R. and R. S. Muller (1996). "Etch rates for micromachining processing." Microelectromechanical Systems, Journal of **5**(4): 256-269.
- Xia, Y. and G. M. Whitesides (1996). "Shadowed sputtering of gold on V -shaped microtrenches etched in silicon and applications in microfabrication." Advanced Materials **8**(9): 765-768.

Yokota, H., F. Johnson, et al. (1997). "A new method for straightening DNA molecules for optical restriction mapping." Nucl. Acids Res. **25**(5): 1064-1070.

Zhang, Y., Austin, R.H., Kraeft, J., Cox, E.C., Ong, N.P. (2002). "Insulating behavior of λ -DNA on the Micron Scale " Physical Review Letters **89**(19): 198102-198101 to 198102-198104.

Zimmermann, R. M. and E. C. Cox (1994). "DNA stretching on functionalized gold surfaces." Nucl. Acids Res. **22**(3): 492-497.